July 2021

Parametric Study of Integral Abutment Bridge Using Finite Element Model

Asako Takeuchi
University of Massachusetts Amherst

Parametric Study of Integral Abutment Bridge Using Finite Element Modeling

A Thesis Presented

by

ASAKO TAKEUCHI

Submitted to the Graduate School of the
University of Massachusetts Amherst in partial fulfillment
of the requirements for the degree of

MASTER OF SCIENCE

May 2021

Civil and Environmental Engineering

Parametric Study of Integral Abutment Bridge Using Finite Element Modeling

A Thesis Presented

by

Asako Takeuchi

Approved as to style and content by:

_____
Scott Civjan, Chairperson

_____
Sergio Breña, Member

_____
Jessica Boakye, Member

_____
John E. Tobiason, Department Head
Civil and Environmental Engineering Department

ACKNOWLEDGEMENTS

The research study reported in this thesis was made possible with financial support through McMillen Jacobs Associates Fellowship in Geotechnical Engineering.

I would like to express my gratitude to everyone who supported me in my academic accomplishments, especially during the pandemic.

First of all, I am extremely grateful to my advisor, Dr. Scott Civjan, for all the advice and assistance throughout my graduate studies and research. His kind words gave me the confidence and strength to overcome many obstacles. The completion of this thesis would not have been possible without his support.

I would also like to extend my gratitude to Dr. Sergio Breña for serving on my research committee and providing insightful feedback. I am especially grateful to him for supporting and encouraging me to apply to graduate schools back in my senior year. I am glad that I made the decision to continue my education.

I would also like to thank Dr. Jessica Boakye, who joined my research committee in her first semester at UMass, for all her thoughtful feedback on my research work. We were never able to meet in person, but I was glad to meet her and get to know her remotely.

Many thanks to my fellow graduate friends in the SEM program. Those days where we overcame all those tough assignments and projects together will forever be in my memories to look back on when I am going through difficult times in the future.

I would also like to thank my family and friends for their continuous support and encouragement. Special thanks to my parents for moral and financial support and providing me the best environment throughout my life in both Japan and the U.S.

Finally, I would like to express my gratitude to the Civil Engineering and Environmental Department of University of Massachusetts Amherst for the valuable education and experience over the five and a half years of my college career.

ABSTRACT

Parametric Study of Integral Abutment Bridge Using Finite Element Modeling

MAY 2021

ASAKO TAKEUCHI, B.S., UNIVERSITY OF MASSACHUSETTS AMHERST

M.S.C.E., UNIVERSITY OF MASSACHUSETTS AMHERST

Directed by: Professor Scott Civjan

A parametric study of single-span integral abutment bridge (IAB) was conducted using finite element analysis to explore the effects of various load conditions, bridge geometries, and soil properties. This study investigated the difference between the live load distribution of traditional jointed bridges and integral abutment bridges (IABs) under HL-93 truck component load. The results showed that AASHTO live load distribution factors (LLDFs) were overly conservative by up to 50% to use for IABs. LLDFs for IABs proposed by Dicleli and Erhan (2008) matched well for interior girder moment, but they were unconservative for exterior girder moment by up to 20% for the bridges studied. The study further investigated the effects of various parameters on the IAB responses under dead, live, and thermal loads and load combinations specified by AASHTO. The results of this study are limited to short to moderate single-span straight bridges under dead, live, and thermal loads. Due to a fixity of superstructure and abutments in IABs, the bridge response to each loading is influenced by the relative stiffness of superstructure to substructure. Under combined loads, the amount of each load effect varied depending on superstructure and substructure stiffness, but the critical load combination for each bridge response was determined in this study. Yielding of piles seems unavoidable for IABs built on sand under combined loads even after the change of pile size or pile orientation,

but replacing the soil around top 3m (10ft) of piles with softer material is effective to reduce the significant amount of pile moment for IABs built on sand foundation soil. This thesis includes some design recommendations based on the findings of this study.

TABLE OF CONTENTS

Page

LIST OF TABLES

Page

LIST OF FIGURES

Page

CHAPTER 1

INTRODUCTION

Integral abutment bridges (IABs) are jointless bridges in which superstructure deck is cast monolithically with abutments and embedding the girder ends, resulting in fixity between the superstructure and substructure. IABs have been widely used throughout the United States as an alternative to traditional jointed bridges due to their efficiency and durability. Traditional jointed bridges are known to have expensive repair costs due to the corrosion of the bridge elements below failed bridge joints. In states with harsh winter weather, corrosion damage is significantly accelerated by use of de-icing agents. The elimination of expansion joints in IABs minimizes the problems associated with failing bridge joints. IABs can also result in significant initial cost savings due to the minimally invasive foundations which avoid coffer dams, dewatering requirements, and environmental impacts. Furthermore, IABs are found to be more resilient bridges that are reported to perform well under earthquake and flood conditions (Wood 2015; Civjan et. al 2014a, 2014b). Due to their various advantages, IABs have become the bridge of choice for standard short to moderate span bridges in many states. However, even though IABs have been used in the USA since 1938 (Burke 2009) and are common structures in recent years, universal design guidelines are not well established, and appropriate design methods and assumptions are not clear. This has resulted in Departments of Transportation (DOTs) using different provisions on IAB designs based on their individual experiences (Conboy 2005; Kunin 2000; Maruri and Petro 2005).

A detailed survey by Maruri and Petro (2005) complied responses from 39 states and reported the variations in design standards of IABs. The allowable maximum span

length for prestressed concrete and steel girder-fully IABs ranged from 18.3 m (60 ft) to 61 m (200 ft) and from 19.8m (65 ft) to 91.4 m (300 ft), respectively. Regardless of the type of girder, maximum skew angle ranged from 15 to 70 degrees, and maximum curvature ranged from 0 to 10 degrees. Among the 39 states which responded to the survey, there was no consistency in the orientation of piles; 33 percent of states orient the piles with strong axis parallel to the centerline of bearing, 46 percent orient the piles with the weak axis parallel to the centerline of bearing, 8 percent leave it to the discretion of the engineer, and the remaining did not comment or noted their use of symmetric piles (Maruri and Petro 2005).

Construction details of IABs also vary (Kunin 2000; Conboy 2005; Soltani 1992). For example, in constructing steel girder IABs, some details connect the bottom flange of the girder to the abutment, and others rigidly connect the bottom flange of the beam by welding it to the top of pile (though this detail can result in much higher pile stresses depending on the amount of dead load end girder moment transferred (Kalayci 2012). When precast concrete girders are used, some states provide a neoprene pad, and other states use anchor bolts with leveling plates and nuts. Other details include casting concrete pedestals with an erection pad on top of the first abutment pour or providing a drilled-in reinforcing bar. Details of pile installation also differ by DOTs. The details include driving or vibrating piles in the existing subgrade, pre-drilling an oversized hole infilled with a variety of materials (sand, natural bentonite, bentonite slurry, pea stone, crushed stone, or no infill), or providing a pre-excavation to assist the pile-driving to retain the backfill material. There is also a variation in the orientation of piles, as previously mentioned. The strong-axis orientation results in a lower percentage of yield

moment in the pile, but the weak-axis orientation results in a lower value of moment (Quinn and Civjan 2017). These variations in construction details appear to result from individual experiences and design preferences. These details have also changed over the years within individual DOTs, so previous reports may no longer be representative of current design.

The soil-structure interaction present in IABs is also not fully understood. The substructure of IABs is subjected to both short term (daily) and long term (seasonal) cyclic thermal loading and the resulting frame action of the bridge. Soil properties under these cyclic loads are often complex and nonlinear, making it difficult to predict the soil-structure interaction. Although finite element modeling is a useful and powerful tool for analyzing and understanding such behavior under various loading conditions, it is only as accurate as the modeling assumptions. In addition, using complicated three-dimensional (3-D) finite element models (FEMs) can be time-consuming and expensive and is not typical practice in the design of short to moderate span bridges. When designing bridges for live loads, most engineers prefer to use two-dimensional (2-D) finite element bridge models and live load distribution factors (LLDFs) available in AASHTO design specifications for simply supported bridges (SSBs) (AASHTO 2017). These factors were not developed for IABs, and their use is only appropriate under the assumption that integral abutments increase load distribution between girders or have minimal effect on girder distribution in positive moment regions of longer spans. This is likely an overly conservative assumption for shorter spans.

Due to an uncertainty in IAB behavior and a lack of consistency in design standards, many research studies have been conducted on IABs over the past years,

including field studies and computer modeling. A wide range of studies were conducted investigating various loading effects on the performance of IABs and soil-structure interaction; live load (Kalayci et. al 2011; Dicleli and Erhan 2008; Dicleli and Erhan 2009; Dicleli and Erhan 2010), thermal load (Kalayci et. al 2012; Salman and Issa 2021; Civjan et. al 2014a, 2014b), and seismic load (Kozak 2018). There were also several parametric studies analyzing the curvature, skew, pile orientation, and soil effects on IAB behavior (Kalyci et. al 2012; Quinn and Civjan 2017; Deng et. al 2015; Dicleli and Erhan 2008).

One of the field studies conducted by Civjan et. al (2013) investigated the substructure response of two straight steel I girder IABs in Vermont under seasonal thermal changes, and the bridges were monitored for thirty months. The field data showed a range of substructure deformations under similar thermal conditions due to a variation in soil properties over time; shifting of displacement was observed in subsequent years, indicating a permanent offset of abutments. Thus, calibration of FEMs for a specific soil condition would not be able to capture a long-term bridge response unless long-term change in soil properties was also modeled (Civjan et. al 2013; Breña et. al 2007).

Among the number of research studies conducted the live load effects of IABs, Dicleli and Erhan (2008, 2009, 2010) conducted a series of parametric studies to investigate the live load distribution for straight IABs and compared the results with the live load distribution factors (LLDFs) developed by AASHTO for jointed bridges. The parametric studies primarily focused on concrete girder IABs with a wide range of superstructure and substructure geometric parameters and soil stiffness. The study

concluded that the superstructure-abutment continuity in IABs generally improved the live load moment distributions among the girders, and AASHTO LLDFs produced a conservative estimate of girder moment for short-span IABs (Dicleli and Erhan 2010). Additionally, Dicleli and Erhan (2008) found that substructure and soil stiffness have negligible effects on the live load distributions among the girders of IABs built on clay and concluded that this finding is also applicable to IABs built on cohesionless soil such as sand even though cohesionless soil was not included in the study.

Despite the number of parametric studies conducted to investigate various effects on IABs under each loading case, the behavior of IABs under the combinations of the loads has not been explored. This research includes additional soil properties, load conditions, and bridge geometries that were not considered in the previous parametric studies conducted by Dicleli and Erhan (2008, 2009, 2010), Kalyci et. al (2011, 2012), Civjan et. al (2014), or Quinn (2017). The purpose of this research study is to perform finite element analysis of IABs to investigate some of the differences between jointed bridge and IAB performance. This will include:

- Expand on previous parametric IAB research (Dicleli and Erhan 2008; 2009; 2010; Quinn et. al 2017) to include a wider range of soil properties, effect of concrete cracking on both concrete and steel girder IABs,
- Evaluate the applicability of AASHTO LLDF and proposed LLDF equations for IABs, with comparisons made and FEM checks with the Dicleli and Erhan's results,
- Study the effects of superstructure and substructure stiffness on IAB under the combination of dead, live, and thermal loads.

This research will consider a wide range of soil types (soft clay to dense sand) using established modeling methods by Dicleli and Erhan (2008). A series of parametric studies conducted by Dicleli and Erhan (2008, 2009, 2010) focused primarily on precast concrete girder IABs on clay foundation soil, using 3-D elastic finite element modeling; however, this current research will investigate steel girder IABs, sand foundation soil, and the effect of concrete cracking. Additionally, this research will include considerations of dead, live, and thermal load effects, as well as the combination of these loads. Comparisons between 3-D and 2-D models, and elastic and inelastic models will be made to evaluate the level of analysis that is appropriate for design consideration.

The rest of the thesis is organized as follows; Chapter 2 discusses the FEM methods and parameters used in this research. Chapter 3 presents the results of SSBs that are used as reference when IABs are considered. Chapter 4 presents and discusses the results of parametric study on single span straight IABs under the load of HL-93 truck component. Chapter 5 presents and discusses the results of parametric study on single span straight IABs under combined loads. Chapter 6 presents conclusion of this study and design recommendations. Lastly, Chapter 7 includes a list of all references in this thesis.

CHAPTER 2

FEM METHODS

This chapter describes the bridge parameters and FEM methods used in this research. The FEMs were created using the finite element analysis software, CSiBridge v21.2.0. The following sections describe the modeling method of structures, soil, and loads. The FEMs created in this study was verified using the literature results.

2.1 General Bridge Dimensions and Parameters Considered

Two types of single span slab on girder IABs were considered in this study; one consists of precast/prestressed concrete girders and another one consisting of steel plate girders. General bridge dimensions modeled in this research are summarized in Table 0.1. The properties presented in Table 0.1 remained unaltered in all FEMs created in this research. Typical bridge width, girder spacing, and slab thickness were selected for single span straight slab on girder bridges.

Table 0.1: General Properties of IABs used in the Analysis

Properties	**Description**
Bridge Width [m (ft)]	9.6 (31.5)
Slab Thickness [m (ft)]	0.2 (0.7)
Girder Spacing [m (ft)]	2.4 (7.9)
Number of Girders	4
Number of Piles per Girder	1
Pile Length [m (ft)]	12 (39.37)
Abutment Thickness [m (ft)]	1 (3.28)
Abutment Height [m (ft)]	3 (9.84)
Unit Weight of Backfill Soil [kN/m^3 (lb/ft^3)]	20 (127.32)

Table 0.2 shows the study parameters considered. The parametric study conducted by Dicleli and Erhan (2009 and 2010) was used as a basis for these parameters and geometries of IABs to make a direct comparison for the initial model verification. Three different AASHTO concrete girder sizes were used, and their dimensions are specified in Table 0.3. The variation of span length was selected based on the maximum span length that bridges with AASHTO Type II, IV, and VI girder sizes can accommodate based on the Precast Concrete Institute (PCI) Bridge Design Manual (PCI 2011). As presented in Figure 0.1, for girder spacing of 2.4m (7.87ft), maximum span length for bridges ranged from 18.3m (60ft) to 45.7m (150ft), thus, span lengths of 20, 30, 40m (65, 100, 135 ft) were selected for this study. For steel I girder IABs, small, medium, and large steel girder sizes were selected according to the typical steel I girder sizes recommended by National Steel Bridge Alliance (NSBA 2013) for 20, 30, 40 m (65, 100, 130 ft) span lengths, respectively, and their dimensions are specified in Table 0.4. Even though the smallest girder size is not appropriate for the longest span length or vice versa, FEMs with these combinations were also modeled for the purpose of the parametric study.

Material properties used in FEMs are presented in Table 0.5. Concrete strength of 27.6MPa (4ksi) was used for the deck and abutment, and higher concrete strength, 41.3MPa (6ksi) was used for AASHTO concrete girders. For steel elements, 345MPa (50ksi) steel was used. Table 0.6 presents the composite superstructure moment of inertia (I_g) using nominal material properties. These values are directly related to the relative stiffness of superstructure; a larger value of moment of inertia results in a superstructure with higher flexural stiffness. Steel girder IABs have smaller values of moment of inertia than concrete girder IABs with the same span length, and thus, steel girder IABs are more

flexible for the bridge models created for this research. For cracked section properties, 0.5 I_g for concrete girders and 0.35 I_g for slab and abutment were assumed.

Table 0.2: Parameters Considered in Analysis

Parameters	**Precast Concrete Girder Bridge**	**Steel I Girder Bridge**
Span Length [m (ft)]	20, 30, 40 (65.6, 98.4, 131.2)	20, 30, 40 (65.6, 98.4, 131.2)
Girder Type	AASHTO Type II, IV, VI	Small, Medium, Large
Foundation Soil	Clay: Soft, Medium, Medium-Stiff, Stiff Sand: Loose, Medium, Stiff	Clay: Soft, Medium, Medium-Stiff, Stiff Sand: Loose, Medium, Stiff
Pile Orientation	Strong and Weak Axis Bending	Strong and Weak Axis Bending
Pile Size [mm x kg/m (in x lbs/ft)]	HP250x85 (HP10x57) HP310x125 (HP12x84)	HP250x85 (HP10x57) HP310x125 (HP12x84)
Concrete Crack	Uncracked/Cracked	Uncracked/Cracked

Table 0.3: Details of Precast Concrete Girder Sections

Girder Sizes	**Type II**	**Type IV**	**Type VI**
	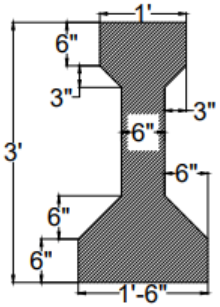	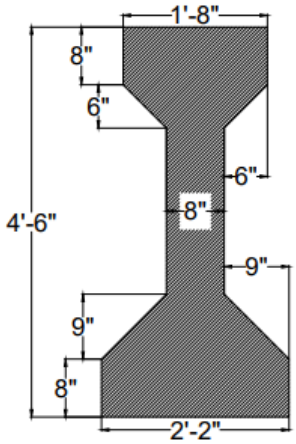	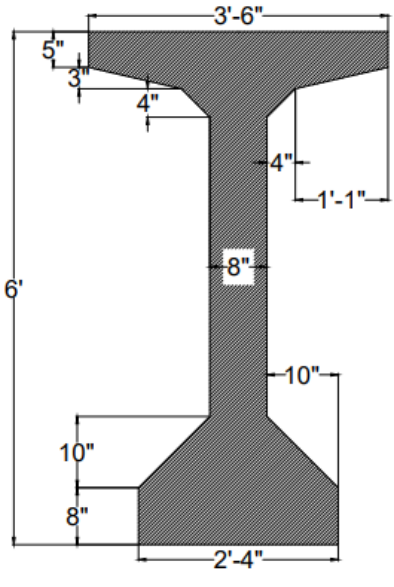

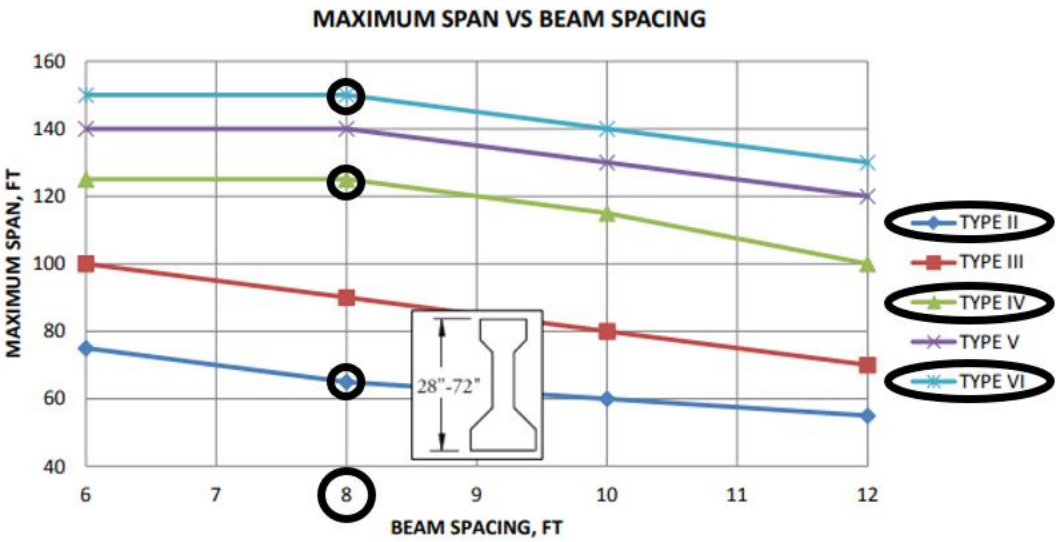

Figure 0.1: Maximum Span vs Beam Spacing (PCI 2011)

Table 0.4: Details of Steel Girder Sections

	Small	**Medium**	**Large**
	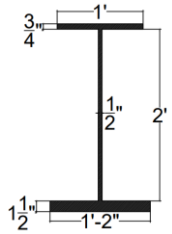	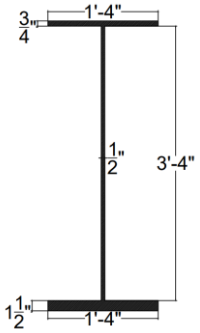	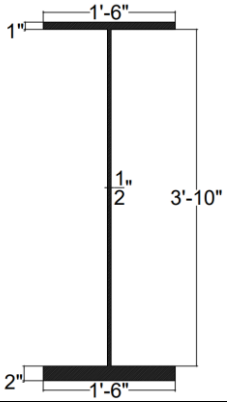
Top Flange	12”x3/4”	16”x3/4”	18”x1”
Bottom Flange	14”x1 ½”	16”x1 ½”	18”x2”
Web	24”x1/2”	40”x1/2”	46”x1/2”

Table 0.5: Material Properties used in FEMs

	Strength [MPa (ksi)]	Elastic Modulus [GPa(ksi)]	Poisson's Ratio	Unit Weight [kg/m^3(kip/ft^3)]	Coefficient of Thermal Expansion [10^{-6} °C^{-1} (10^{-6} °F^{-1})]
Concrete Deck/ Abutment	27.6 (4)	24.9 (3605)	0.2	23.6 (0.15)	9.9 (5.5)
Concrete Girders	41.3 (6)	30.4 (4415)	0.2	23.6 (0.15)	9.9 (5.5)
Steel Girders/Piles	345 (50)	200 (29000)	0.3	77 (0.49)	11.7 (6.5)

Table 0.6: Moment of Inertia of Bridge Composite Section Based on Nominal Properties

		Moment of Inertia [mm^4 (in^4)]
Concrete	Type II	3.824e11 (9.187e5)
	Type IV	1.310e12 (3.147e6)
	Type VI	2.744e12 (6.592e6)
Steel	Small	2.317e11 (5.567e5)
	Medium	6.307e11 (1.515e6)
	Large	1.076e12 (2.585e6)

2.2 Modeling of Structures

Three-dimensional (3-D) FEMs of IABs were created in CSiBridge v21.2.0, using the general dimensions and the study parameters described in Section 1. The abutments were assumed to be supported by steel H-piles as they are commonly used in IAB construction. The concrete deck, abutments, and steel girders were modeled using four-node thin shell elements with six degrees of freedom (DOFs) at each node, and concrete girders and piles were modeled as 3-D frame elements with six DOFs at each node. Frame elements for concrete girders and shell elements for steel girders were used for this research. The geometry of steel girders allowed modeling with shell elements in steel

girder IABs, and thus shell elements were used for a better accuracy of the results. Slab and girders were meshed at every 0.5 m (1.64 ft) longitudinally. Additionally, the slab was meshed at every 0.6 m (1.97 ft) transversely to align with the truck wheels for live load analysis. The abutments are divided into equal 0.6 m (1.97 ft) square shell elements. Girders are also attached to the abutments at nodes along the girder depth using rigid links with all degrees of freedom constrained to model transfer of moment with consistent deformations from superstructure to substructure, as shown in Figure 0.2. The typical FEMs of prestressed concrete and steel girder IABs used in this study are shown in Figure 0.3 and Figure 0.4, respectively.

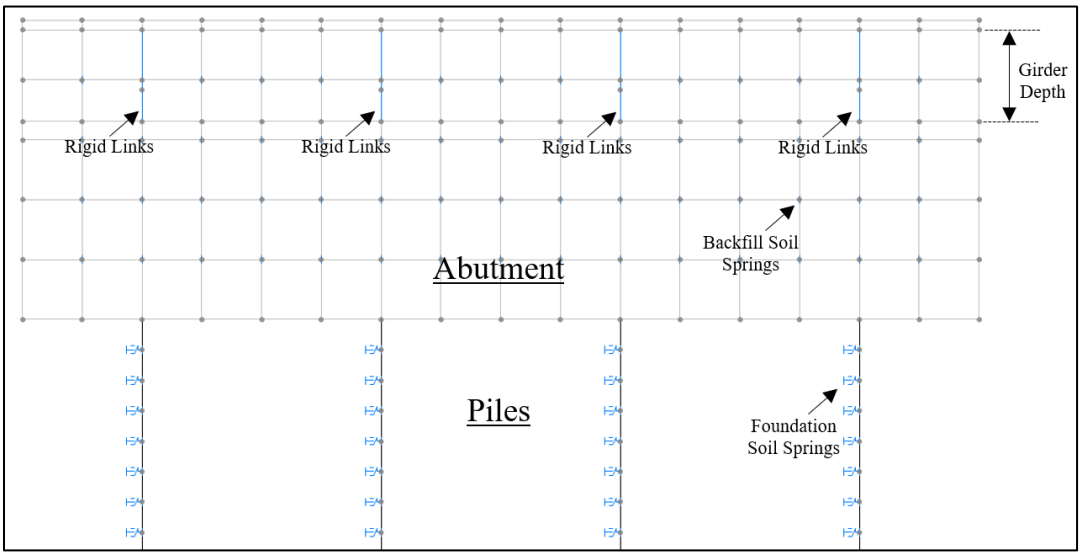

Figure 0.2: Connection of Substructure and Superstructure in Typical IABs

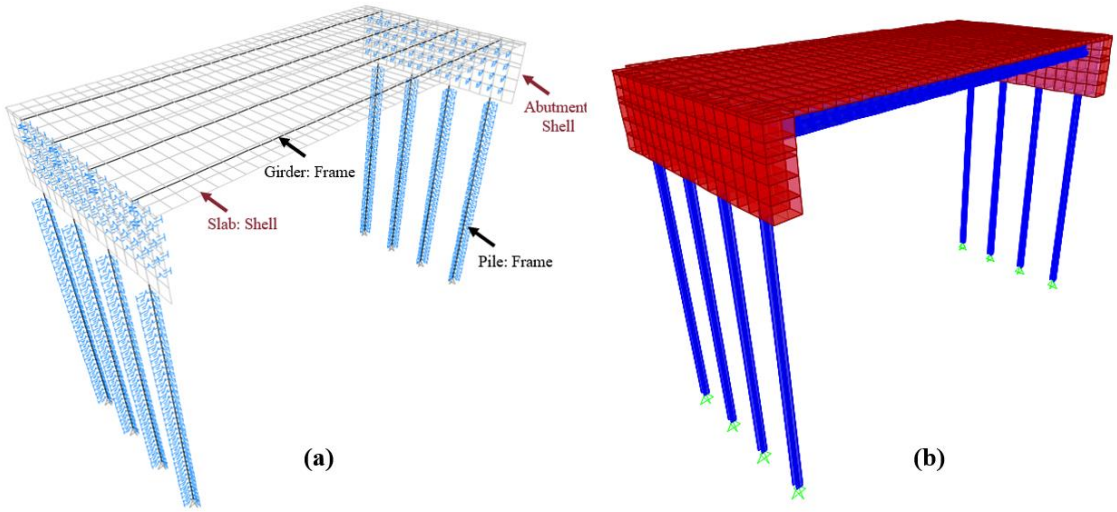

Figure 0.3: FEMs of Typical Prestressed Concrete Girder IABs in (a)Element View and (b)Extruded View

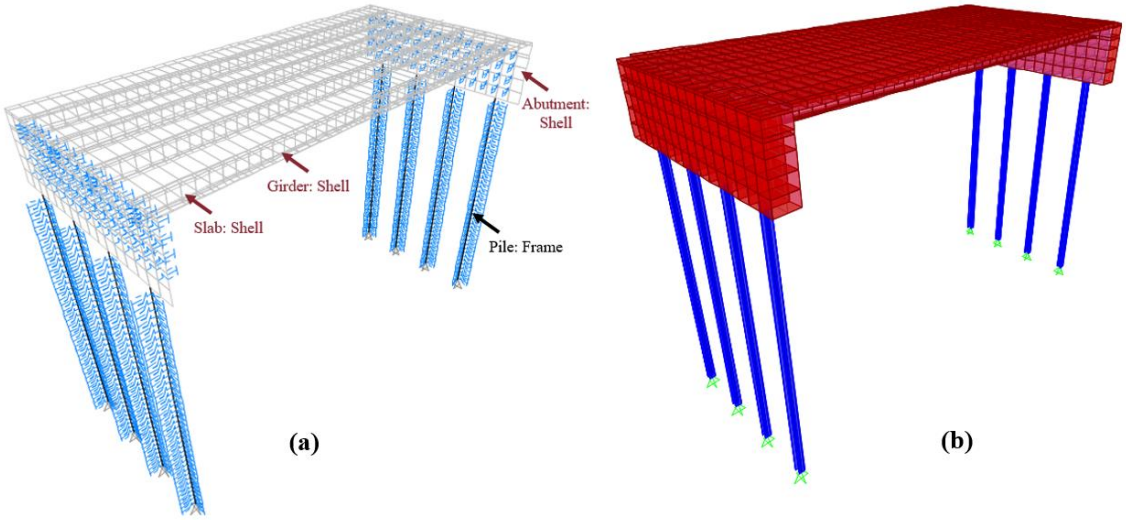

Figure 0.4: FEMs of Typical Steel Girder IABs in (a)Element View and (b)Extruded View

2.3 Modeling of Plastic Hinges

Plastic hinges were included to account for the yielding of piles in this study. The moment-curvature relationships defined for FEMs should ideally include the effects of axial load, residual stress, and strain hardening. However, this is not straightforward to include, so some assumptions were made to match experimental results in the literature for this study. The nominal yield and plastic moment capacities ($M_{y\_nominal}$ and $M_{p\_nominal}$) of the pile can be computed by multiplying elastic section modulus (S_x and S_y) and plastic section modulus (Z_x and Z_y) by the yield strength of steel (F_y), respectively. The nominal yield and plastic curvature capacities ($\phi_{y\_nominal}$ and $\phi_{p\_nominal}$) of the pile are computed by the ratio of strain to depth of neutral axis. Assuming a linear strain distribution through the cross section, the moment-curvature relationship for nominal properties of the piles was determined. However, if piles are also subjected to axial loads, the capacity of the piles decreases. Since the H-piles in this study were subjected to axial loads resulting in 10 to 30% of pile axial yield capacity (P_y) due to dead and live loads (see Section 3.3 for more details), the moment-curvature relationships were modified based on the reduced yield and plastic moment and curvature ($M_{y\_reduced}$, $M_{p\_reduced}$, $\phi_{y\_reduced}$, and $\phi_{p\_reduced}$) obtained from literature (Albhaisi 2012). To avoid changing axial load in piles in each mode, the axial load of 30% of P_y was considered for all FEMs since this could result in earlier yielding of piles in some models.

Literature data of yield and plastic moment capacities of the two HP sections used in this study about strong and weak-axis orientations based on analytical analysis for the cases of no axial load (0% of P_y) and 30% axial load of P_y are listed in Table 0.7 (Albhaisi 2012). Since the H-piles in this study were subjected to axial load, the nominal

capacity (0% of P_y) is not ideal. The values in the table include factors such as residual stresses and strain hardening without needing to model them explicitly. Due to these effects, the reduced plastic capacity of the H-piles can reach close to the nominal plastic capacity of H-piles even after the axial load consideration, and thus, reducing the entire nominal moment-curvature relationship by 30% would be overly conservative.

Figure 0.5 shows the four moment-curvature relationships generated for HP310x125 with the weak-axis orientation. To generate the curves beyond the yield capacity, three assumptions were considered for the piles used in this study, as shown in Figure 0.5, in addition to the nominal moment-curvature relationship (Case 1). Using the literature data points for the axial load of $0.3P_y$ presented in Table 0.7, curves were generated by interpolating the ratio from $M_{y\_reduced}/M_{y\_nominal}$ to $M_{p\_reduced}/M_{p\_nominal}$ by linear interpolation (Case 2 in Figure 0.5) and polynomial interpolation with the 2^{nd} power (Case 3 in Figure 0.5), respectively. Even though this is not realistic as mentioned previously, Case 4 in Figure 0.5 provides a moment-curvature relationship assuming a straight 30% of P_y reducing both $M_{y\_nominal}$ and $M_{p\_nominal}$: the curve of Case 1 scaled by 0.7.

The results can vary depending on the assumptions used on this relationship. For the reasons previously stated, Case 2 or Case 3 are more ideal than Case 1 and 4. The data points presented with markers in Figure 0.5 are the maximum pile moment recorded using all assumptions for one particular IAB, which resulted in one of the highest pile moments in the study, and the results are listed in Table 0.8. The results showed that the resulting pile moment did not differ significantly between Case 2 and 3. The curve fit better with the curve obtained from literature experimental data on wide-flange steel

sections with weak-axis orientation (Lybas 1970), thus, the polynomial interpolation (Case 3) was used. Figure 0.5 is limited to the results of HP310x125 with the weak-axis orientation, however, HP250x85 as well as the strong-axis orientation were also plotted, using polynomial interpolation.

The moment-curvature relationships were then normalized by $M_{y\_reduced}$ and $\phi_{y\_reduced}$. Figure 0.6 presents the normalized moment-curvature relationship used in FEMs for strong and weak-axis orientations. The results showed that HP250x85 and HP310x125 have identical normalized moment-curvature curves with the axial load of $0.3P_y$; this also agreed with the literature finding (Dicleli and Albhaisi 2004). Therefore, the same plastic hinge properties were used for all bridge models regardless of pile sizes, shown in Figure 0.6.

Table 0.7: Yield and Plastic Moment of HP Sections (Albhaisi 2012)

Pile Size	**Pile Orientation**	**P/P_y**	**ϕ_y (m^{-1})**	**M_y (kN-m)**	**ϕ_p (m^{-1})**	**M_p (kN-m)**
HP250x85	Weak	0 (Nominal)	0.0131	111.9	0.1144	168.2
		0.3 (Reduced)	0.0092	78.3	0.1040	166.0
	Strong	0 (Nominal)	0.0135	329.0	0.1176	371.6
		0.3 (Reduced)	0.0095	230.3	0.0672	307.1
HP310x125	Weak	0 (Nominal)	0.0109	194.7	0.0954	292.8
		0.3 (Reduced)	0.0077	136.3	0.0868	289.1
	Strong	0 (Nominal)	0.0110	589.0	0.0957	665.4
		0.3 (Reduced)	0.0077	412.3	0.0547	549.8

Note: Yield and plastic curvature and moment for $P/P_y = 0$ are $\phi_{y\_nominal}$, $\phi_{p\_nominal}$, $M_{y\_nominal}$, and $M_{p\_nominal}$, and yield and plastic curvature and moment for $P/P_y = 0.3$ are $\phi_{y\_reduced}$, $\phi_{p\_reduced}$, $M_{y\_reduced}$, and $M_{p\_reduced}$.

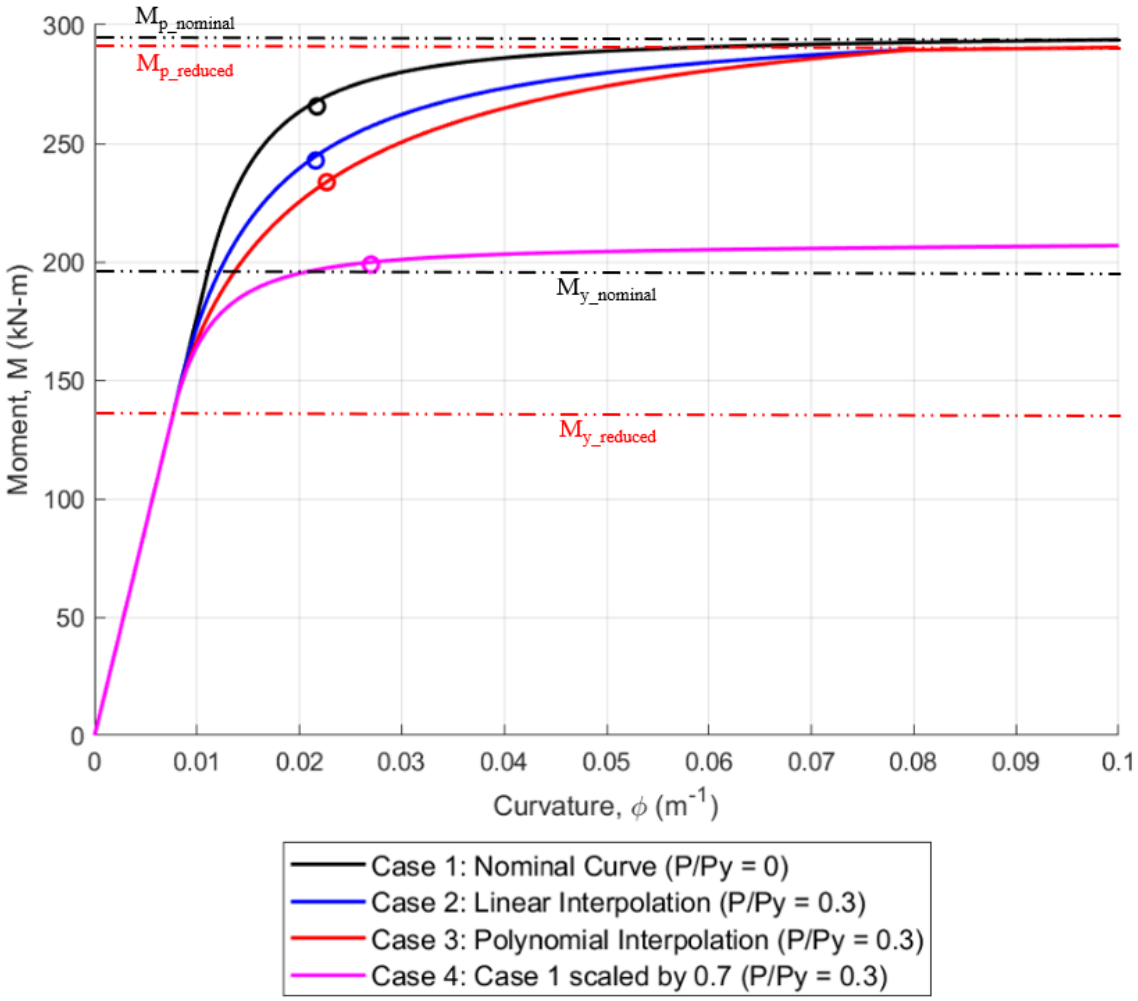

Figure 0.5: Assumptions made for the Moment-Curvature Relationship for HP310x125 with Weak-Axis Orientation

Table 0.8: The Results of Preliminary Plastic Hinge Analysis

Pile Size	Case	Maximum Pile Moment (kN-m)
HP310x125	1	265.6
	2	242.7
	3	233.6
	4	195.8

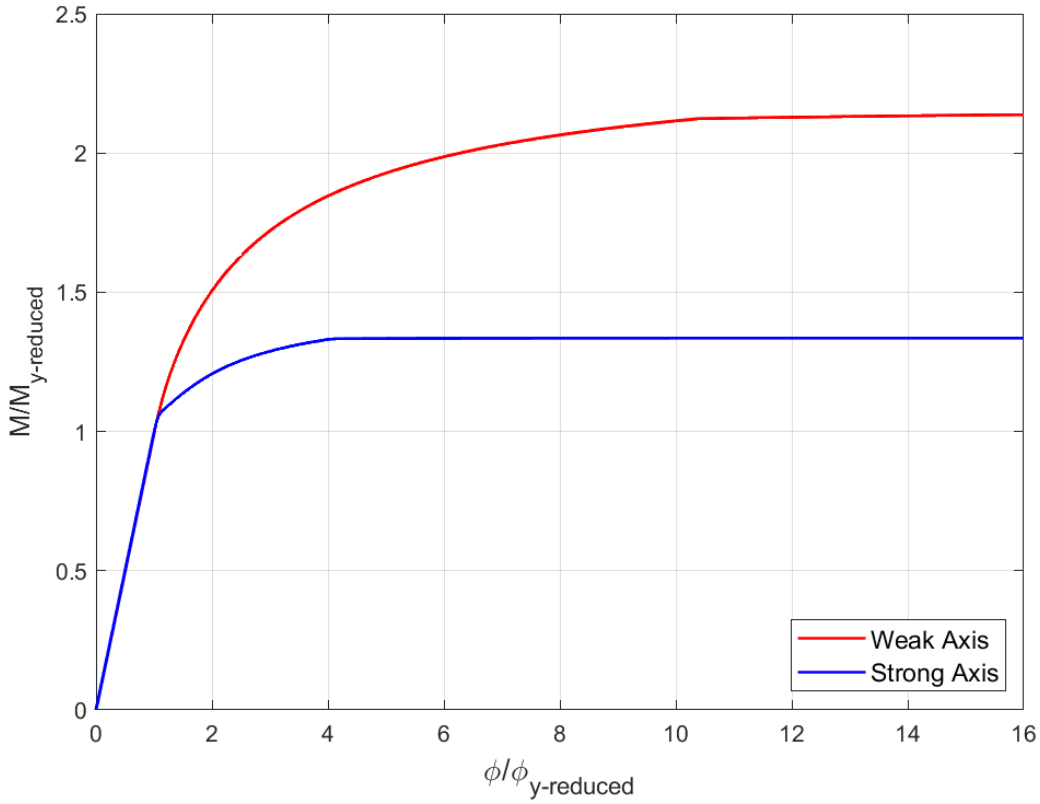

Figure 0.6: Normalized Moment-Curvature Relationship for HP sections
Note: Polynomial interpolation assumption was used.

2.4 Modeling of Soil

Soil-structure interaction in substructure of IABs was simulated using a set of springs on abutment and piles. This section describes the modeling methods of backfill and foundation soil in this research.

2.4.1 Modeling of Backfill Soil

To simulate the backfill-abutment interaction, springs were attached perpendicular to the nodes along the height and width of abutments. The springs were

defined by force-deformation curves (p-y curves) that are calculated for the depth of each node. The p-y curves can be computed by the following equation,

$$F = K \cdot \sigma' \cdot w \cdot h \qquad \text{Equation 0-1}$$

where F = effective lateral soil resistance at the node of a tributary area with dimensions of w(width) and h(height), K = lateral earth pressure coefficient, and σ' = effective vertical earth pressure. For this research, the backfill soil was assumed to be medium dense sand (friction angle = 37° and unit weight = 20kN/m^3 [128.5lb/ft^3]). Lateral earth pressure coefficient, K depends on the amount of displacement, and thus, the variation of K for medium dense sand defined by Clough and Duncan (1991) was used to calculate the p-y curves. The nonlinear variation of K used in this study is presented in Figure 0.7. Active pressure was accounted as an initial pressure with p-y curves offset accordingly and applied on each shell element.

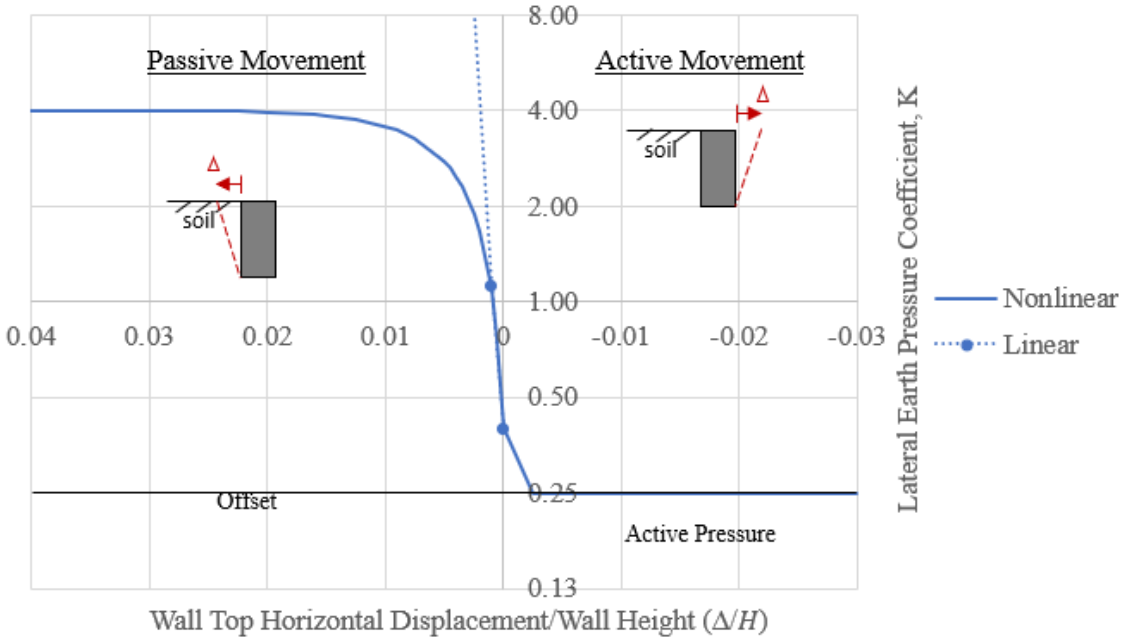

Figure 0.7: Lateral Earth Pressure Coefficient K as a function of Δ/H

For only the parametric study of IABs under the HL93 design truck load (Chapter 4), the nonlinear curve of lateral earth pressure coefficient, K was simplified to be a linear curve presented in Figure 0.7. For linear backfill springs, only passive pressure was considered on the abutment. Under the truck load, abutments move towards the center of the bridge, and only the abutments above the centroid of deck are subjected to active pressure. The movement of the abutment above the superstructure centroid is expected to be small under the single case of truck load, thus, active pressure was ignored. The linear curve of K in Figure 0.7 was plotted following the assumption made by Dicleli and Erhan (2008). Using the two data points shown in the Figure 0.7 (K = 0.4 and 1.125 for $\Delta/H = 0$ and 0.001), the linear curve of K was determined. The p-y curves were computed using the linear curve of K.

2.4.2 Modeling of Clay Foundation Soil

To simulate the soil-pile interaction, springs were attached in two perpendicular directions at every 0.3m (1ft) depth along the pile depth. Four stiffnesses of clay were modeled in this study: soft, medium, medium stiff, and stiff clay. The properties of the clay are summarized in Table 0.9. The p-y curve developed by Matlock (1970) for soft to stiff clay was used in this study and defined by the following equation,

$$p = 0.5 p_u \left(\frac{y}{y_c}\right)^{\frac{1}{3}} \qquad \text{Equation 0-2}$$

where p_u = ultimate soil resistance per unit length of pile and $y_c = 2.5\varepsilon_c d_p$; ε_c = strain (0.02, 0.01, 0.0065, 0.0050 for soft, medium, medium stiff, and stiff clay were used

respectively for the corresponding undrained strength of clay (Peck et. al 1974)) and d_p = pile width. p_u can be computed by the following equation Matlock (1970),

$$p_u = \left(3 + \frac{\gamma x}{C_u} + 0.5\frac{x}{d_p}\right) C_u d_p \qquad for\ x < x_r \qquad \text{Equation 0-3}$$

$$p_u = 9 C_u d_p \qquad for\ x \geq x_r \qquad \text{Equation 0-4}$$

where γ = unit weight of soil, x = depth, C_u = undrained strength of clay, and x_r = critical depth. The values of C_u, 20, 40, 80, and 120 kPa were selected for as soft, medium, medium stiff, and stiff clay, respectively (Peck et. al 1974). The critical depth, x_r for each soil was computed by the following equation (Matlock 1970)),

$$x_r = \frac{6 d_p}{\frac{\gamma d_p}{C_u} + J} \qquad \text{Equation 0-5}$$

where γ = unit weight of soil and J= empirical factor; 0.5 for soft clay and 0.25 for stiff clay (Matlock 1970). x_r are 0.04m (0.13ft) for soft clay and 0.02m (0.07ft) for stiff clay, and x_r for medium and medium stiff clay were assumed to fall between these values. These critical depths are much shallower than the depth of piles, and therefore, Equation 0-4 was used to calculate p_u. Using this p_u, Equation 0-2 was used to calculate the p-y curves for each clay stiffness. The p-y curves of clay foundation soil do not depend on the depth of nodes at which springs are attached, thus, they are consistent along the depth of the pile. Figure 0.9 presents the P-Y curves plotted for each clay stiffness and HP section.

As similarly performed for backfill springs, the nonlinear p-y curves of clay were simplified to be linear curves for the parametric study of IABs under the truck load (Chapter **Error! Reference source not found.**), since the lateral pile deformation under

the truck load is expected to be small. This simplification was only made for Chapter **Error! Reference source not found.**, and nonlinear curves were used for Chapter **Error! Reference source not found.**. Figure 0.8 presents the typical nonlinear and linear p-y curves plotted for clay foundation soil. The slope of linear p-y curve (k) was defined as the ratio of half of p_u ($0.5p_u$) to y_c. Then, the linear spring stiffness was determined by multiplying the slope of the linear curve by the tributary length (0.3m [1ft]).

Table 0.9: Properties of Clay Foundation Soil

Clay Stiffness	**Undrained Strength, C_u [kPa (lb/ft^2)]**	**Strain, ε_c**	**Linear Slope, k [kPa (lb/ft^2)]**
Soft	20 (418)	0.02	1800 (37600)
Medium	40 (835)	0.01	7200 (150300)
Medium Stiff	80 (1670)	0.0065	22150 (462400)
Stiff	120 (2505)	0.0050	43200 (901900)

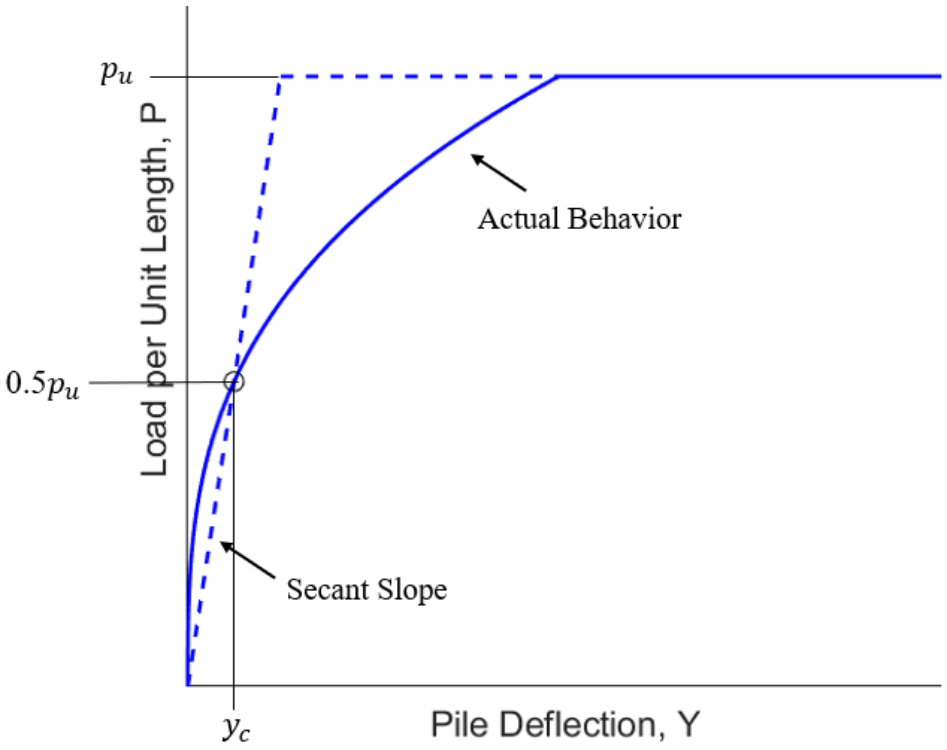

Figure 0.8: Typical Linear and Nonlinear P-Y Curve for Clay Foundation Soil

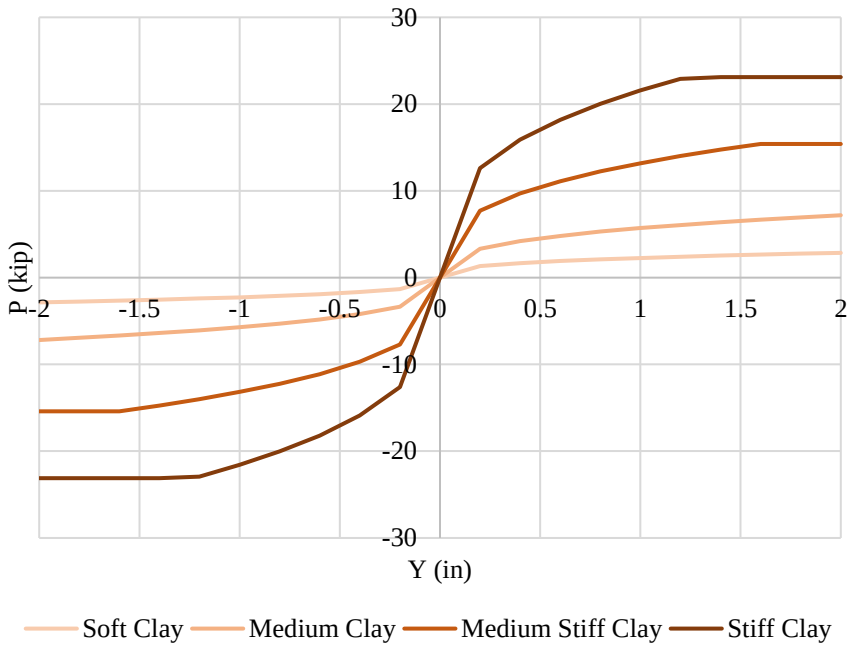

Figure 0.9: Nonlinear P-Y Curves of Clay Foundation Soil
Note: Soil Springs for HP310x125

2.4.3 Modeling of Sand Foundation Soil

Cohesionless sand soil around piles was modeled using nonlinear springs used in previous UMass research by Kalayci et al. (2011 and 2012), Civjan et.al (2007 and 2014), and Quinn and Civjan (2017). Springs were attached in two perpendicular directions at every 0.3m (1ft) depth along the pile depth to simulate the soil behavior around the pile. The p-y curves for these springs were designed using the hyperbolic tangent method described by the American Petroleum Institute (API 2014), as follows:

$$F = Ap_u \tanh\left(\frac{k_1 zy}{Ap_u}\right) L_p \qquad \text{Equation 0-6}$$

where A = empirical factor ($A = 3 - 0.8\left(\frac{z}{D}\right) \geq 0.9$), D = pile width, p_u = estimated ultimate lateral soil resistance, k_1 = soil strength modulus, z = soil depth from the top of the soil layer to the specified location, y = deflection along horizontal axis, and L_p = length of pile section. The estimated ultimate lateral soil resistance was the minimum of p_{us} and p_{ud} calculated as follows:

$$p_{us} = (c_1 z + c_2 D)\gamma' z \qquad \text{Equation 0-7}$$

$$p_{ud} = c_3 \gamma' D z \qquad \text{Equation 0-8}$$

where γ' = effective soil density, and $c_1, c_2, and\ c_3$ were calculated using the equations as follows: $c_1 = K_0 \tan\phi \sin\beta/\tan(\beta-\phi)\cos\alpha + \tan^2\beta \tan\alpha/\tan(\beta-\phi) + K_0 \tan\beta\,(\tan\phi \sin\beta - \tan\alpha)$, $c_2 = \tan\beta\,/\tan(\beta-\phi)\tan^2(45-\phi/2)$, and $c_3 = K_0 \tan\phi \tan^4\beta + K_a(\tan^8\beta - 1)$; where ϕ = friction angle, $\alpha = \phi/2$, and $\beta = 45 + \phi/2$, K_0 = at-rest earth pressure coefficient = $1 - \sin\phi$, and K_a = Rankine active earth pressure coefficient = $\tan^2(45-\phi/2)$. The p-y curves for each HP section were calculated for each depth of nodes at which springs were attached. The properties for loose, medium, and dense sand soil are summarized in Table 0.10 (Bonczar 2005), and Figure 0.10 presents the p-y curves plotted for sand foundation soil at 0.3m (1ft) depth from the top of piles.

Table 0.10: Properties of Sand Foundation Soil

	ϕ (deg)	γ' [kg/m^3 (lb/ft^3)]	k_1
Loose	30	1762 (110)	45
Medium	37	2002 (125)	97
Stiff	45	2242 (140)	220

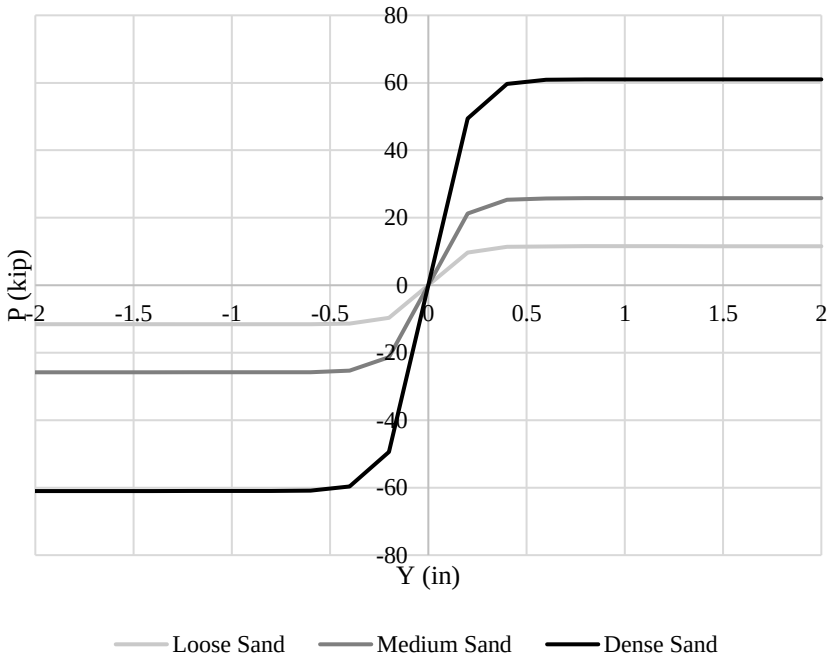

Figure 0.10: The P-Y curves of Sand Foundation Soil at 0.3m (1ft) Depth
Note: Soil Springs for HP310x125

2.4.4 Comparison of Clay and Sand Foundation Soil

The p-y curves of clay and sand foundation soil are compared in this section. Figure 0.11 shows the p-y curves for all clay (soft, medium, medium stiff, and stiff) and sand (loose, medium, and dense) foundation soil foundation used in this study at 0.3m (1ft) and 1.5m (5ft) depth from the top of pile. Generally, sand is stiffer than clay. Since clay stiffness does not depend on depth, the p-y curves are consistent throughout the depth of pile. On the other hand, sand stiffness increases at deeper depth, and thus the curve increased in Figure 0.11(b). The comparison also showed that the elastic portion of the curve for loose sand is near the elastic portion of curve for stiff clay. Therefore,

similar bridge responses are expected between IABs with loose sand and stiff clay in this study up to the point of inelastic soil response.

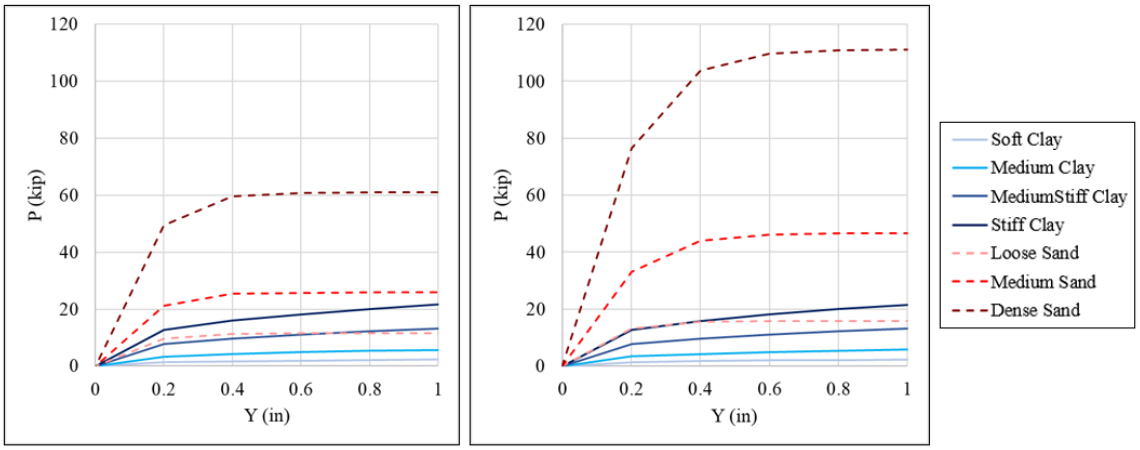

(a) Z = 0.3m (1ft) (b) Z = 1.5m (5ft)

Figure 0.11: P-Y curves of Clay and Sand Foundation Soil at (a)0.3m (1ft) and (b)1.5m (5ft) from Top of Piles

2.5 Modeling of Loads

To understand the behavior of the integral abutment bridges, three types of loads were considered in this study: dead, live, and thermal loads. Additionally, bridge responses were also analyzed under Strength 1 and Service 1 load combinations in accordance with AASHTO Bridge Design Specification (2017). This section describes the modeling procedures of each load in FEMs. All loads and load combinations were considered in the final inelastic finite element analysis of Chapter **Error! Reference source not found.**.

2.5.1 Dead Load

According to AASHTO specification (2017), there are three dead load cases: DD, DC, DW, however, the dead load considered in this study is only the weight of the concrete slab and girders (DC). Subsequent dead load, such as wearing surface and guardrails, was neglected in this study. For typical modern detailing where girders are freely sitting on bearings during construction, IABs do not have fixity at girder ends until the concrete has hardened in the upper abutment. Typically, the superstructure of IABs sits on construction joints providing pin-roller supports to the structure. After the completion of deck, girder, and substructure elements up to the joints, the top of abutment is cast with the superstructure, and fixity between the abutment and girders is provided. Due to this construction sequence, the dead load is determined by pin-roller conditions and can be determined through a simple 2-D simply supported beam analysis. From this 2-D beam analysis, reaction forces at the supports and full bridge moment were recorded. Reaction forces at the supports are assumed to be distributed among four piles, and thus, one fourth of the reaction forces was the axial dead load applied on each pile. Further details will be discussed in Section 3.

2.5.2 Live Load

Live load considered in this study is the AASHTO designated vehicular live load, HL-93 (AASHTO 2017). This includes a design truck or tandem load in addition to lane load. The preliminary analysis showed that tandem load does not govern the design for the IABs, thus, the tandem load was not considered in this study. The maximum live load effects on the bridge depends on the number of design lanes and the position of trucks.

Even though maximum of three traffic lanes can be placed for the width of the IABs analyzed in this study, bridges with three traffic lanes are not typical, thus, the possible number of design lanes considered in this study was only one or two design lanes.

The preliminary analysis showed that the number of design lanes that produced the maximum live load effects for similar four-girder bridges was two design lanes, including the effect of multiple presence factor specified by AASHTO (2017), shown in Table 0.11. Live load effect was found to be most critical when both design lanes were placed at an exterior of the bridge, 0.6m (2.0ft) away from the outer edge of the deck, and thus, the positions of lanes and trucks that produced the most critical bridge response for the 2.4 m (7.9 ft) spaced girder bridges were illustrated as per Figure 0.12.

To verify the critical positions of the trucks, the moving load analysis in CSiBridge with “Floating Lanes” was conducted. “Floating Lane” in CSiBridge is a moving load analysis feature in which it automatically moves the lanes transversely in the width of the bridge deck to determine the most critical bridge response. On the other hand, when “Fixed Lane” in CSiBridge is used, it only moves the trucks transversely within the lane that was manually defined by the user, thus, the critical bridge response is only as accuracy as the position of defined design lane. Since “Floating Lane” in CSiBridge analyzes every possible transverse and longitudinal truck positions on the bridge, it identifies critical live load effects on the bridge response, at considerably greater computational expense. Thus, the results using this feature was used to verify the most critical position of the design lanes. Table 0.12 shows the results of maximum girder bending moment for the span length 40m with AASHTO type IV with piles oriented to bend about weak axis using “Floating Lanes” and “Fixed Lanes” defined as

Figure 0.12. Since both methods were within 1% difference, the position of lanes illustrated in Figure 0.12 was found to be the most critical design lane position. For the rest of FEMs, lanes were specifically defined as fixed lanes to reduce the computational time.

Table 0.11: Maximum Girder Moment [kN-m (kip-ft)] for One and Two Loaded Lanes with Multiple Presence Factor Consideration

Clay Stiffness	**Girder Size**	**One Lane (Multiple Presence Factor = 1.2 Included)**	**Two Lanes (Multiple Presence Factor = 1.0 Included)**
Soft	Type II	1286 (948)	1574 (1160)
Soft	Type VI	896 (660)	1179 (869)

IAB parameters: Span Length = 40m, Pile = HP250x85 and Weak Axis Orientation

Table 0.12: Comparison of Maximum Girder Moment at Mid-Span using "Floating Lane" and "Fixed Lane" [kN-m (kip-ft)]

Clay Stiffness	**Floating Lane**	**Fixed Lane**	**% Difference**
Soft	1421 (1047)	1411 (1040)	0.7
Medium	1380 (1017)	1370 (1009)	0.7
Medium Stiff	1328 (978)	1317 (970)	0.8
Stiff	1287 (948)	1277 (941)	0.8

IAB parameters: Span Length = 40m, Girder = AASHTO Type IV, Pile = HP250x85 and Weak Axis Orientation

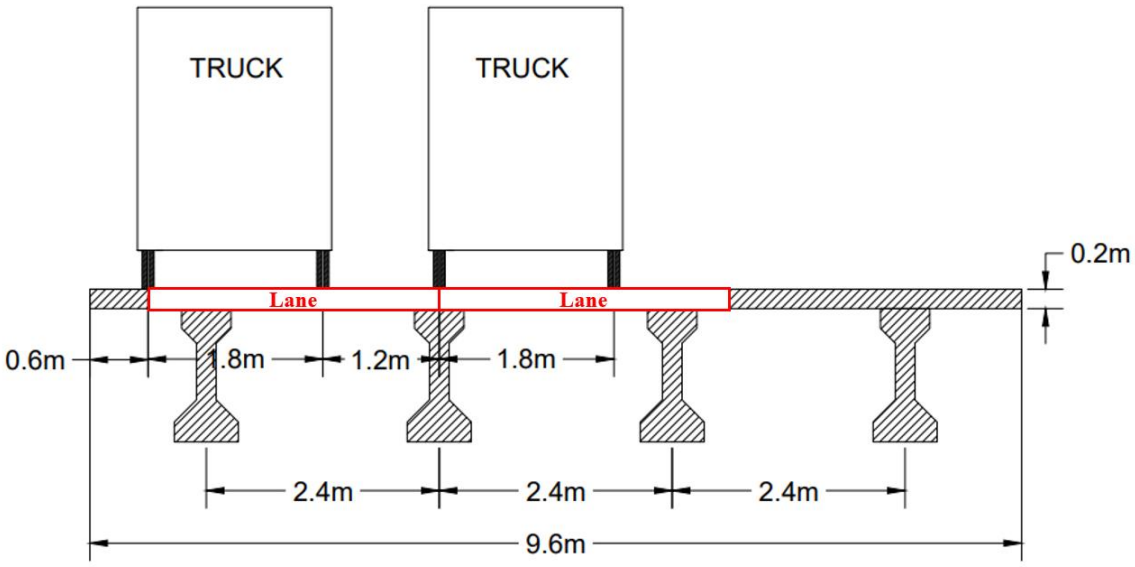

Figure 0.12: Transverse Position of HL-93 Design Lanes and Trucks

2.5.3 Thermal Load

Thermal load considered in this study is only uniform thermal loads; thermal gradient was ignored. Per AASHTO Bridge Design Specification (2017), varying thermal loads for concrete and steel bridges must be considered. The AASHTO specifies the minimum and maximum design temperatures for concrete and steel bridges for cold climate to be from -17.8°C to 26.7°C (0°F to 80°F) and from -34.4°C to 48.9°C (-30°F to 120°F), respectively. Assuming that typical construction temperature ranges from -6.8°C to 21.0°C (20°F to 70°F) defined by the Vermont Agency of Transportation IAB Design Guideline (VTran 2008), separate thermal loads were applied on each type of bridge: extreme positive temperature change of T+15.7°C (T+60°F) and extreme negative temperature change of T-21°C (T-70°F) for concrete IABs and T+37.9°C (T+100°F) and T-37.7°C (T-100°F) for steel IABs.

2.5.4 Load Combination

IABs in this study were also analyzed under Strength 1 and Service 1 load combinations according to the AASHTO design specification (AASHTO 2017). Due to the construction process described in Section 2.5.1, dead load was analyzed on a simply supported beam only, and the results were superimposed in spreadsheets. Thus, dead load was not included in the load combinations on 3-D analysis. Table 0.13 shows all possible Strength 1 and Service 1 load combinations that were considered in this study.

Table 0.13: Strength 1 and Service 1 Load Combinations

	Dead [D]	**Live (Truck + Lane) [L]**	**Positive Temperature [T(+)]**	**Negative Temperature [T(-)]**
Strength 1	1.25	1.75		
			1.2	
				1.2
		1.75	1.2	
		1.75		1.2
Service 1	1.0	1.0		
			1.2	
				1.2
		1.0	1.2	
		1.0		1.2

2.6 Verification of FEMs

Dicleli and Erhan (2009) reported results that corresponded to some of the analysis planned in this study, specifically concrete girder IABs with moving truck load applied. The results were therefore compared for similar bridges for verification of initial

FEMs for this study. Table 0.14 summarizes the result comparison for the maximum girder and pile bending moments. The differences were generally within approximately 10%. The larger values of percentage difference were recorded for pile bending moment, but the difference in actual values of pile bending moment was minimal. Considering that there were some slight variations in modeling assumptions and their models were used elastic soil properties throughout, the FEMs created for this study were considered to be verified and used for further parametric analysis.

Table 0.14: Comparison of Maximum Bending Moment in Girders at Mid-Span and Piles (kN-m)

Span length	Girder Size	Clay Stiffness	Girder Moment (kN-m)			Pile Moment (kN-m)		
			Dicleli & Erhan	FEM	% Difference	Dicleli & Erhan	FEM	% Difference
20m	II	Medium	533.1	525.5	1.42	22.27	21.73	2.42
20m	IV	Medium	674.6	679	0.65	11.04	10.47	5.16
30m	IV	Medium	1072.2	1030.1	3.92	N/A	N/A	N/A
40m	II	Medium	N/A	N/A	N/A	63.47	61.19	3.59
40m	IV	Medium	1377.8	1370.7	0.51	39.5	35.47	10.20
40m	VI	Medium	1567.2	1547.6	1.25	N/A	N/A	N/A

2.7 Automation of Modeling Processes

More than 500 FEMs were created and analyzed in this study. To optimize the modeling processes, some procedures were automated using CSi Application Programming Interface and MATLAB R2019b. The following lists include the automation processes used in this study.

- General commands, such as opening, saving, and running analysis,

- Applying thermal loads,
- Changing pile size and orientation,
- Applying concrete cracking on concrete sections,
- Recording the results of pile moment and substructure displacement results to Excel Spreadsheets.

CHAPTER 3

SIMPLY SUPPORTED BEAM ANALYSIS

This chapter presents the results of simply supported beam (SSB) analysis under dead and live loads. The purposes are to have a base-line to compare IAB superstructure moment results to, and to determine the amount of axial loads expected in the piles in order to define approximate non-linear hinge properties in the FEM pile response. Pin-roller supported 2-D beams for each span length were created in CSiBridge v21.2.0 by including the superstructure section of 3-D FEMs into a spine model as presented in Figure 0.1. This 2-D model was used to represent a simply supported bridge and verified against hand calculations.

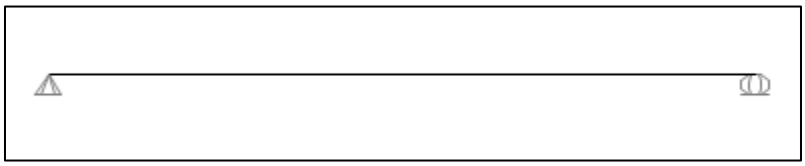

Figure 0.1: Typical Simply Supported 2-D Beam

3.1 Dead Load

Dead load considered in this study is only self-weight of superstructure (slab and girders), and any other dead load were ignored. Using the properties of slab and girders, reaction forces at the supports and maximum full bridge cross section moment were computed. The reaction force at each support was half of dead load, and the maximum moment for a simply supported beam under uniform dead load was computed. Assuming that the reaction force at each support were distributed equally to four piles, the axial load expected in each pile was computed as one-fourth of the reaction force at support. Table

0.1 and Table 0.2 show the results of axial load in each pile and maximum full bridge cross section moment for all superstructure properties used in this study. Additionally, these results were used to verify the 2-D model for the further analysis. Table 0.3 present the comparison of results of 2-D FEMs and hand calculation for typical concrete and steel girder bridges. As shown in the table, the results from 2-D FEMs almost matched exactly with hand calculation, thus, the models were verified.

Table 0.1: Axial Dead Load in Each Pile (kN)

		Span Length (m)		
		20	**30**	**40**
Concrete Girders	**AASHTO Type II**	169.2	253.8	338.4
	AASHTO Type IV	233.1	349.6	466.1
	AASHTO Type VI	278.0	417.1	556.1
Steel Girders	**S**	134.0	200.9	267.9
	M	140.9	211.3	281.8
	L	151.4	227.0	302.7

Note: The results are not factored.

Table 0.2: Maximum Full Bridge Cross Section Bending Moment at Mid-Span under Dead Load (kN-m)

		Span Length (m)		
		20	**30**	**40**
Concrete Girders	**AASHTO Type II**	3384	7614	13537
	AASHTO Type IV	4661	10488	18645
	AASHTO Type VI	5561	12512	22244
Steel Girders	**S**	2679	6028	10717
	M	2818	6340	11271
	L	3027	6811	12109

Note: The results are not factored.

Table 0.3: Comparison of FE and Hand Calculation Results

Span Length (m)	Girder Size	Axial Load (kN)		Maximum Moment (kN-m)	
		FEM	Hand Calculation	FEM	Hand Calculation
20	AASHTO Type II	169.2	169.2	3384.0	3384.1
30	AASHTO Type IV	349.6	349.6	10487.3	10487.8
40	AASHTO Type VI	556.1	556.1	22243.6	22243.6
20	S	134.0	134.0	2679.2	2679.3
30	M	211.4	211.3	6341.1	6340.1
40	L	302.7	302.7	12107.3	12108.7

3.2 Live Load Including HL-93 Truck and Lane Loads

Truck and lane loads were also analyzed separately on a 2-D simply supported beam. Two HL-93 truck components were placed, and two 3m-wide lane were placed, as previously shown in Figure 0.12. Moving load analysis for truck load and static linear analysis for lane load were performed on the 2-D simply supported beam with varying span length. Reaction forces at supports and maximum full bridge cross section bending moment at mid-span were recorded. Assuming that the reaction forces are equally distributed to each pile, axial load in each pile was determined. Table 0.4 and Table 0.5 present the axial load and maximum full bridge cross section moment, respectively for each span length. Since it was simply supported, the results were identical for FEMs with the same span length, regardless of girder types and sizes. These values are used for reference when plastic hinges and live load distributed factor (LLDF) of IABs are considered.

Table 0.4: Axial Load in Each Pile under Two Loaded Lanes [kN (kip)]

Load Type	Span Length		
	20m	30m	40m
Lane Load	46.7 (10.5)	70.0 (15.7)	93.4 (21.0)
Truck Load	137.4 (30.9)	145.0 (32.6)	148.8 (33.5)

Table 0.5: Maximum Full Bridge Cross Section Moment under Two Loaded Lanes [kN-m (kip-ft)]

Load Type	**Span Length**		
	20m	**30m**	**40m**
Lane Load	934 (688)	2101 (1548)	3735 (2752)
Truck Load	2458 (1811)	4055 (2988)	5653 (4165)

3.3 Expected Axial Loads in Piles

Using the expected axial loads determined in the previous sections, the axial load under the critical Strength 1 load combination expected in each pile was determined for defining non-linear plastic hinge properties described in Section 2.3. Piles are expected to have axial loads from dead and live loads only, and thus, the critical load Strength 1 load combination is 1.25D+1.75L. The axial loads were factored and compared with axial pile capacities (P_y) of HP250x85 and HP310x125. Table 0.6 presents the results of factored axial loads expected in each pile for IABs with ideal girders for that span length and the relative ratio to P_y of two HP sections. The results showed that the piles are subjected to axial loads up to 30% of pile axial capacities for ideal girder IABs for that span.

Table 0.6: Expected Critical Axial Load in Piles

Span Length (m)	**Girder Size**	**Factored Axial Load, P [kN (kip)]**	**P/P_y HP250x85**	**P/P_y HP310x125**
20	AASHTO Type II	534 (120)	0.14	0.10
30	AASHTO Type IV	813 (183)	0.22	0.15
40	AASHTO Type VI	1119 (252)	0.30	0.20
20	S	490 (110)	0.13	0.09
30	M	640 (144)	0.17	0.12
40	L	802 (180)	0.22	0.15

Note: P_y (HP250x85) = 3723kN (837kip) and P_y (HP310x125) = 5481kN (1232kip)

CHAPTER 4

PARAMETRIC STUDY ON SINGLE SPAN STRAIGHT INTEGRAL ABUTMENT BRIDGES UNDER HL-93 TRUCK COMPONENT LOADING

This chapter presents the results of a parametric study investigating the effect of truck load and foundation soil conditions for single-span IABs of varying span length and girder types and sizes. This parametric study is limited to HL-93 truck component loading of symmetrical single-span slab on girder IABs with HP250x85 and without skew or curvatures, thus, all parameters in Table 0.2, except pile size. The objective was to analyze the effects of the soil and structural parameters on bridge responses, such as girder, pile bending moments and pile deformation under truck load. These models were used to validate the modeling against previous research for the single load condition of truck load, to verify trends in data expected in the full models of Chapter 6, and to evaluate resulting LLDFs under conditions considered by AASHTO Design Specification (AASHTO 2017).

4.1 Full Bridge Cross Section Bending Moment

This section presents the results of full bridge cross section bending moment. The values of bending moment about the center of gravity of superstructure were recorded for IABs as full bridge cross section bending moment. To determine the effect of fixity of superstructure and substructure in IABs, the results of the full 3-D analysis were compared with the truck load results of SSBs (pin-roller supported bridges) presented in Section 3.2. Figure 0.1 shows typical moment diagrams determined under the truck load

for IAB and SSB for 20m IABs; the results are presented as an envelope of moment for all possible truck positions.

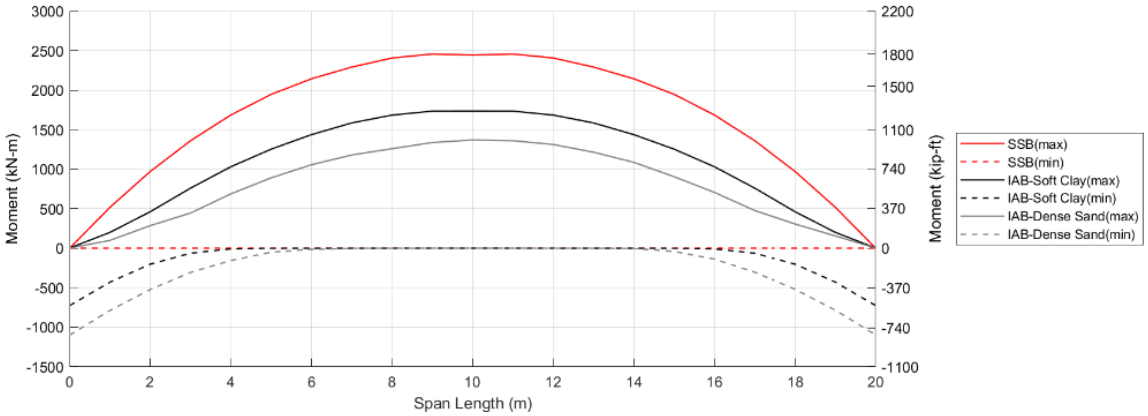

Figure 0.1: Typical Full Bridge Moment Diagram
IAB parameters presented here are Span Length = 20m, Girder Type: AASHTO Type II, and Pile Orientation = Weak Axis

As shown in Figure 0.1, the overall shape of diagram remains unchanged between SSB and IAB results; maximum moment at the mid span and minimum moment at the end-span. In SSBs, moment is released at end supports, and is therefore zero. However, fixity at the end of bridge due to the continuity of the superstructure and abutments in IABs shifts the moment diagrams, resulting in negative bending moment at the end supports. This shift also resulted in IABs having smaller maximum full bridge cross section bending moment at mid-span, compared to SSBs.

Since the shape of diagram remains unchanged between IABs and SSBs, the value of end-span bending moment (M_{end}) determines the amount of shift in moment diagrams in IABs and is related to the restraining substructure stiffness of IABs when a single load case is considered. Moreover, the addition of the maximum moment at mid-span (M_{max}) and moment at the end-span (M_{end}) of IAB should equal to the maximum mid-span bending moment of the simply supported bridge (M_{ss}). As presented in Figure 0.1, when stiffer soil was present around piles (stiffer substructure), M_{end} was larger; the

shift in moment diagrams was larger. Table 0.1 also shows that the values of (M_{max}+M_{end}) were almost identical to the values of M_{ss} for this single load case.

Table 0.1: Comparison of Superstructure Moment and Axial Loads, and Pile Moment

Span Length	Girder Size	Soil Stiffness	M_{max} (kN-m)	M_{end} (kN-m)	$M_{max}+M_{end}$ (kN-m)	M_{ss} (kN-m)	P (kN)	$M_{\Sigma Pile}$ (kN-m)
20m	Type II	Soft Clay	1735	726	2461	2458	308	54
	Type II	Dense Sand	1370	1099	2469	2458	376	129
	S	Soft Clay	1542	929	2471	2458	384	68
	S	Dense Sand	1244	1237	2480	2458	413	144
30m	Type IV	Soft Clay	3465	591	4055	4055	273	52
	Type IV	Dense Sand	2858	1201	4059	4055	444	155
	M	Soft Clay	2981	1080	4061	4055	465	84
	M	Dense Sand	2351	1720	4071	4055	596	207
40m	Type VI	Soft Clay	5164	490	5654	5653	240	49
	Type VI	Dense Sand	4478	1175	5653	5653	458	164
	L	Soft Clay	4451	1208	5659	5653	540	101
	L	Dense Sand	3529	2144	5673	5653	767	270
$M_{max} + M_{end} \approx M_{ss}$ $M_{end} \gg M_{\Sigma Pile}$								

Table 0.1 also shows the sum of the maximum moment developing in the four piles ($M_{\Sigma Pile}$). Under the truck load, maximum moment in piles were observed at the top of the piles. Bending moment at the ends of the bridge span is transferred to substructures and distributed within the substructure and soil. The results showed that bending moment at the top of the piles was only about 5-15% of the bending moment observed at the end of span. This indicates that the soil plays a significant role in the fixity at the end of the span. Evaluation of this effect shows that the axial load (P) developed in the superstructure acts as a force couple with the pile shear and lateral soil forces to counter

the superstructure end span bending moment. Distributions of lateral soil pressures (location and magnitude) depend on soil type, making it difficult to predict.

Figure 0.2 shows the results of maximum full bridge cross section moment observed for all bridges with HP250x85 oriented about the weak axis. IABs resulted in a smaller value of maximum full bridge bending moment than SSBs regardless of bridge geometry. This indicates that the fixity of superstructure and substructure in IABs reduces the mid-span moment and increases the negative moment at the end, as was presented in Figure 0.1. The results also showed that the maximum mid-span full bridge moment decreased as soil stiffens; the stiffer substructure reduces more moment at the mid-span. The results for stiff clay and loose sand overlapped in most plots, which was expected due to their soil properties being similar in the elastic region of response. Furthermore, the results showed that bridges with larger girder sizes have higher values of maximum full bridge cross section moment due to the higher relative stiffness of the superstructure to substructure. The higher moment was observed for the superstructure with higher moment of inertia, in the order of small steel, AASHTO Type II, medium steel, large steel, AASHTO Type IV, and AASHTO Type VI girders with the moment of inertia of 2.3, 3.8, 6.3, 10.7, 13.1, and 27.4 (e11 mm^4), respectively, as listed in Table 0.6.

The effect of pile orientation was also analyzed. The results are limited for concrete IABs, but steel IABs with strong-axis pile orientation are investigated in Chapter 6. Figure 0.3 shows the results of maximum full bridge cross section moment of concrete IABs with varying pile orientation. The results showed that the pile orientation did not have a significant effect on the full bridge cross section moment. The difference in the results between strong and weak axis bending was all within 5%. These results

indicate that moment restraints at the end-span are dominated by soil properties rather than pile properties.

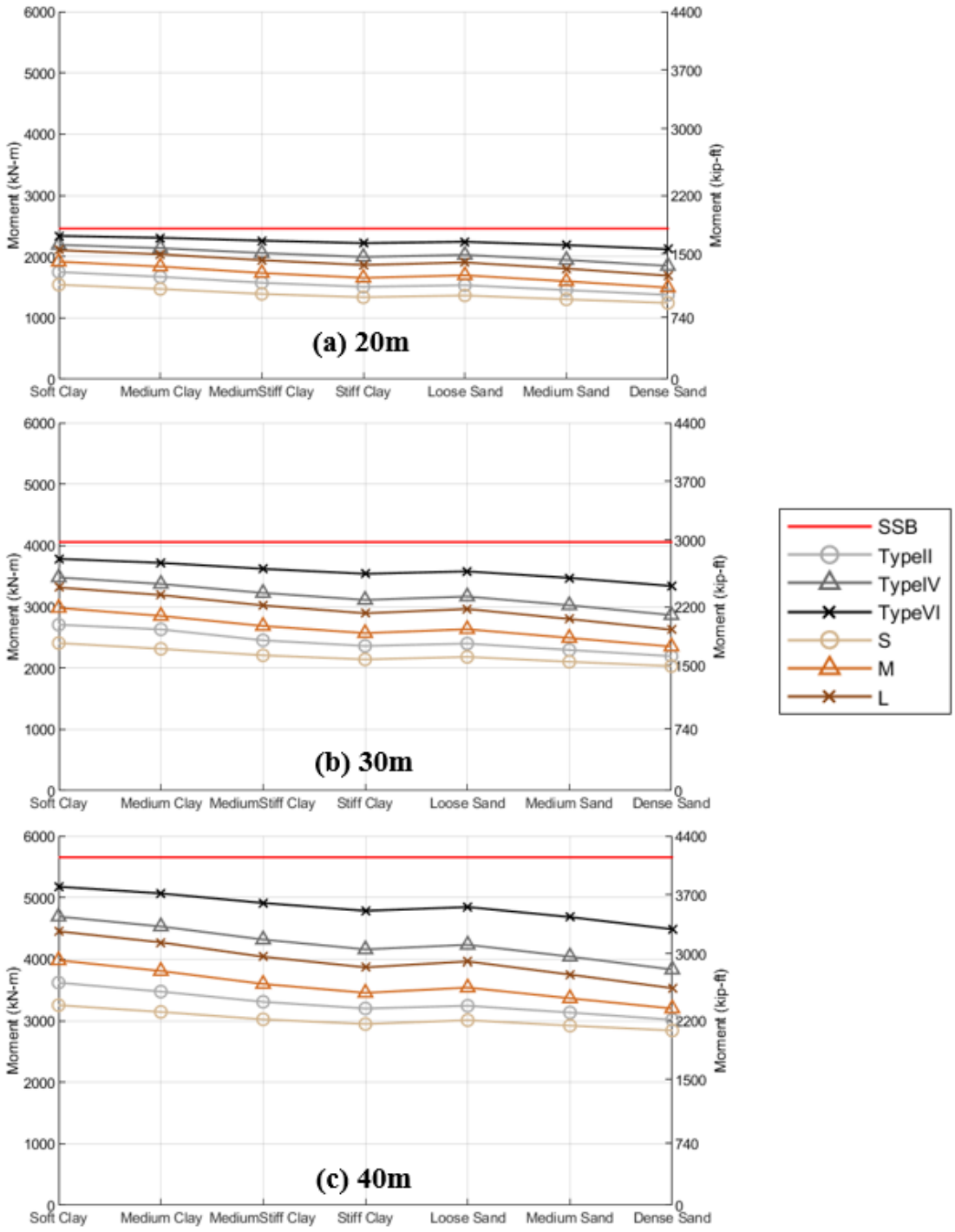

Figure 0.2: Maximum Full Bridge Cross Section Moment of SSBs and IABs with Varying Girder Size and Soil Condition for (a)20m, (b)30m, and (c)40m Span Length
Note: Pile = HP250x85 and Weak Axis Bending

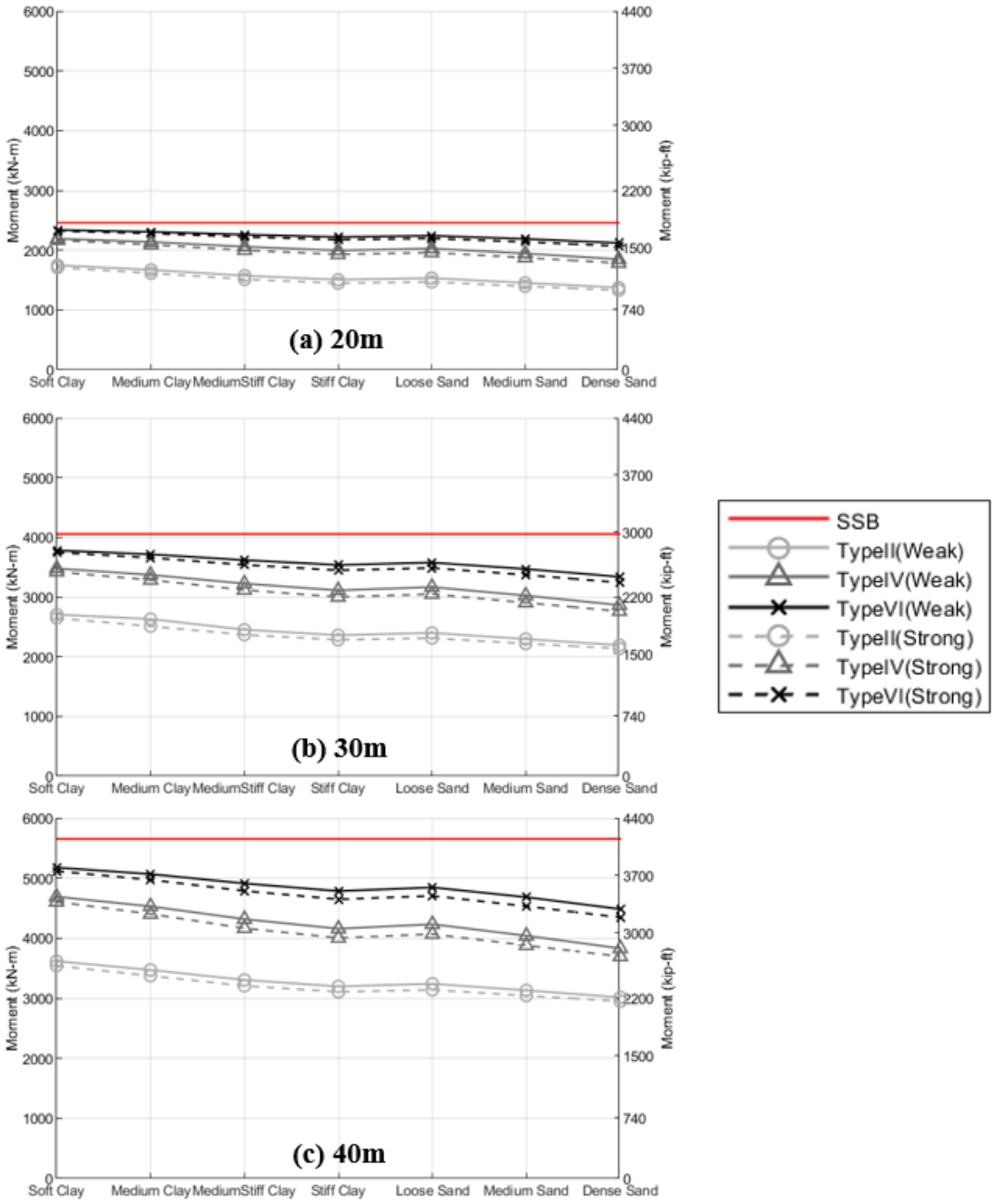

Figure 0.3: Maximum Full Bridge Moment of SSBs and IABs with Varying Concrete Girder Size, Soil Condition, and Pile Orientation for (a)20m, (b)30m, and (c)40m Span Length

Note: Pile = HP250x85

4.2 Bending Moment in Girders

This section describes the effect of superstructure and substructure on individual girder bending moment in IABs. The values of moment about the center of gravity of the composite girder were recorded for each girder. This avoids the change in moment due to eccentricity of any axial load that develops in the girders. The location of critical girder within the bridges under truck load was compared. Since the trucks were placed towards the left side of deck to produce the most critical bridge response, a girder that had the largest value of moment among four girders was either a left exterior girder or left interior girder. The results showed the left exterior girder was most critical in most bridges, but left interior girder was the critical girder in most 20m IABs and some 30m steel girder IABs. Table 0.2 presents the difference between exterior and interior girder moments in percentage for all IABs with piles oriented about the weak axis. The negative values highlighted in the table indicate that the maximum moment in interior girder was greater. The difference in values between the left exterior and interior girder moments was up to 11%. Larger difference in values was observed for IABs with unrealistic girders, such as shorter span IABs with larger girders and longer span IABs with smaller girders. Overall, the difference was smaller for shorter span IABs. Although Table 0.2 is limited to the results of IABs with piles oriented about the weak axis, the results of critical girder location and difference between the left exterior and interior girders were almost identical for IABs with piles oriented about the strong axis.

Table 0.2: Difference Between Exterior and Interior Girder Moment in Percentage

		Precast Concrete Girder Size			Steel Girder Size		
Span Length = 20m		**Type II**	**Type IV**	**Type VI**	**Small**	**Medium**	**Large**
Soil Type	Soft Clay	-1.7	-4.1	-5.9	0.8	-3.5	-4.3
	Medium Clay	-1.8	-4.2	-6.0	0.7	-3.7	-4.4
	Medium Stiff Clay	-2.1	-4.3	-6.1	0.6	-3.9	-4.7
	Stiff Clay	-2.2	-4.4	-6.2	0.6	-4.2	-4.9
	Loose Sand	-0.9	-1.9	-2.6	-3.9	-9.1	-9.8
	Medium Sand	-1.0	-2.0	-2.7	-4.2	-9.6	-10.3
	Dense sand	-1.2	-2.1	-2.8	-4.4	-10.3	-11.0
Span Length = 30m		**Type II**	**Type IV**	**Type VI**	**Small**	**Medium**	**Large**
Soil Type	Soft Clay	4.8	1.7	0.5	9.1	4.6	2.6
	Medium Clay	5.0	1.7	0.5	9.3	4.7	2.7
	Medium Stiff Clay	5.1	1.8	0.5	9.6	4.8	2.7
	Stiff Clay	5.2	1.8	0.5	9.8	4.9	2.7
	Loose Sand	5.9	2.9	2.1	7.1	1.6	-0.8
	Medium Sand	6.2	3.0	2.1	7.3	1.6	-0.9
	Dense sand	6.4	3.1	2.2	7.4	1.5	-1.1
Span Length = 40m		**Type II**	**Type IV**	**Type VI**	**Small**	**Medium**	**Large**
Soil Type	Soft Clay	7.0	4.0	3.3	12.0	9.2	7.4
	Medium Clay	7.2	4.1	3.3	12.3	9.5	7.6
	Medium Stiff Clay	7.5	4.3	3.4	12.7	9.9	7.9
	Stiff Clay	7.7	4.4	3.5	12.9	10.1	8.1
	Loose Sand	8.3	5.4	4.6	11.0	7.8	5.5
	Medium Sand	8.6	5.6	4.8	11.2	8.0	5.7
	Dense sand	8.8	5.8	4.9	11.4	8.2	5.9

Note: Negative values in highlighted cells indicate that a greater maximum girder moment was recorded in interior girders.

Figure 0.4 shows the results of maximum girder moment for IABs with piles oriented about the weak axis in this parametric study. The comparison was made even though the location of the critical girder may differ. The trend of the plots for girder moment was similar to the trend observed for full bridge cross section moment: the maximum moment decreased as the soil stiffness increases regardless of bridge geometries. Even though IABs with AASHTO Type II and small steel girders, and IABs with AASHTO Type IV and large steel girders produced almost identical results, it was

still related to the relative stiffness of superstructure: the higher girder moment was observed for IABs with a higher moment of inertia.

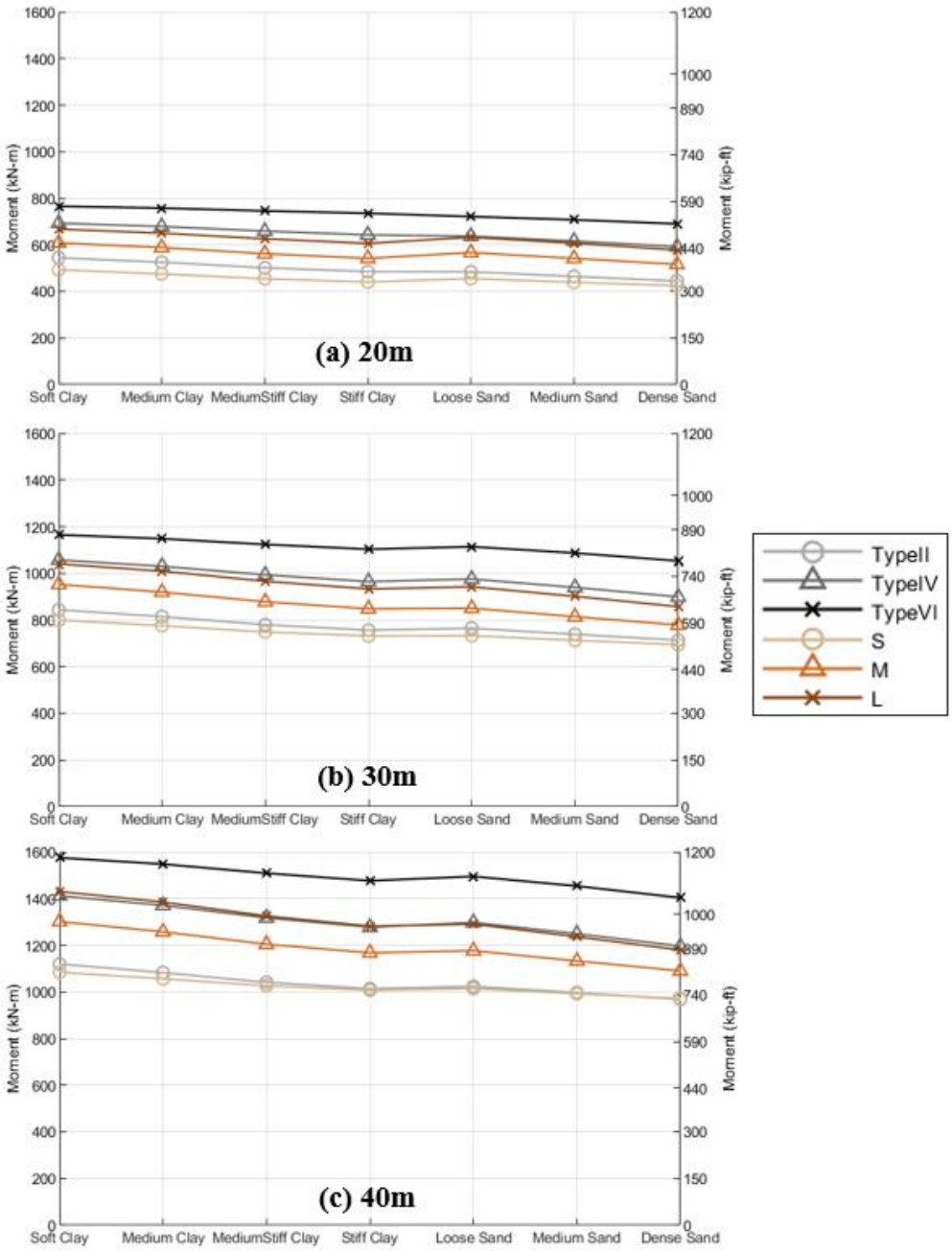

Figure 0.4: Maximum Mid-Span Girder Moment of IABs with Varying Girder Type and Size for (a)20m, (b)30m, and (c)40m Span Length
Note: Pile = HP250x85 and Weak Axis Bending

4.3 Evaluation of LLDFs of IABs

In this section, the LLDFs for girder moment of IABs were estimated based on the FE analysis results from this study and compared with the design LLDFs recommended for SSBs by AAHSTO Bridge Design Specification (AASHTO 2017) and LLDF equations for concrete IABs developed by Dicleli and Erhan (2009). According to the AASHTO Bridge Design Specification, the LLDFs must be calculated for one loaded lane and two or more loaded lanes, and a greater value should be used. The AASHTO LLDFs for exterior and interior girder moments were determined, using the following equations:

for one design loaded lane,

$$AASHTO\ LLDF_{interior} = 0.06 + \left(\frac{S}{14}\right)^{0.4}\left(\frac{S}{L}\right)^{0.3}\left(\frac{K_g}{12.0Lt_s{}^3}\right)^{0.1} \quad \text{Equation 0-1}$$

$$AASHTO\ LLDF_{exterior} = lever\ rule \quad \text{Equation 0-2}$$

for two or more design loaded lanes,

$$AASHTO\ LLDF_{interior} = 0.075 + \left(\frac{S}{9.5}\right)^{0.6}\left(\frac{S}{L}\right)^{0.2}\left(\frac{K_g}{12.0Lt_s{}^3}\right)^{0.1} \quad \text{Equation 0-3}$$

where

$$K_g = n(I + Ae_g{}^2) \quad \text{Equation 0-4}$$

$$AASHTO\ LLDF_{exterior} = (0.77 + \frac{d_e}{9.1}) \cdot LLDF_{interior} \quad \text{Equation 0-5}$$

where S = spacing of girders(ft), L = span length(ft), n = modular ratio between girder and slab, I = moment of inertia of girder(in^4), A = cross sectional area of girder(in^2), e_g = distance between the centers of gravity of the girder and slab(in), t_s = thickness of slab(in), and d_e = distance from the centerline of the exterior girder to the interior edge of

traffic barrier(ft). The lever rule for the exterior girder defined in the AASHTO was used with the multiple presence factor of 1.2, and it was determined to be 0.75 lanes; this controlled in most IABs except 20m span bridges with AASHTO Type VI. Table 0.3 and Table 0.4 present summary of the AASHTO LLDFs for interior and exterior girder moments computed for IABs analyzed in this study. These values are used for a reference when LLDFs of IABs are determined.

Table 0.3: AASHTO LLDFs for Interior Girder Moments with Varying Span Length and Girder Size

		Span Length		
		20m	**30m**	**40m**
Girder Size	**Type II**	0.65	0.58	0.54
	Type IV	0.74	0.66	0.61
	Type VI	0.83	0.74	0.69
	S	0.62	0.55	0.52
	M	0.68	0.61	0.56
	L	0.72	0.64	0.60

Table 0.4: AASHTO LLDFs for Exterior Girder Moments with Varying Span Length and Girder Size

		Span Length		
		20m	**30m**	**40m**
Girder Size	**Type II**	0.75	0.75	0.75
	Type IV	0.75	0.75	0.75
	Type VI	0.82	0.75	0.75
	S	0.75	0.75	0.75
	M	0.75	0.75	0.75
	L	0.75	0.75	0.75

Dicleli and Erhan (2009) developed equations to estimate LLDFs for concrete IABs based on the 3-D analysis and 2-D rigid frame analysis of IABs. The equations were developed for both one design loaded lane and two or more design loaded lanes independent of AASHTO LLDF equations. Similarly, LLDFs for both cases must be determined, and a greater value should be used. For all IABs of this study, the LLDFs for two or more design loaded lanes controlled. The proposed equations for two or more loaded lanes are following:

$$IAB\ LLDF_{interior} = \frac{S^{0.82}}{500L^{0.06}} \qquad \text{Equation 0-6}$$

$$IAB\ LLDF_{exterior} = \frac{L^{0.09}S^{0.53}{t_s}^{0.06}}{80{K_g}^{0.04}}\ (0.5 + \frac{d_e}{5000}) \qquad \text{Equation 0-7}$$

where

$$K_g = n(I + A{e_g}^2) \qquad \text{Equation 0-8}$$

These equations are developed in SI units. The unit for each parameters is as follows; S = spacing of girders(mm), L = span length(mm), n = modular ratio between girder and slab, I = moment of inertia of girder(mm^4), A = cross sectional area of girder(mm^2), e_g = distance between the centers of gravity of the girder and slab(mm), t_s = thickness of slab(mm), and d_e = distance from the centerline of the exterior girder to the interior edge of traffic barrier(mm). Table 0.5 and Table 0.6 present the calculated LLDFs for interior and exterior girder moments for IABs using the equations developed by Dicleli and Erhan (2009). As shown in Equation 0-6 and Table 0.5, LLDFs for interior girder moments using the Dicleli and Erhan's equation do not depend on girder sizes, thus they are consistent regardless of girder sizes for the same span length.

Table 0.5: LLDFs for Interior Girder Moments Estimated using Dicleli and Erhan's Equations (2009) for IABs with Varying Span Length and Girder Size

		Span Length		
		20m	**30m**	**40m**
Girder Size	**Type II**	0.65	0.64	0.63
	Type IV	0.65	0.64	0.63
	Type VI	0.65	0.64	0.63
	S	0.65	0.64	0.63
	M	0.65	0.64	0.63
	L	0.65	0.64	0.63

Table 0.6: LLDFs for Exterior Girder Moments Estimated using Dicleli and Erhan's Equations (2009) for IABs with Varying Span Length and Girder Size

		Span Length		
		20m	**30m**	**40m**
Girder Size	**Type II**	0.58	0.60	0.62
	Type IV	0.54	0.56	0.58
	Type VI	0.52	0.54	0.55
	S	0.59	0.61	0.63
	M	0.57	0.59	0.60
	L	0.55	0.57	0.59

Two methods were performed to estimate the LLDF of IABs from the FE analysis of this study. The first method was to estimate the LLDFs as the ratio of the maximum mid-span girder moment from 3-D analysis to the maximum mid-span full bridge cross section moment from the 2-D pin-roller analysis results of a single truck load (half of the truck load results presented in Table 0.5). This method is similar to the way used in developing the equation of LLDFs for SSBs by AASHTO, and this allows a comparison of the girder moment of IABs with the results of simple 2-D beam analysis. The second method was to estimate the LLDFs as the ratio of the maximum mid-span girder moment from 3-D analysis to the maximum full bridge cross section moment of a single truck load from the 3-D analysis (half of the results presented in Figure 0.2). The full bridge cross section moment recorded from the 3-D analysis was assumed to be identical to the

results of a 2-D rigid frame analysis since the full bridge cross section moment is taken about the center of gravity in superstructure in both analyses. The full bridge cross section moment from the rigid frame analysis is more practical in the case of IABs since the effects of substructure stiffness and rigidity of superstructure and abutments present in IABs are accounted.

Table 0.7 and Table 0.8 present the LLDFs for interior and exterior girder moments computed using the two assumptions described above, respectively. The results are limited to IABs with HP250x85 oriented about the weak axis; pile orientation has minimal impacts on superstructure moments as proved in Figure 0.3. The LLDFs computed for IABs include the effect of substructure stiffness, thus the results in the Table 0.7 and Table 0.8 were in a range of numbers for a particular IAB with varying foundation soil stiffness. The results showed that the LLDFs estimated from the 2-D simply supported analysis decreased as the foundation soil stiffened and increased as the girder sizes increased. On the other hand, the LLDFs estimated from the rigid frame analysis increased as the foundation soil stiffened and remained relatively consistent with the change in the girder size. The variation in LLDFs with the change in soil stiffness was also relatively smaller (within 10% difference) for the LLDFs computed from the rigid frame. This indicates that the effects of soil stiffness and superstructure stiffness are not significant in determining LLDFs when rigid frame analysis was used. This also agrees with the proposed LLDF equation for interior girder moment by Dicleli and Erhan (2009) for being independent of the effect of substructure and superstructure stiffness. The proposed equation for the exterior girder moment is also independent of the substructure stiffness.

Table 0.7: The Range of LLDFs for Interior Girder Moment Computed for IABs with Varying Span Length and Girder Size

	FEM (Pin-Roller)			FEM (Rigid Frame)		
	20m	**30m**	**40m**	**20m**	**30m**	**40m**
Type II	0.36 - 0.44	0.33 - 0.40	0.31 - 0.37	0.62 - 0.65	0.59 - 0.61	0.58 - 0.59
Type IV	0.48 - 0.56	0.43 - 0.51	0.40 - 0.48	0.63 - 0.64	0.60 - 0.61	0.58 - 0.59
Type VI	0.56 - 0.62	0.51 - 0.57	0.47 - 0.54	0.64 - 0.66	0.61 - 0.62	0.59 - 0.60
S	0.35 - 0.40	0.32 - 0.36	0.31 - 0.34	0.63 - 0.68	0.61 - 0.63	0.59 - 0.61
M	0.42 - 0.50	0.38 - 0.45	0.36 - 0.42	0.63 - 0.69	0.61 - 0.65	0.60 - 0.63
L	0.47 - 0.54	0.42 - 0.50	0.39 - 0.47	0.63 - 0.68	0.61 - 0.65	0.60 - 0.63

Note: Minimum value corresponds to the result of dense sand, and maximum value corresponds to the result of soft clay.
IAB Parameter: Pile = HP250x85 and Weak Axis Bending

Table 0.8: The Range of LLDFs for Exterior Girder Moment Computed for IABs with Varying Span Length and Girder Size

	FEM (Pin-Roller)			FEM (Rigid Frame)		
	20m	**30m**	**40m**	**20m**	**30m**	**40m**
Type II	0.36 - 0.44	0.35 - 0.42	0.34 - 0.40	0.61 - 0.64	0.62 - 0.65	0.62 - 0.64
Type IV	0.47 - 0.54	0.44 - 0.52	0.42 - 0.50	0.61 - 0.63	0.61 - 0.63	0.60 - 0.62
Type VI	0.55 - 0.59	0.52 - 0.57	0.50 - 0.56	0.62 - 0.63	0.62 - 0.63	0.61 - 0.63
S	0.33 - 0.40	0.34 - 0.39	0.34 - 0.38	0.64 - 0.66	0.66 - 0.68	0.67 - 0.68
M	0.38 - 0.48	0.38 - 0.47	0.39 - 0.46	0.61 - 0.63	0.64 - 0.66	0.65 - 0.68
L	0.42 - 0.52	0.42 - 0.51	0.42 - 0.51	0.60 - 0.62	0.63 - 0.65	0.64 - 0.67

Note: Minimum value corresponds to the result of soft clay, and maximum value corresponds to the result of dense sand.
IAB Parameter: Pile = HP250x85 and Weak Axis Bending

Figure 0.5 and Figure 0.6 show comparison of the LLDFs of all IABs for interior and exterior girder moments estimated by two methods from FEMs of this study, and the LLDFs computed using AASHTO LLDF equations (AASHTO 2017) and Dicleli's developed equations for concrete IABs (Dicleli and Erhan 2009). Since both AASHTO LLDF and developed LLDF equations do not consider the effect of soil stiffness, only one value of LLDF is determined for each bridge, regardless of substructure properties, as was presented in Table 0.3-Table 0.6. However, the LLDFs of IABs estimated from

the FEMs of this study slightly varied based on foundation soil, thus, the average value was calculated to make a comparison. Dicleli and Erhan (2009) developed the equations for concrete IABs, but applicability of these equations for steel IABs was determined in this study.

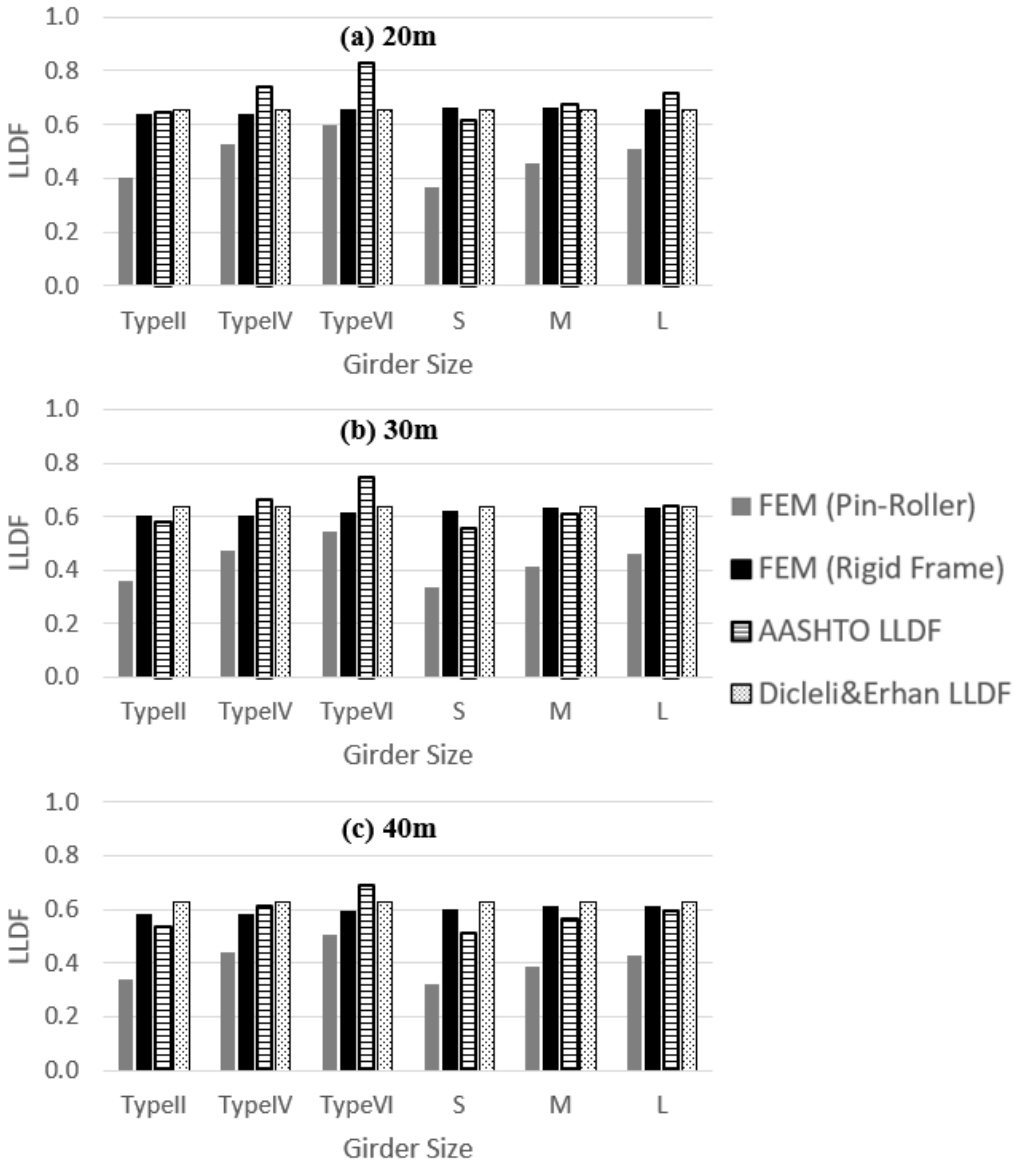

Figure 0.5: Comparison of LLDFs for Interior Girder Moments Estimated for (a)20m, (b)30m, and (c)40m IABs with Varying Girder Size

Note: Average value from seven soil types was calculated for FEM (Pin-Roller) and FEM (Rigid Frame)
IAB parameters: Pile = HP250x85 and Weak Axis Bending

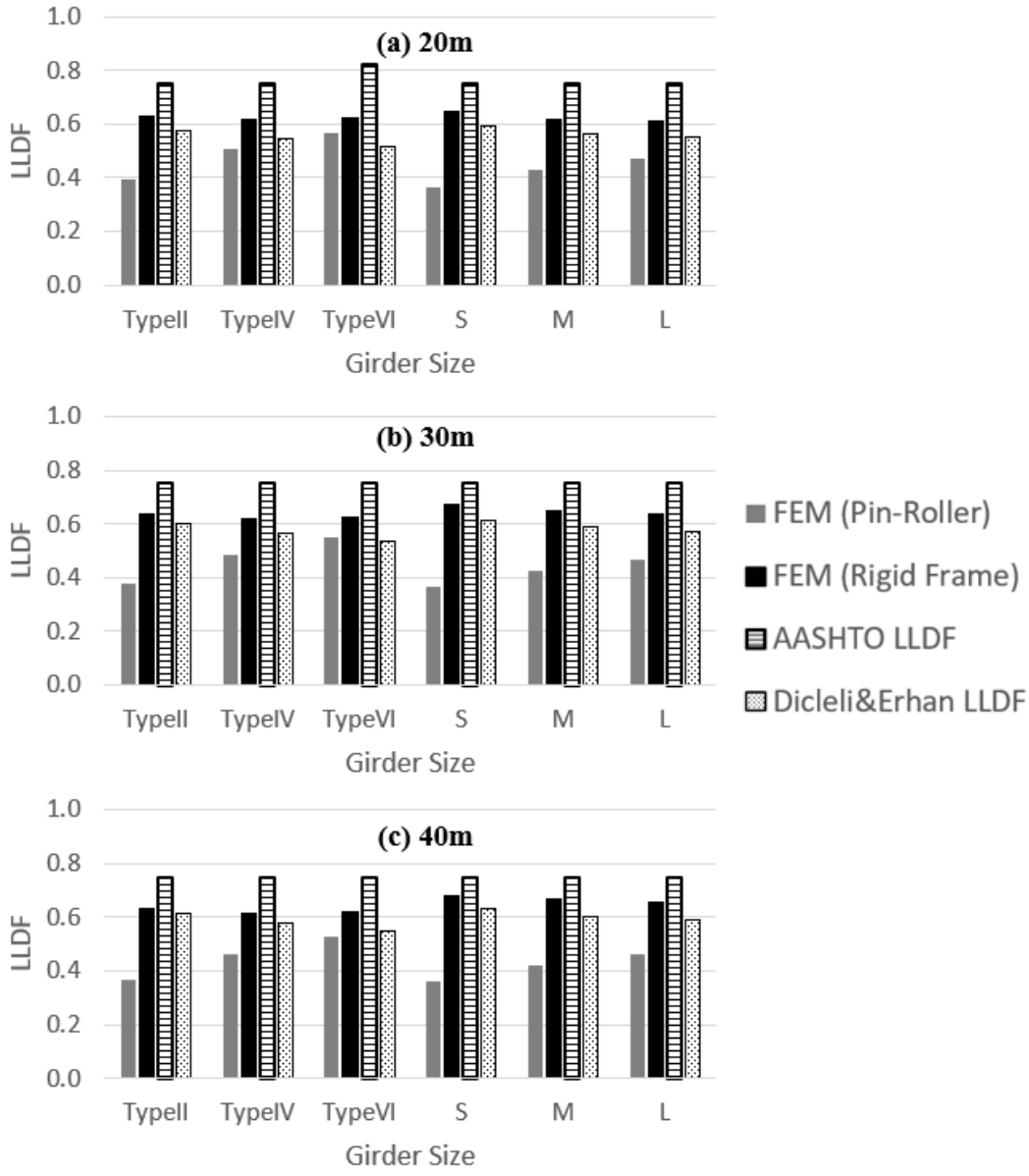

Figure 0.6: Comparison of LLDFs for Exterior Girder Moments Estimated for (a)20m, (b)30m, and (c)40m IABs with Varying Girder Size

Note: Average value from seven soil types was calculated for FEM (Pin-Roller) and FEM (Rigid Frame)
IAB parameters: Pile = HP250x85 and Weak Axis Bending

The results showed that AASHTO LLDFs for interior girder moment were about 20-40% greater than the LLDFs estimated from the simply supported beam analysis of IABs. For exterior girder moment, the AASHTO predicted that one loaded lane was more critical, and they were 30%-50% greater than the LLDFs estimated from the simply supported beam analysis of IABs. The AASHTO LLDFs are developed for SSBs, thus the reduction in superstructure moments due to the fixity of superstructure and substructure in IABs is not accounted. Additionally, for SSBs, one loaded lane may be more critical for exterior girder, however, two loaded lanes always controlled in the case of IABs, as the fixity of superstructure and substructure in IABs improve the load distribution. This indicates that the AASHTO LLDFs are conservative to use for any IABs if girder moments are estimated based on 2-D simply supported beam analysis.

When compared to LLDFs estimated from the results of the rigid frame, the AASHTO LLDFs were up to about 25% greater for exterior girder moment. For interior girder moment, AASHTO LLDFs produced reasonable estimates (within ±10% difference) for IABs with ideal girder sizes for that span length. However, the difference increased for IABs with unrealistic girder sizes; AASHTO LLDFs were up to 17% smaller for 40m IABs with the smallest concrete and steel girders, but they were up to 23% greater for 20m span IABs with the largest concrete and steel girders. This indicates that even if the 2-D rigid frame analysis was performed to consider the substructure stiffness, the AASHTO LLDFs may overestimate or underestimate girder moments of IABs depending on the superstructure stiffness.

The results of rigid frame were also compared with the LLDFs determined using the Dicleli and Erhan's equations (2009) that were developed for concrete IABs based on

the 2-D rigid frame analysis. The results showed that LLDFs computed using the proposed equations generally agreed with the LLDFs for interior girder moment (only up to 7% difference), however, they were up to 20% smaller for the exterior girder moments. Even though these equations were developed for concrete IABs, the results were relatively similar for steel IABs.

4.4 Substructure Displacement

This section presents the effects of each study parameter on the substructure displacement under a single load case, truck load. The displacement of the substructure was most critical at location of left exterior pile under the truck load indicated by the dashed line in Figure 0.7 for all FEMs. Minimum and maximum substructure displacements were recorded as the envelope of all possible truck positions. The following sections describe the effect of each parameter.

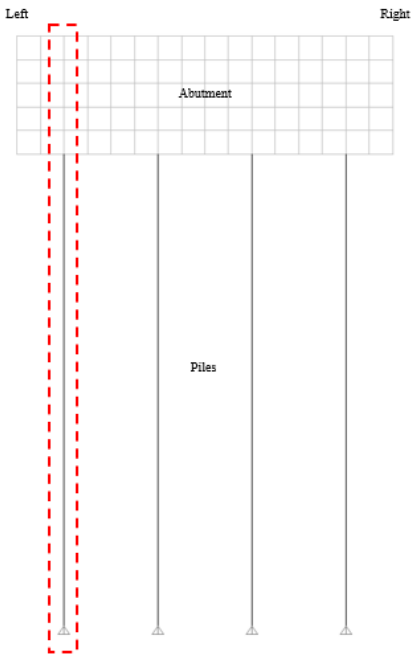

Figure 0.7: Location of Most Critical Substructure Displacement

4.4.1 Effect of Soil Stiffness

The effect of soil stiffness on substructures displacement of IABs was analyzed by plotting the results for the same bridge with varying soil properties. As an example, the results for bridges with 40m span length and AASHTO Type VI are presented in Figure 0.8. The negative displacement indicates the movement of the substructure away from the center of the bridge, and the positive displacement indicates the movement of the substructure towards the center of the bridge. The results showed that as soil stiffens, the overall displacement and rotation of substructures decreased, and this was true for all IABs with varying girders and span length. When soil was softer, the curve was smoother, and the pile displaced at deeper depth.

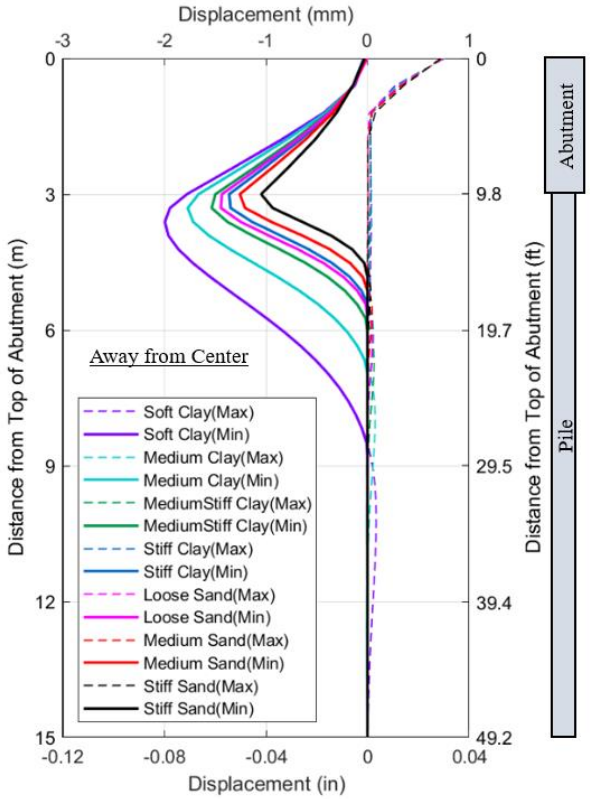

Figure 0.8: Substructure Displacement of IABs with Varying Soil Stiffness
IAB Parameters: Span Length = 40m, Girder = AASHTO Type VI, Pile = HP250x85 and Weak Axis Bending

4.4.2 Effect of Span Length

The effect of span length was analyzed by plotting the results of IABs with varying span length. As an example, IABs with AASHTO Type II built on soft clay (loosest soil) and dense sand (stiffest soil) are presented in Figure 0.9. The results showed that substructure displaced more, and abutment had significantly greater rotation when the span length was longer. The same observation was made for IABs with other girder sizes and varying span length. This corresponds to the cases with larger end moments in the span.

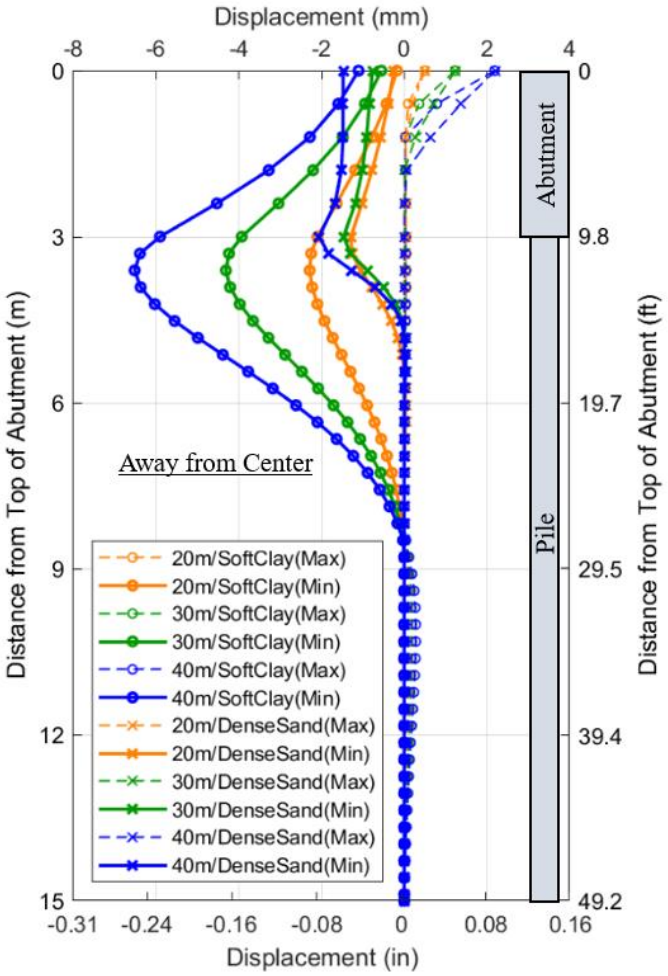

Figure 0.9: Substructure Displacement of IABs with Varying Span Length
Note: IAB parameters: Girder = AASHTO Type II, Pile = HP250x85 and Weak Axis Bending

4.4.3 Effect of Girder Size

Similarly, the effect of girder size on substructure displacement was evaluated. For a comparison, 40m span length IABs with varying girder sizes built on the loosest and stiffest soil is presented in Figure 0.10. The superstructure with smaller girders allowed the abutment to rotate more freely, thus a greater displacement and rotation of abutment were observed. As shown in Figure 0.10(a), AASHTO type II is the smallest concrete girder size, and thus, the displacement was the largest. On the other hand, AASHTO type VI was the largest concrete girder size, and the displacement was the smallest. This relationship was also observed in the substructure of steel girder IABs. As was also shown in Section 4.4.1, a similar effect (smaller substructure displacement and abutment rotation) was observed as the soil became stiffer.

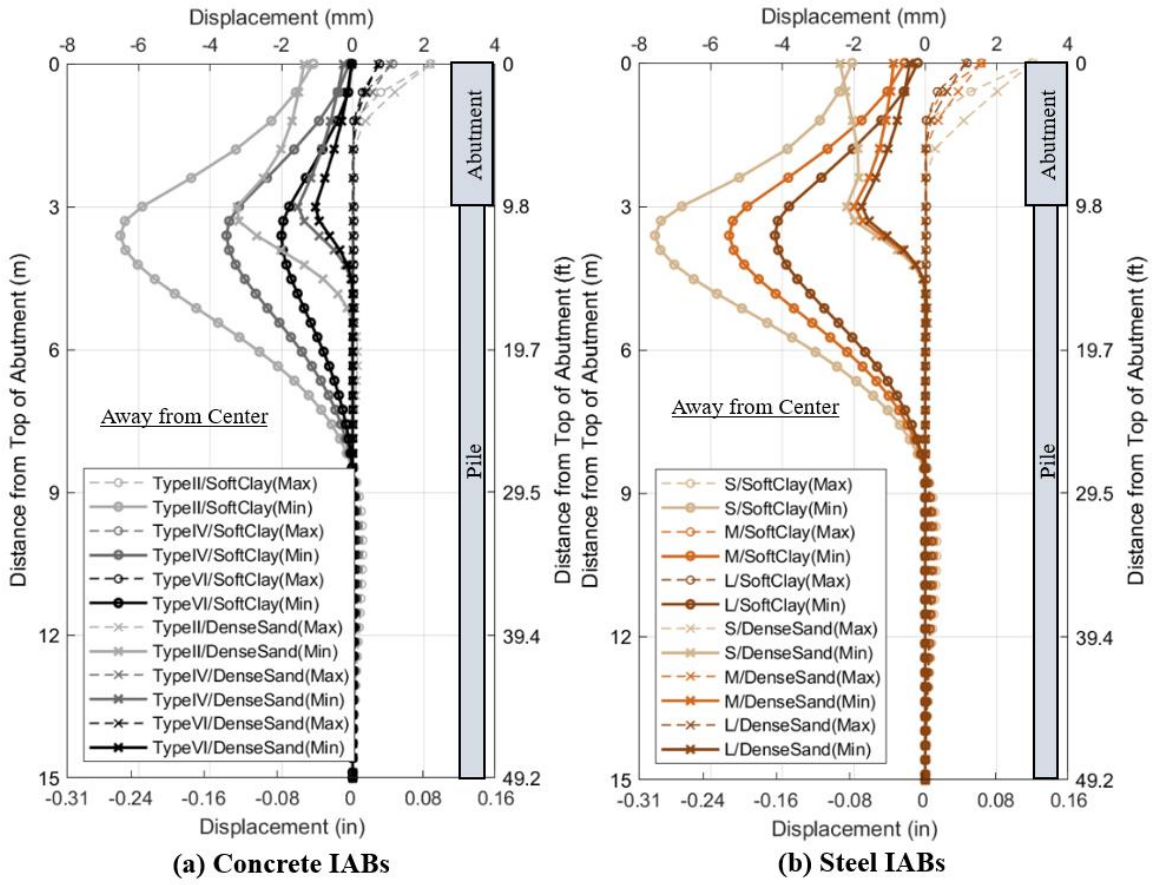

Figure 0.10: Substructure Displacement of (a) concrete and (b) steel girder IABs
Note: 40m span IABs with HP250x85 oriented about the weak axis

4.5 Bending Moment in Piles

This section presents the results of pile bending moment. The absolute maximum values of bending moment in piles were always recorded at the top of piles, and the left exterior pile was the most critical of the four piles for all IABs under the truck load. As an example, Figure 0.11 shows the typical envelope moment diagram of the critical pile of all truck positions, in this case oriented about the weak axis bending for 20m IABs with AASHTO Type II on soft clay and dense sand. There would be no discontinuity in the plot if a single truck location were evaluated.

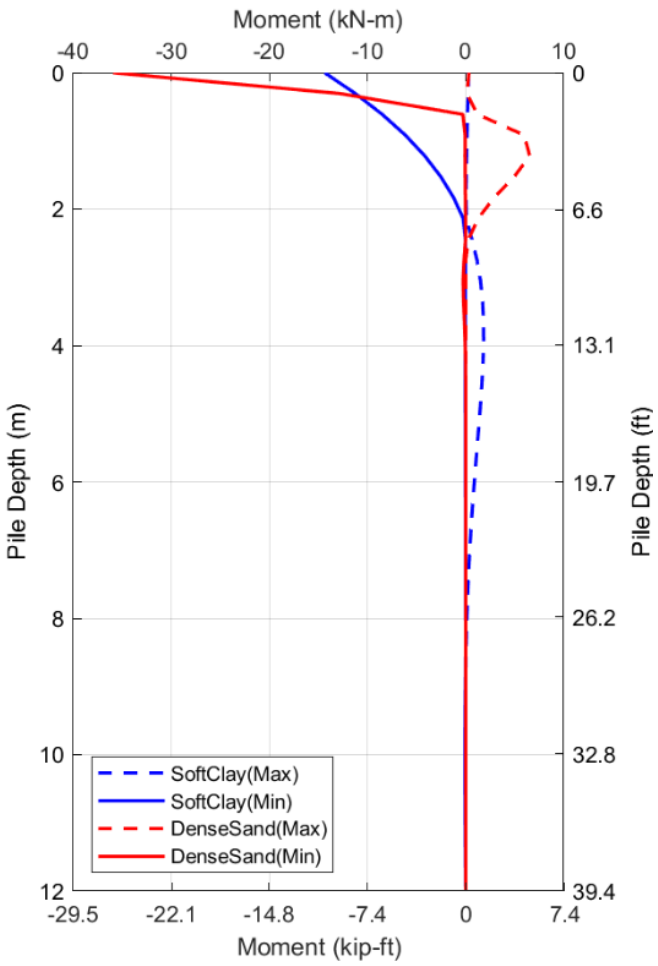

Figure 0.11: Typical Moment Diagram of Piles
Note: IAB parameters presented here are Span Length = 20m, Girder Size = AASHTO Type II, and Pile Orientation = Weak Axis

Figure 0.12 presents the comparison of maximum pile moment observed for IABs with varying girder size and soil condition, and HP250x85 oriented about the weak axis. The results showed that the values of maximum pile moment increased as the foundation soil becomes stiffer. The opposite trend from the superstructure moment was observed in pile moments; the IABs with smaller girders (more flexible superstructure) have higher pile moments. The results also showed that as span length increased, the pile moment increased.

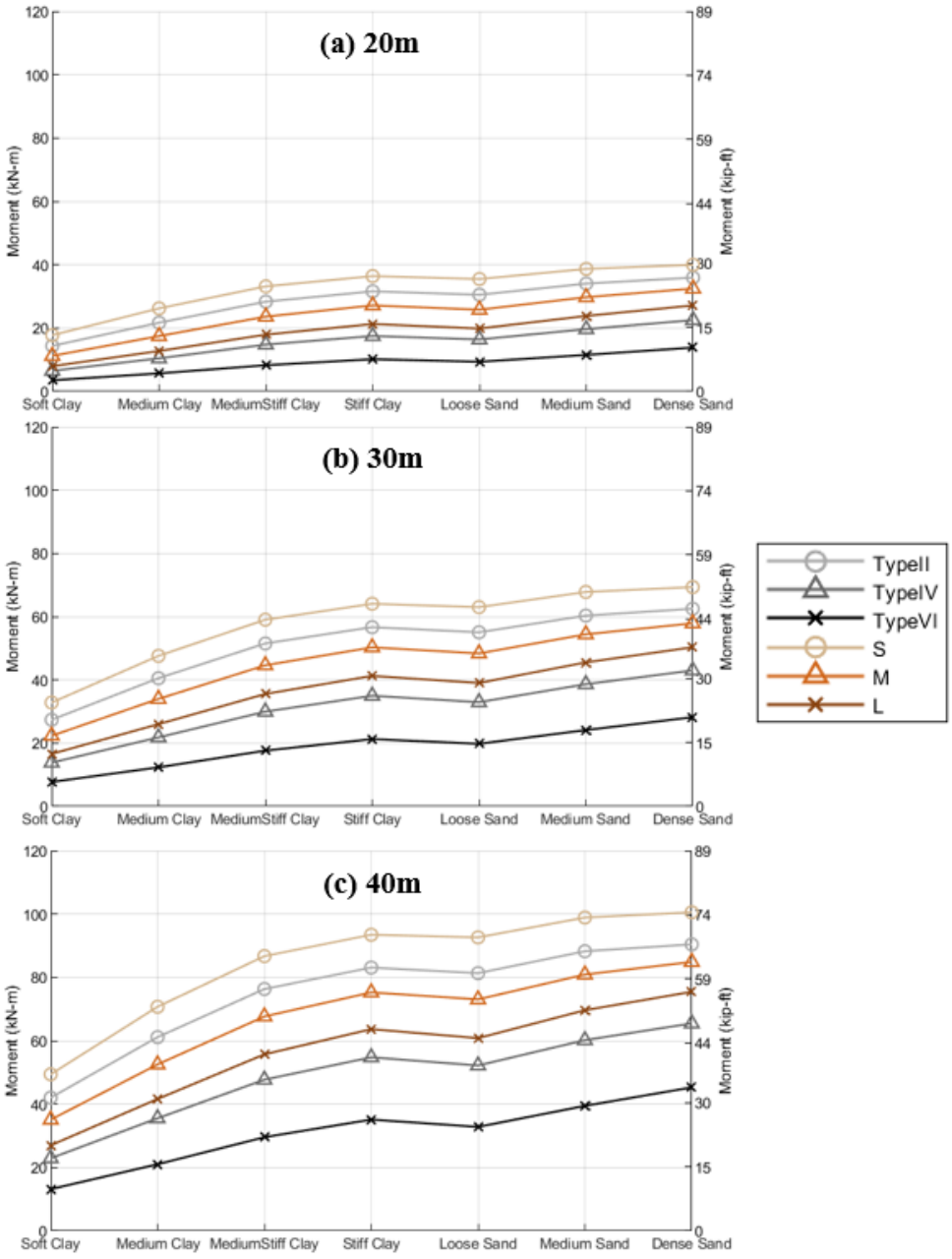

Figure 0.12: Maximum Pile Moment with Varying Girder Size and Soil Condition for (a)20m, (b)30m, and (c)40m IABs

Note: Pile = HP250x85 and Weak Axis Bending

4.5.1 Effect of Pile Orientation on Pile Bending Moment

This section focuses on the effect of pile orientation on pile bending moment for concrete girder IABs. Overall, the results showed that weak-axis pile orientation resulted in a lower value of moment in piles. However, the flexural capacity of piles is also significantly lower for the weak-axis orientation. The absolute maximum pile moment (M_{max}) was compared with the nominal yield capacity of the pile ($M_{y\_nominal}$) by computing the ratio of M_{max} to M_y. The ratio exceeding 1 indicates the yielding of piles, and it would require a more advanced analysis to provide meaningful results. The results showed that piles did not yield for either orientation or any parameters considered under a single load case of truck load. Load combinations will be evaluated in Chapter 5, and thus, pile yielding must be considered. Figure 0.13 presents examples of the results under truck load for the girder sizes that would be typical for the span length shown. The results of weak-axis bending resulted in almost twice as much ratio as the strong-axis bending results. The results are limited for concrete girder IABs, and the effect of pile orientation for steel IABs is further evaluated in Chapter 5.

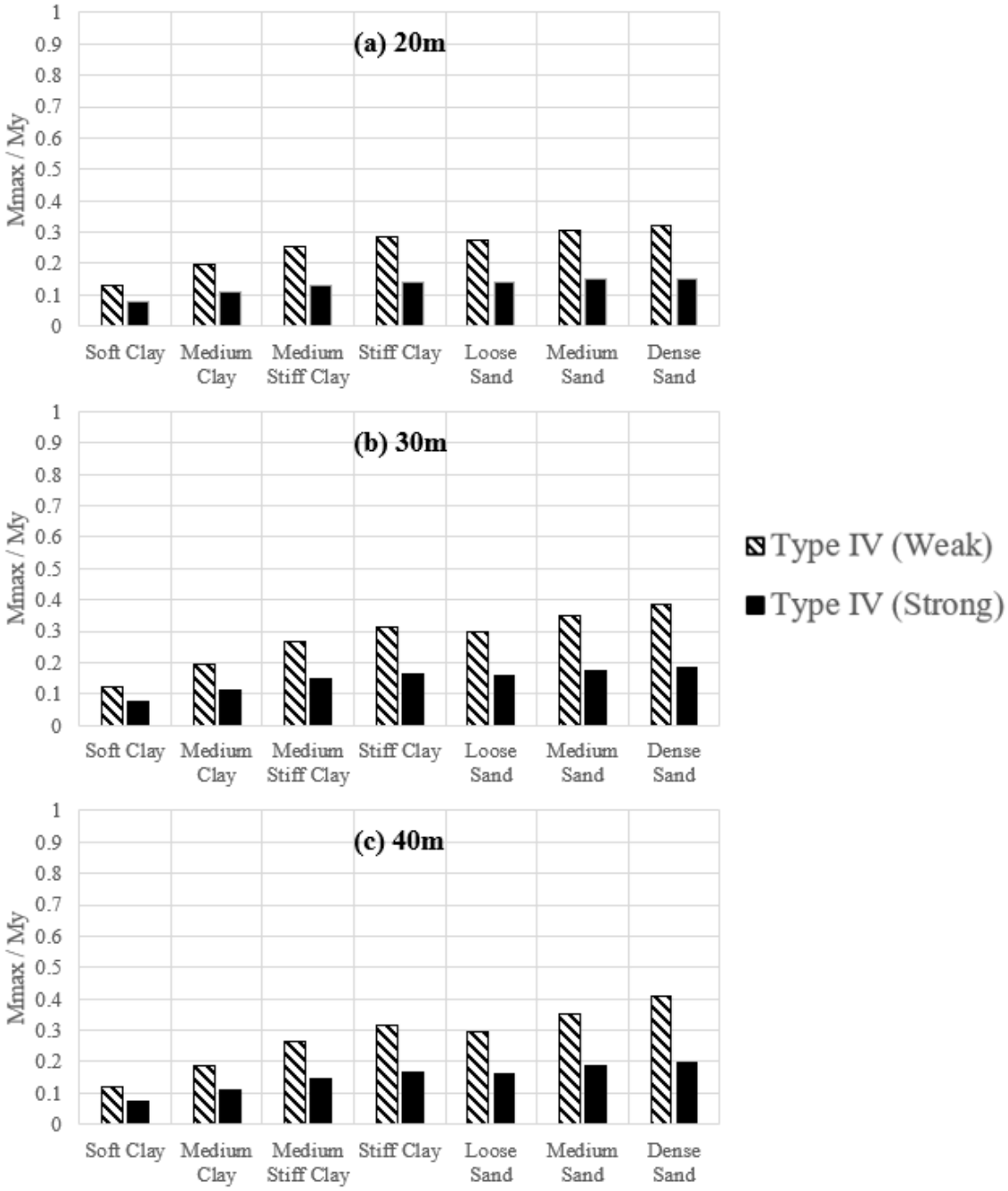

Figure 0.13: The Ratio of Maximum Pile Moment and Yield Capacity for (a)20m, (b)30m, (c)40m IABs with Ideal Girder Size

4.6 Discussion of Results

Effects of various parameters on bridge responses were analyzed for the IABs subjected to truck load only, and the resulting LLDFs were compared with AASHTO LLDFs. This section discusses and summarizes the results presented in this chapter.

When compared to typical moment diagrams of SSBs, the fixity of superstructure and substructure in IABs shifted the overall moment diagram downwards, resulting in negative moments at the end-span and lower maximum superstructure moments (full bridge cross section and girder moments) at mid-span in IABs. This shift in the moment diagram was related to the relative stiffness of superstructure to substructure of IABs. When stiffer soil was present around piles (lower relative stiffness of superstructure to substructure), the shift of moment diagram became greater; less maximum superstructure moments at mid-span and more negative moments at end-span were observed. Since more moments were transferred from the superstructure (greater absolute value of negative end-span moments), a larger value of moment was transferred to substructure, resulting in a higher pile moment. Stiffer foundation soil also limits the movement of substructure, resulting in smaller displacements and rotations of substructure. Since stiffer foundation soil forced the pile to remain in the original position, it caused a sharper transition in curvature at the bottom of the abutment; this also led an increase in maximum pile moment.

IABs with larger girders increase the relative stiffness of superstructure to substructure for a given pile. Increasing the girder size resulted in a greater value of superstructure moments at mid-span and a smaller value of pile moment. When the maximum moment in superstructure increases, the moment diagram shifts upwards and a

decreasing value of moment was transferred to substructure, resulting in a smaller pile moment. Stiffer superstructure limited the rotations of abutment, and thus resulted a smaller substructure displacement.

The effects of pile orientation were also analyzed in this chapter. Although the pile orientation had minimal effects on superstructure moments, it significantly affects the pile moment. The weak-axis orientation produced a much lower value of maximum pile moment due to a greater pile flexibility, however, the ratio of maximum pile moment to the yield moment was greater for the weak-axis orientation. Even though the pile moment resulted in a greater percentage of pile yield moment, the weak-axis orientation may be preferable to reduce the force transfer between the pile and abutment, avoiding the potential concrete cracking of abutment. Overall, under the single load case of truck load, the pile did not yield for either orientation or other parameters considered in this chapter. However, a relatively high pile moment was observed for longer span IABs, thus a larger pile size and non-linear material properties of piles will be included in Chapter 5.

Furthermore, the applicability of AASHTO LLDFs for SSBs and proposed LLDFs for concrete IABs by Dicleli and Erhan (2009) were evaluated based on the resulting LLDFs from FE analysis of this research. LLDFs were computed for one and two design loaded lanes and for interior and exterior girder moments. For the exterior girder moment of IABs analyzed in this study, the AASHTO equations for SSBs predicted a higher LLDF for one design loaded lane; this did not agree with the results of IABs because two design loaded lanes always controlled for exterior girder moment of IABs. Overall, the AASHTO LLDF values may be overly conservative to use for IABs if the girder moments were estimated from the simply supported beam analysis, as the

AASHTO LLDFs were 20-50% greater than the resulting LLDFs from the 2-D simply supported analysis. Since AASHTO LLDF equations were developed for SSBs, the fixity of superstructure and substructure in IABs was not considered, thus the AASHTO LLDF equations estimated greater values compared to LLDFs resulted from the FEMs of IABs.

The LLDFs were also estimated using the 2-D rigid frame analysis that included the effects of substructure stiffness present in IABs. The superstructure stiffness and foundation soil stiffness had minimal impacts on the LLDFs of IABs resulted from the rigid frame analysis. For IABs with ideal girder sizes for that span, the resulting LLDFs from the rigid frame analysis were closer to the AASHTO LLDFs. The differences for interior girder moment were within ±10%, and the AASHTO LLDFs were up to 25% larger for exterior girder moment. The LLDFs computed using the proposed equations by Dicleli and Erhan (2009) generally agreed with the resulting LLDFs from the 2-D rigid frame analysis for interior girder moments (only up to 7% difference). However, the resulting LLDFs for the exterior girder moments were up to 20% greater than the LLDFs computed using the proposed equation. Even though the equations were developed for concrete IABs, the results were relatively similar for steel IABs as well.

CHAPTER 5

INELASTIC ANALYSIS OF INTEGRAL ABUTMENT BRIDGES

This chapter presents the results of the inelastic finite element analysis investigating the effect of various loads and foundation soil conditions for single-span IABs of varying bridge geometries and soil conditions. The major difference from the previous chapter is that this analysis includes soil nonlinearity and material nonlinearity in all FEMs. This analysis also includes thermal loads and AASHTO load combinations that were not considered in Chapter 4. The objective was to analyze the effects of the soil and geometric parameters on bridge responses: full bridge and girder bending moments, substructure displacement and rotation, and pile bending moments.

Most results presented in this chapter include an envelope solution of all possible truck locations; there would be no discontinuity in the plot if a single truck location were evaluated. Dead load was not included in the results presented in this chapter since it was analyzed separately on simply supported beams and presented in Chapter 3. However, dead load induces superstructure moments on IABs in addition to the live and thermal loads, thus, the results of dead load in Chapter 3 must be superimposed on the results of superstructure moments presented in this chapter; the superstructure moment at mid-span increases by the amount of mid-span moment induced by dead load which will be noted in applicable figures for reference. Due to the assumptions made on the construction of IABs in this study, dead load has no influence on the results of substructure results and end-span superstructure moments. Thermal loads applied on steel and concrete IABs are different as described in Section 2.5.3; steel IABs are subjected to larger thermal loads.

Additionally, the p-Δ effects were also neglected due to the substructure displacement is small even under combined loads.

Table 0.1 and Table 0.2 present the number of models with varying pile orientations evaluated in this chapter. AASHTO Type II and small steel girders, AASHTO Type IV and medium steel girders, and AASHTO Type VI and large steel girders are ideal girder sizes for 20m, 30m, and 40m span IABs, respectively (the diagonal cells in the tables). Furthermore, HP250x85 and HP310x125 are typical pile sizes for 20m bridges and 30m or 40m bridges, respectively. In each cell in the tables, the two numbers indicate the number of bridges with varying soil types for each pile size listed at the top of the table. IABs with non-ideal girder and pile sizes were also investigated to study the effect of varying stiffness, thus a total of 392 models were reported. The plastic moment capacities of the composite deck sections with each girder size are listed in Table 0.3, and all IABs with ideal girder sizes satisfied the capacity. Since the critical mid-span moment was way below the plastic flexural capacity of the composite deck (only 50 to 60% of the plastic flexural capacity with an addition of factored dead load), it was assumed that addition of dead load would not cause the structure to enter the nonlinear range; this allows the results of dead load to be superimposed to the results presented here. The axial load caused by dead load is already accounted in moment-curvature relationship in piles.

Table 0.1: Number of IABs with Weak-Axis Orientation Reported in Chapter 6

Weak-Axis Bending (HP250x85/HP310x125)							
		CONCRETE			STEEL		
		Type II	Type IV	Type VI	S	M	L
20m	Uncracked	7/7	3/3	3/3	7/7	3/3	3/3
	Cracked	7/7	-	-	7/7	-	-
30m	Uncracked	3/3	7/7	3/3	3/3	7/7	3/3
	Cracked	-	7/7	-	-	7/7	-
40m	Uncracked	3/3	3/3	3/7	3/3	3/3	3/7
	Cracked	-	-	3/7	-	-	3/7

Table 0.2: Number of IABs with Strong-Axis Orientation Reported in Chapter 6

Strong-Axis Bending (HP250x85/HP310x125)							
		CONCRETE			STEEL		
		Type II	Type IV	Type VI	S	M	L
20m	Uncracked	3/7	3/3	3/3	3/7	3/3	3/3
	Cracked	3/3	-	-	3/3	-	-
30m	Uncracked	3/3	3/7	3/3	3/3	3/7	3/3
	Cracked	-	3/3	-	-	3/3	-
40m	Uncracked	3/3	3/3	3/7	3/3	3/3	3/7
	Cracked	-	-	3/3	-	-	3/3

Table 0.3: Plastic Flexural Capacities of Deck for IABs with Ideal Girders based on Nominal Properties [kN-m (kip-ft)]

Girder Size	**Composite Girder**	**Composite Full Bridge Cross Section**
AASHTO Type II	4060 (2990)	16220 (12000)
AASHTO Type IV	9360 (6910)	37440 (27600)
AASHTO Type VI	21010 (15500)	84040 (62000)
S	4960 (3660)	19860 (14600)
M	9080 (6700)	36310 (26800)
L	13980 (10300)	55920 (41200)

5.1 Results of Superstructure Bending Moment

This section presents the effects of each parameter analyzed in this study on superstructure bending moments: the full bridge cross section and girder bending moments. The values of bending moment about the center of gravity of deck were recorded for IABs as full bridge cross section bending moment, and the values of moment about the center of gravity of the composite girder were recorded for each girder.

5.1.1 Full Bridge Cross Section Bending Moment

Typical full bridge cross section moment diagrams are shown in Figure 0.1-5.4 for 20m and 40m span IABs with ideal concrete and steel girders built on soft clay and dense sand under three individual load types. Figure 0.5-5.8 represent the typical full bridge cross section moment diagrams for these bridges under all possible Strength 1 load combinations. These figures represent typical full bridge cross section moment diagrams for all IABs analyzed in this study. The results of all 30m span and other foundation soil stiffness fell between these results.

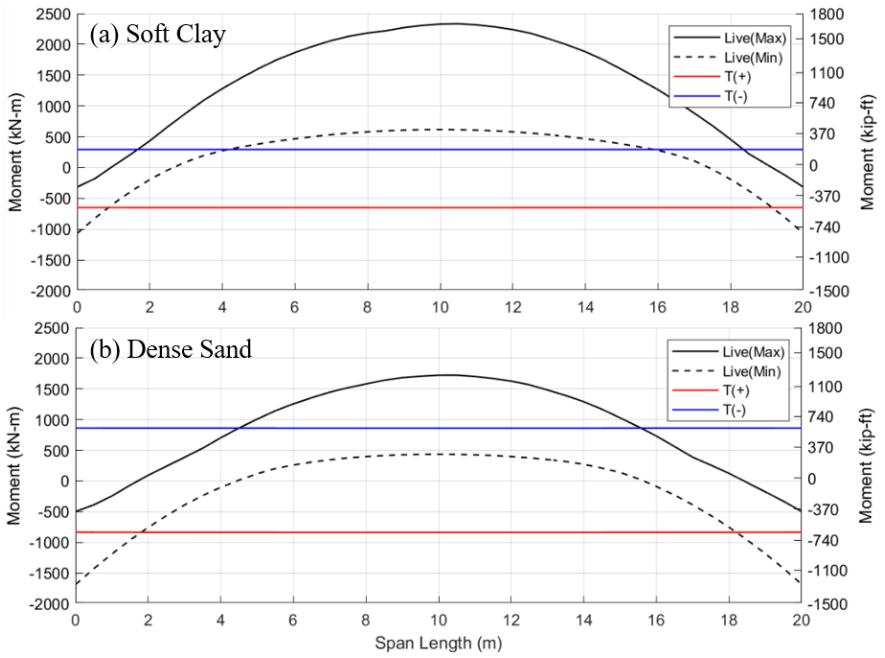

Figure 0.1: Full Bridge Cross Section Bending Moment under Individual Load Cases for 20m IABs with AASHTO Type II on (a)Soft Clay and (b)Dense Sand

IAB parameters: Span Length = 20m, Girder = AASHTO Type II, and Pile = HP310x125 and Weak Axis Bending

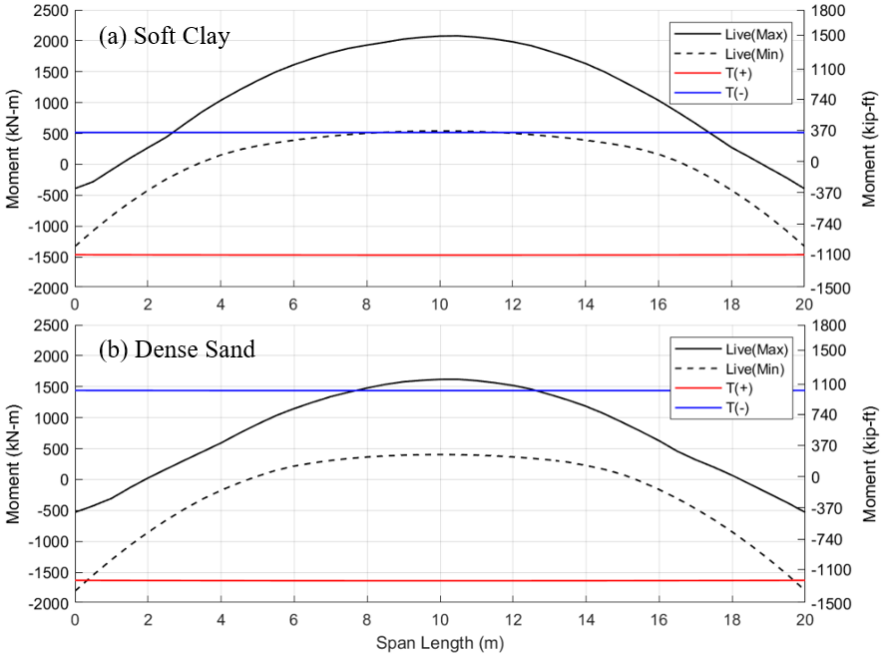

Figure 0.2: Full Bridge Cross Section Bending Moment under Individual Load Cases for 20m IABs with Small Steel Girders on (a)Soft Clay and (b)Dense Sand

IAB parameters: Span Length = 20m, Girder = Small Steel, and Pile = HP310x125 and Weak Axis Bending

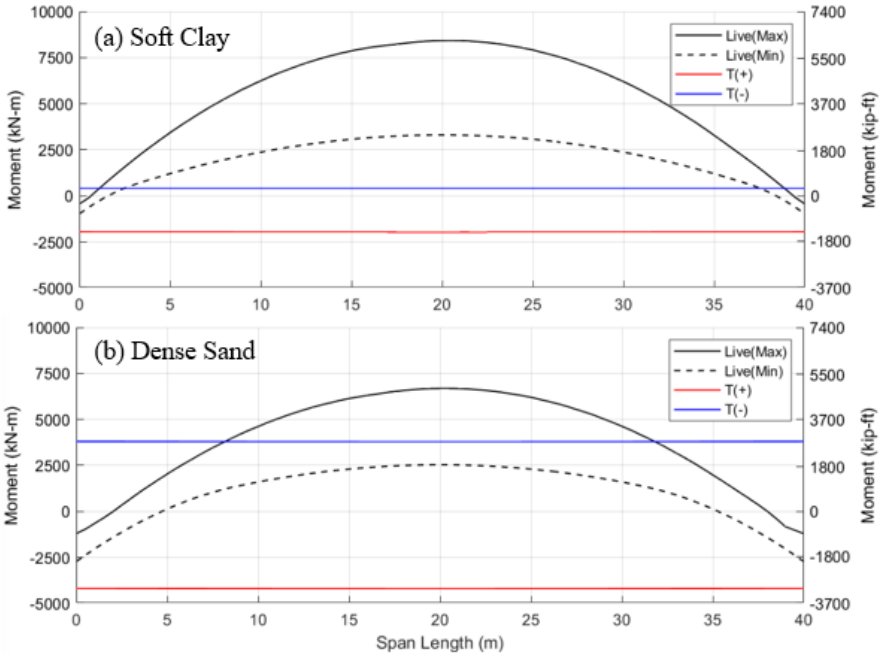

Figure 0.3: Full Bridge Cross Section Bending Moment under Individual Load Cases for 40m IABs with AASHTO Type VI on (a)Soft Clay and (b)Dense Sand

IAB parameters: Span Length = 40m, Girder = AASHTO Type VI, and Pile = HP310x125 and Weak Axis Bending

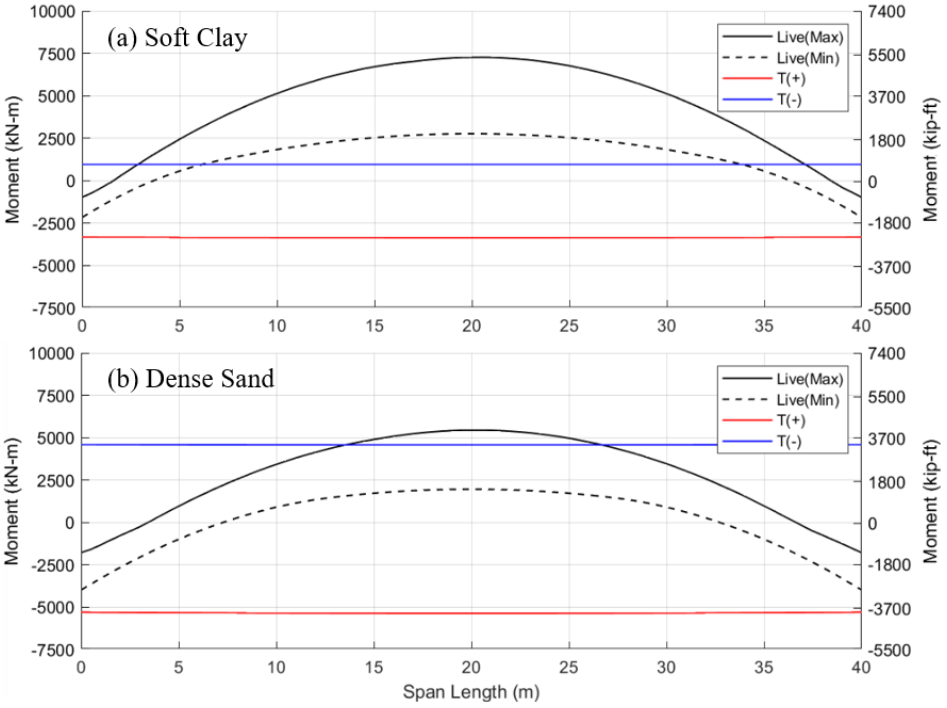

Figure 0.4: Full Bridge Cross Section Bending Moment under Individual Load Cases for 40m IABs with Large Steel Girders on (a)Soft Clay and (b)Dense Sand

IAB parameters: Span Length = 40m, Girder = Large Steel, and Pile = HP310x125 and Weak Axis Bending

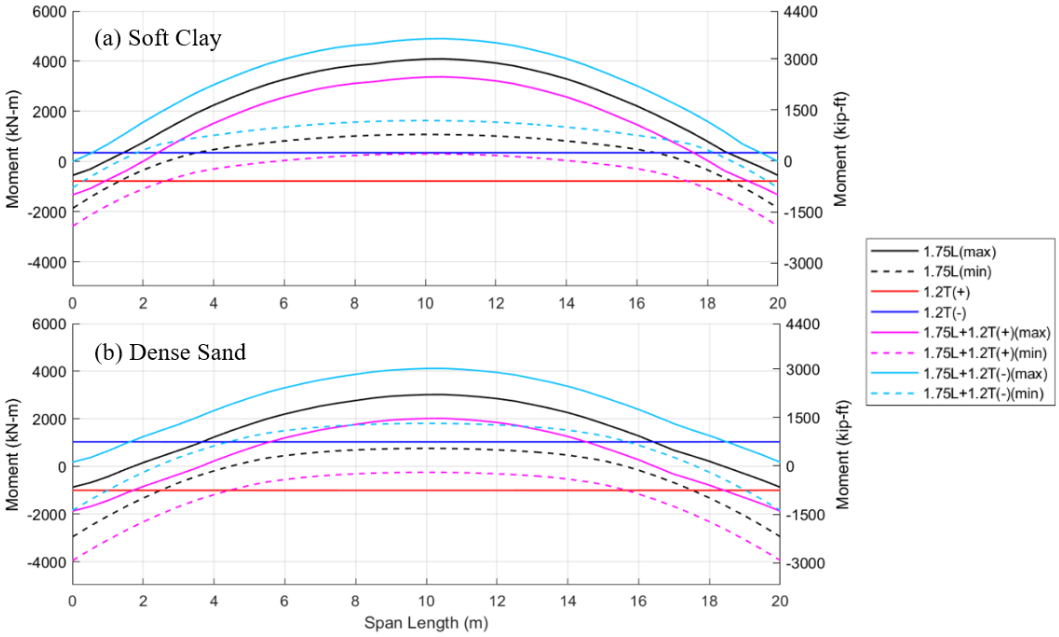

Figure 0.5: Full Bridge Cross Section Bending Moment under Strength 1 Load Combinations for 20m IABs with AASHTO Type II on (a)Soft Clay and (b)Dense Sand

Note: 1.25D = 4230kN-m (3120kip-ft) at mid-span is not included.

IAB parameters: Span Length = 20m, Girder = AASHTO Type II, and Pile = HP310x125 and Weak Axis Bending

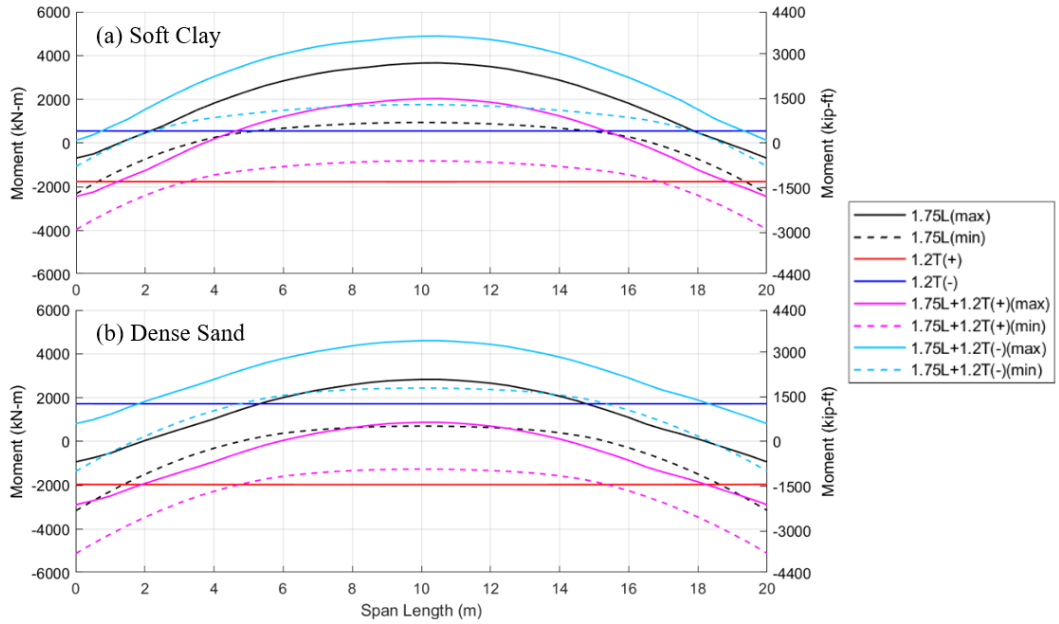

Figure 0.6: Full Bridge Cross Section Bending Moment under Strength 1 Load Combinations for 20m IABs with Small Steel Girders on (a)Soft Clay and (b)Dense Sand

Note: 1.25D = 3350kN-m (2470kip-ft) at mid-span is not included.

IAB parameters: Span Length = 20m, Girder = Small Steel, and Pile = HP310x125 and Weak Axis Bending

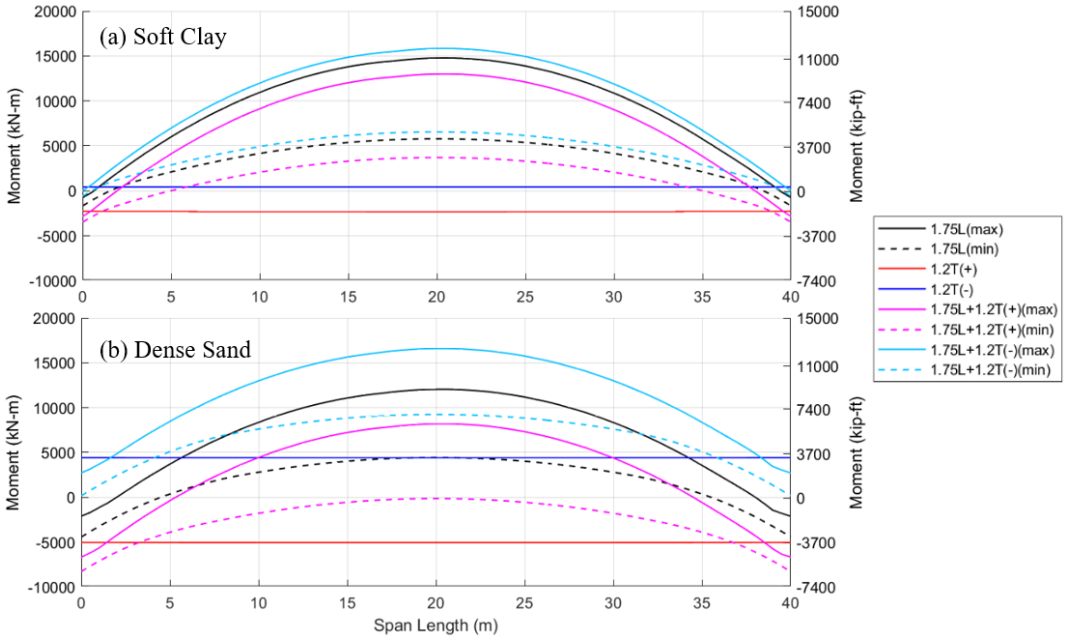

Figure 0.7: Full Bridge Cross Section Bending Moment under Strength 1 Load Combinations for 40m IABs with AASHTO Type VI on (a)Soft Clay and (b)Dense Sand

Note: 1.25D = 27800kN-m (20500kip-ft) at mid-span is not included.

IAB parameters: Span Length = 40m, Girder = AASHTO Type VI, and Pile = HP310x125 and Weak Axis Bending

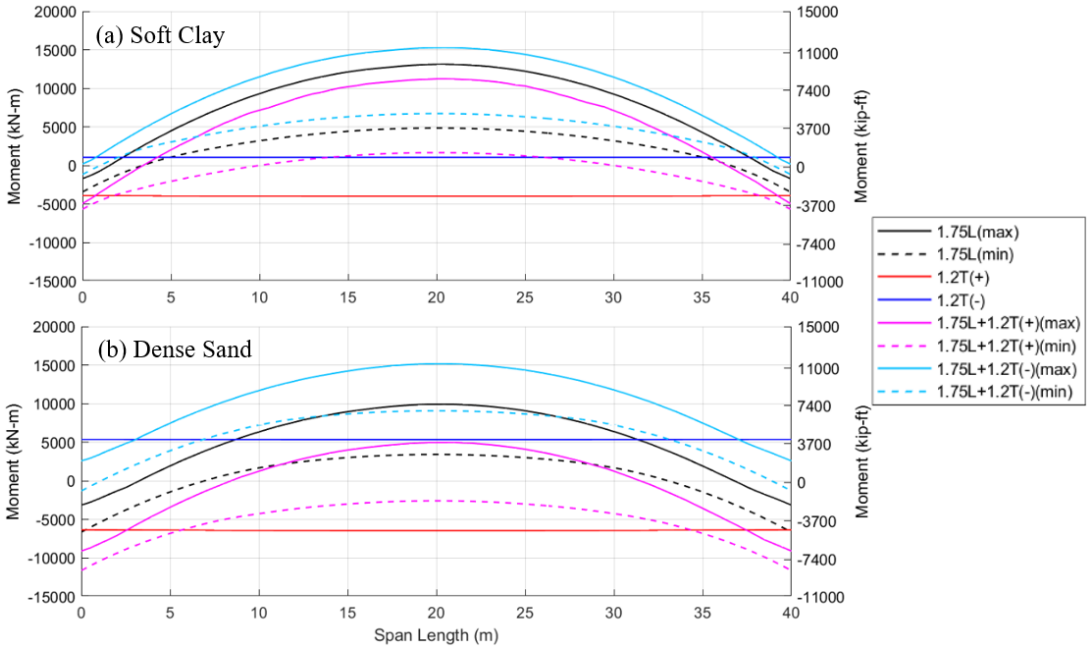

Figure 0.8: Full Bridge Cross Section Bending Moment under Strength 1 Load Combinations for 40m IABs with Large Steel Girders on (a)Soft Clay and (b)Dense Sand

Note: 1.25D = 15140kN-m (11160kip-ft) at mid-span is not included.

IAB parameters: Span Length = 40m, Girder = Large Steel, and Pile = HP310x125 and Weak Axis Bending

As observed in Figure 0.1-5.8, the maximum moment was recorded at the mid-span and the minimum moment was recorded at the end-span under live load and the load combinations that include live load. The moment diagrams under thermal loads were constant throughout the span, as the longitudinal movement is restrained by the rotation of the substructure, applying a concentrated moment at these locations. Expansion of the bridge would result in arching upward of the superstructure, and contraction an arching downward. Figure 0.1-5.4 also showed that the maximum moment at the mid-span under live load was smaller for the IABs with dense sand than with soft clay, shifting the entire moment diagram to the negative direction. Thus, more negative moment was observed at end-span for the IABs with dense sand due to greater fixity from the foundation. For the moment under thermal loads, a larger positive moment for the negative temperature change (T(-)) and larger negative moment for the positive temperature change(T(+)) were recorded for the IABs built on dense sand. Therefore, the load combinations with T(-) resulted in larger positive mid-span moments and the combinations with T(+) resulted in larger negative end-span moments in Figure 0.5-5.8.

Figure 0.9-5.12 present the maximum and minimum full bridge cross section moment values under possible Strength 1 load combinations for the 20m and 40m IABs with ideal concrete and steel girders for each span on all foundation soil conditions; (a) of each figure presents the maximum full bridge moment, and (b) of each figure presents the minimum full bridge moment for each IAB with varying soil conditions. As also observed in the previous figures, the maximum and minimum moments were always recorded at the mid-span and end-span, respectively. For the maximum full bridge cross

section moment shown in (a) of each figure, the center span moment would increase by the moment induced by dead loads which is noted in each figure, while end-span moments would remain unchanged due to pin-roller conditions when dead load is applied.

The results showed that the critical load combination for maximum (most positive) and minimum (most negative) moments are 1.75L + 1.2T(-) and 1.75L + 1.2T(+), respectively; this was true for all IABs analyzed in this study. Even though five possible load combinations were presented in each figure from Figure 0.9 to 5.12, the trend of the plots in (a) is almost identical to the trend of the plots in (b) under the same load combination; the change in maximum moment from soft clay to dense sand under one load combination is almost the same as the change in minimum moment from soft clay to dense sand under this load combination. This demonstrates that the overall shape of moment diagram under the same load combination remained unchanged, but the moment diagram shifted depending on soil conditions and load combinations.

Figure 0.9-5.12 also showed the effect of foundation soil stiffness under each individual load case. The results showed that the maximum moment increased under live load and positive thermal load but decreased under the negative thermal change as the foundation soil becomes stiffer. Thus, when live and negative thermal loads were combined (1.75L+1.2T(-)), the effects from each load counteracted and the moment became relative consistent under 1.75L+1.2T(-) load combination. On the other hand, when live and positive thermal loads were combined (1.75L+1.2T(+)), the decreasing rate of the trend became more significant as the foundation soil becomes stiffer.

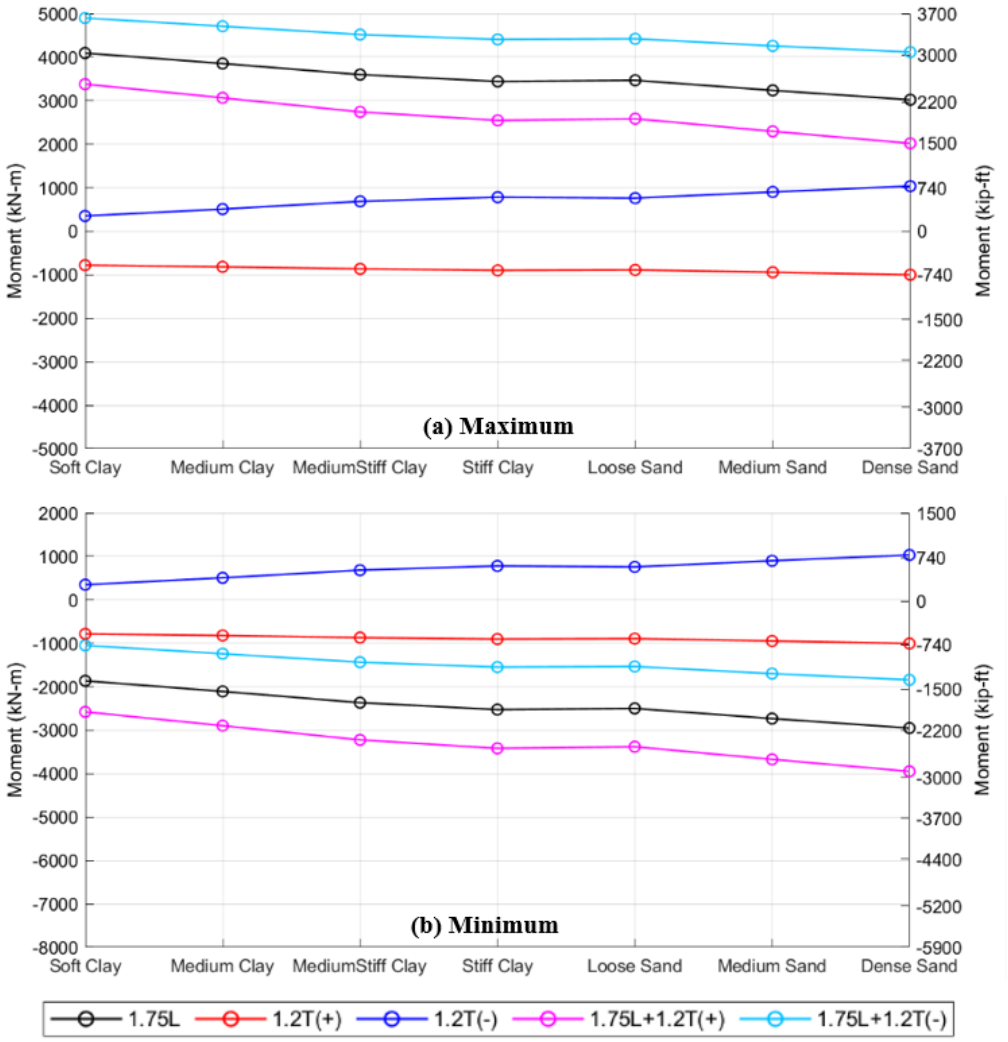

Figure 0.9: (a)Maximum and (b)Minimum Full Bridge Cross Section Moment for 20m IABs with AASHTO Type II under Strength 1 Load Combinations

Note: (a) 1.25D = 4230kN-m (3120kip-ft) is not included.

IAB parameters: Span Length = 20m, Girder = AASHTO Type II, and Pile = HP310x125 and Weak Axis Bending

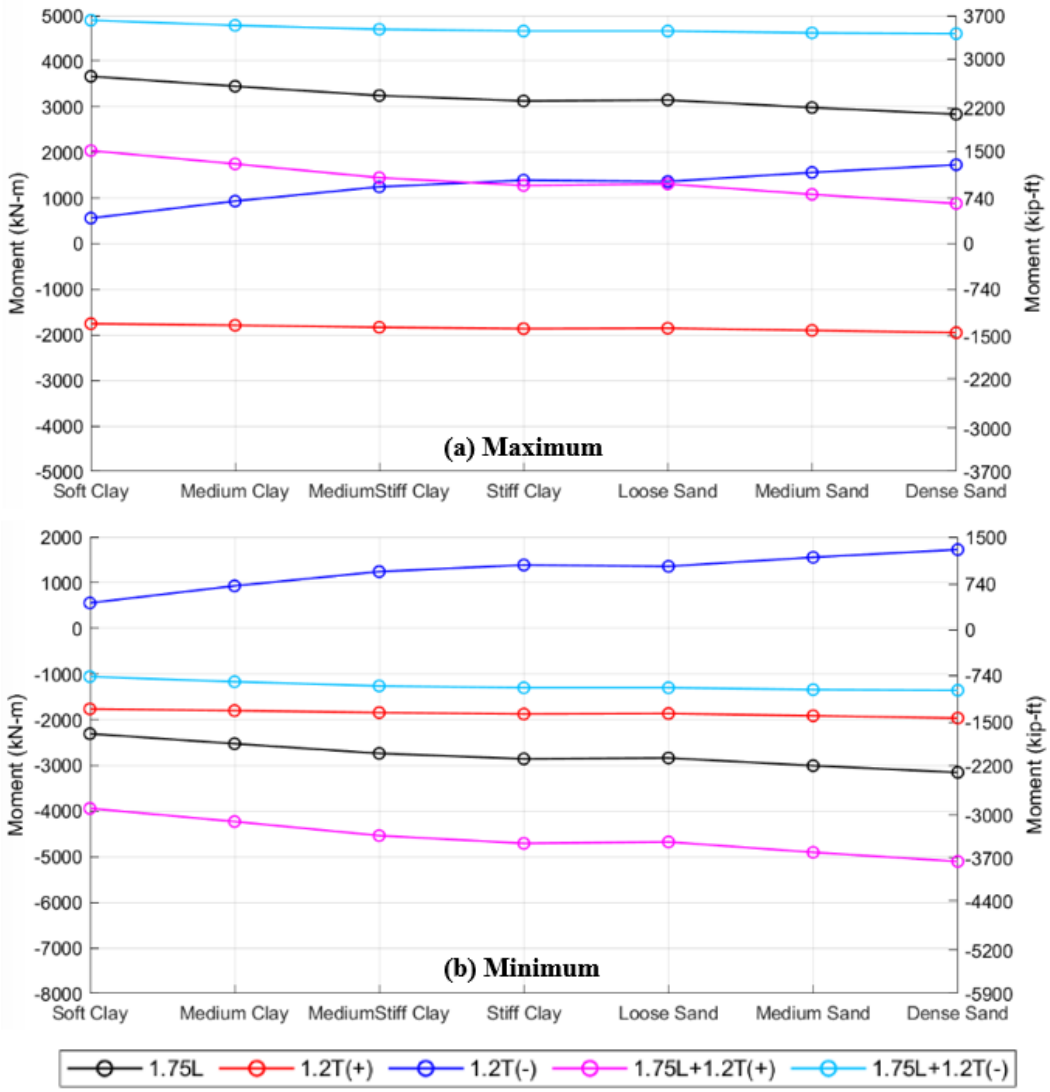

Figure 0.10: (a)Maximum and (b)Minimum Full Bridge Cross Section Moment for 20m IABs with Small Steel Girders under Strength 1 Load Combinations

Note: (a) 1.25D = 3349kN-m (2470kip-ft) is not included.

IAB parameters: Span Length = 20m, Girder = Small Steel, and Pile = HP310x125 and Weak Axis Bending

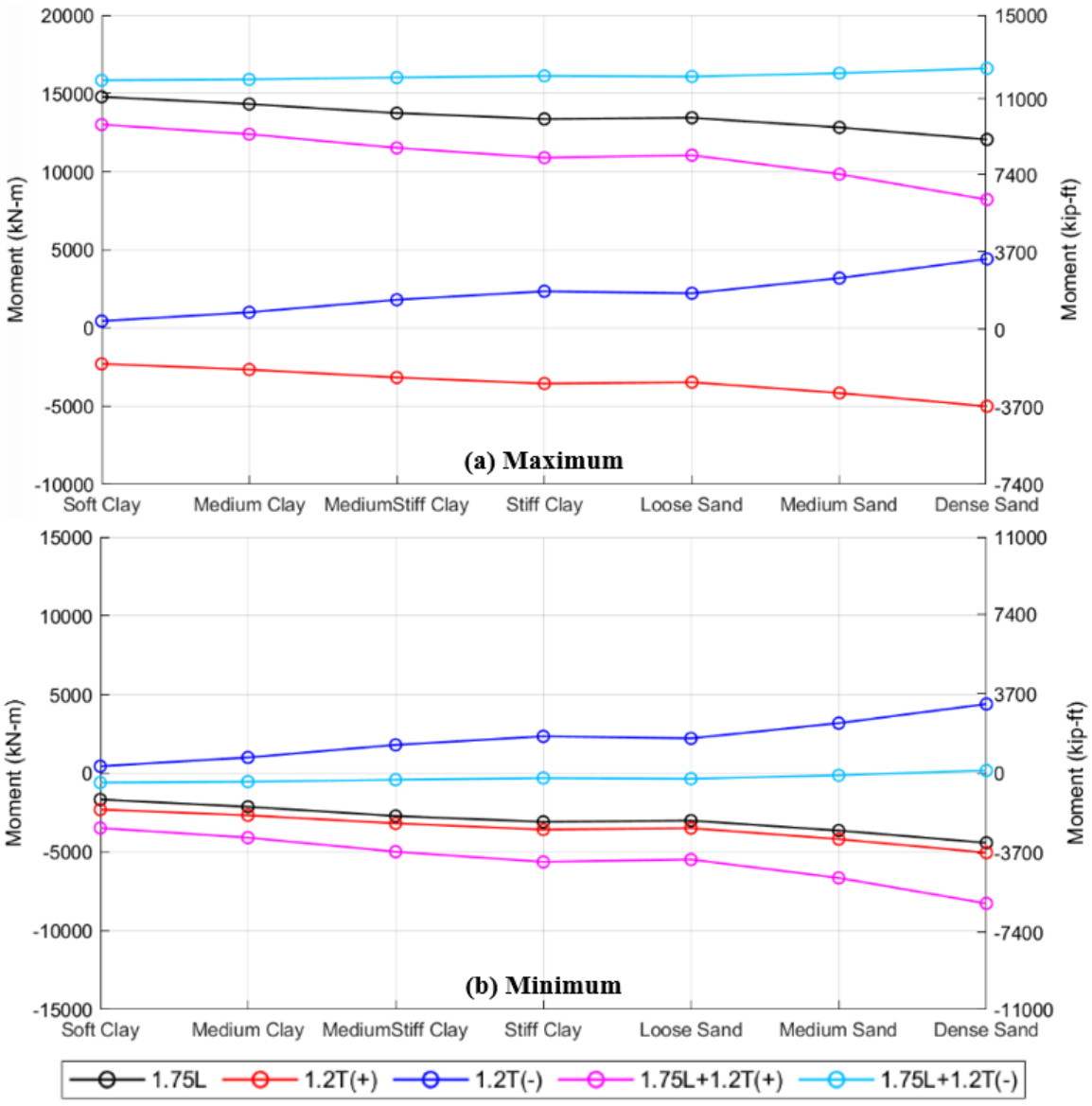

Figure 0.11: (a)Maximum and (b)Minimum Full Bridge Cross Section Moment for 40m IABs with AASHTO Type VI under Strength 1 Load Combinations

Note: (a) 1.25D = 27804kN-m (20508kip-ft) is not included.

IAB parameters: Span Length = 40m, Girder = AASHTO Type VI, and Pile = HP310x125 and Weak Axis Bending

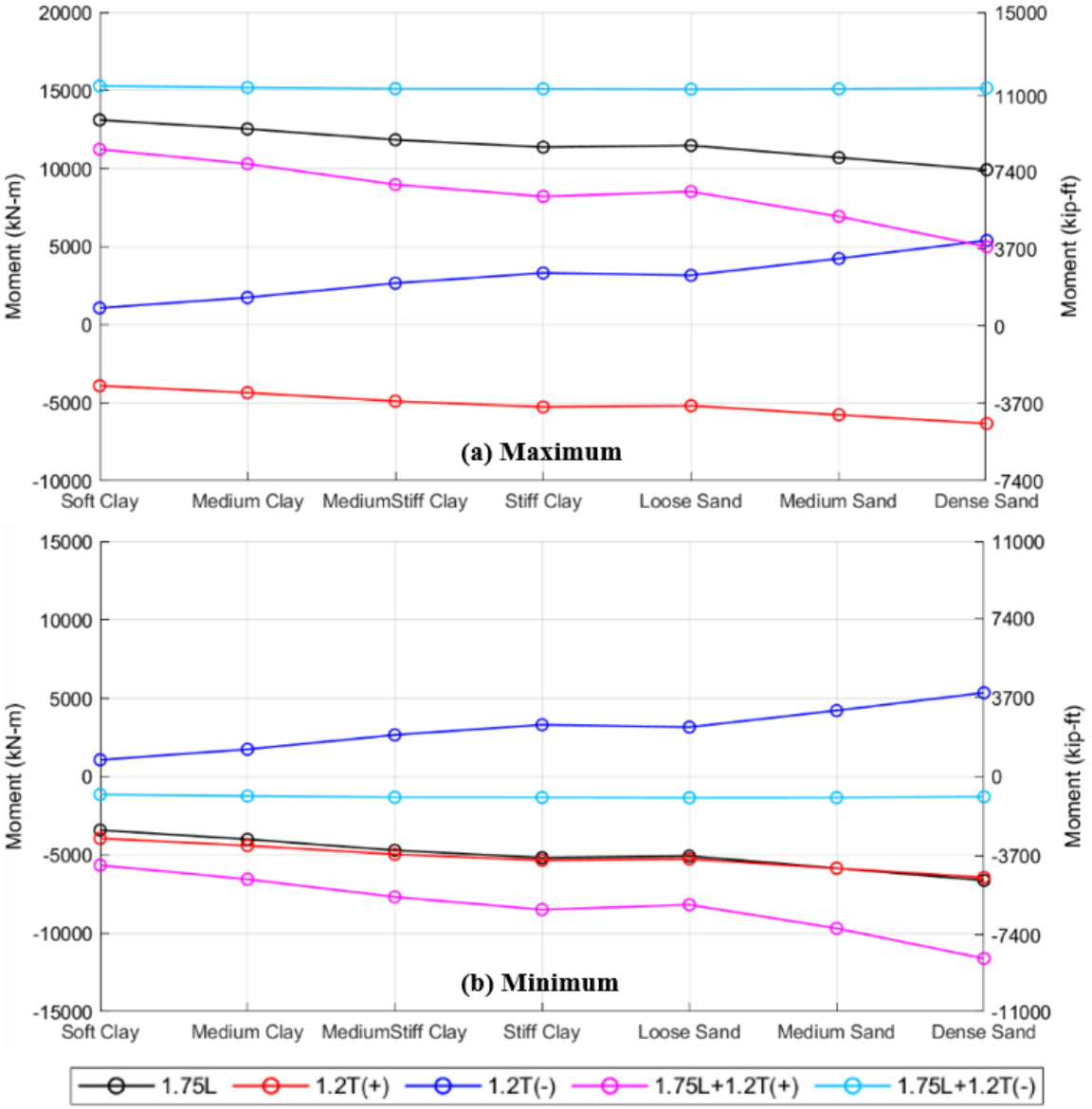

Figure 0.12: (a)Maximum and (b)Minimum Full Bridge Cross Section Moment for 40m IABs with Large Steel Girders under Strength 1 Load Combinations

Note: (a) 1.25D = 15136kN-m (11164kip-ft) is not included.

IAB parameters: Span Length = 40m, Girder = Large Steel, and Pile = HP310x125 and Weak Axis Bending

Figure 0.13 shows the maximum positive full bridge cross section moment recorded at the mid-span under the critical Strength 1 load combination (1.75L + 1.2T(-)) for all uncracked and cracked IABs with ideal girders and varying foundation soil conditions. The difference between cracked and uncracked sections for concrete IABs is

larger due to girders also being cracked. Overall, the maximum full bridge cross section moment recorded at the mid-span under the critical load combination (1.75L+1.2T(-)) was relatively consistent for all ideal girder IABs studied in this analysis: approximately 4500kN-m, 10000kN-m, and 16100kN-m for 20m, 30m, and 40m uncracked concrete girder IABs and 4700kN-m, 9600kN-m, and 15200kN-m for 20m, 30m, and 40m uncracked steel girder IABs, respectively. This result indicates that the effect of foundation soil stiffness becomes minimal on the critical mid-span moment. When the concrete cracking was included, these values were decreased by approximately 5 to 15%. Dead load (1.25D) was not included in the results presented in Figure 0.13. Even after dead load was factored and added to the results, they were all below the flexural plastic capacities of deck.

As mentioned previously in Section 4.1, a continuity of superstructure and substructure in IABs shifts the moment diagram downward under live load, and thus the superstructure mid-span moments of SSBs are usually conservative to use for the design of IABs. However, due to thermal load effects, the maximum full bridge cross section moment at mid-span increased and became relatively close to the live load results of simply supported beam analysis that was factored by 1.75 of Table 0.5, especially for longer span IABs: 6000kN-m, 10800kN-m, and 16400kN-m for 20m, 30m, and 40m bridges. However, the superstructure moments highly depend on the superstructure stiffness, and negative superstructure moments are present at end-span in IABs. Therefore, analyzing both live and thermal loads is still significant to capture the effects from each load case.

Figure 0.14 presents the minimum full bridge cross section moment under the critical Strength 1 load combination (1.75L + 1.2T(+)). It is important to note that the critical Strength 1 load combination for minimum and maximum full bridge cross section moment differed, and therefore, a varying trend was observed for minimum full bridge cross section moment; 1.75L+1.2T(-) load combination does not control for minimum full bridge cross section moment. Unlike the maximum moment under its critical load combination (1.75L + 1.2T(-)) in Figure 0.13, minimum full bridge cross section moment decreased significantly as soil foundation stiffened under its critical load combination (1.75L + 1.2T(+)), meaning that more negative moment at the end-span was recorded at end-span in IABs with stiffer foundation soil. This agreed with the trend observed from each individual load case: decreasing trend under both live and positive thermal loads with increasing in foundation stiffness. The effect of foundation soil became more apparent in IABs with longer span lengths since overall effects from each load become larger. The results also showed that the effect of concrete cracking was almost negligible for end-span moment in steel IABs. The concrete cracking increased the absolute value of negative moment for concrete IABs but became less important in dense sand. The effect of each load with increasing soil stiffness on the shift of moment diagram is summarized in Table 0.4.

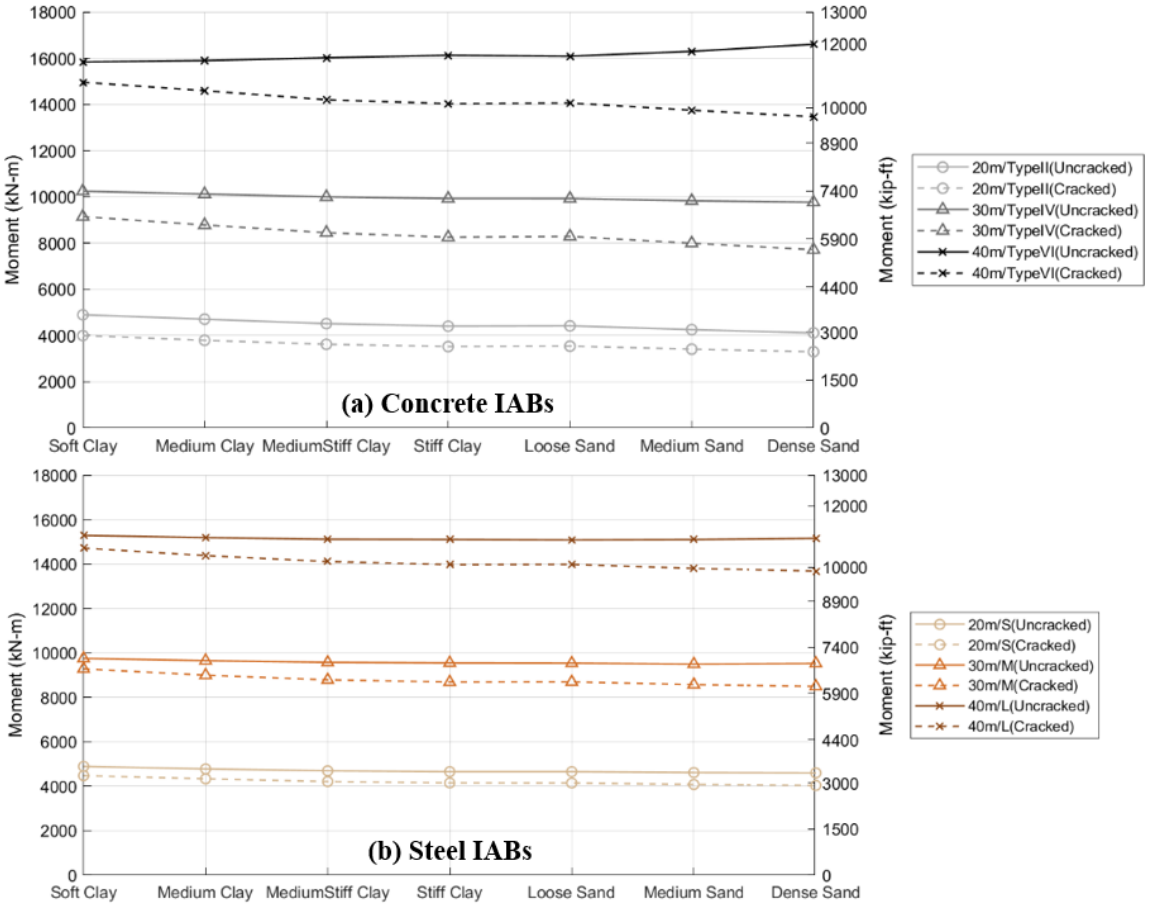

Figure 0.13: Maximum Mid-Span Full Bridge Cross Section Moment under 1.75L+1.2T(-) for (a)Concrete IABs and (b)Steel IABs

Note: 1.25D is not included.

IAB parameters: Pile = HP310x125 and Weak Axis Bending

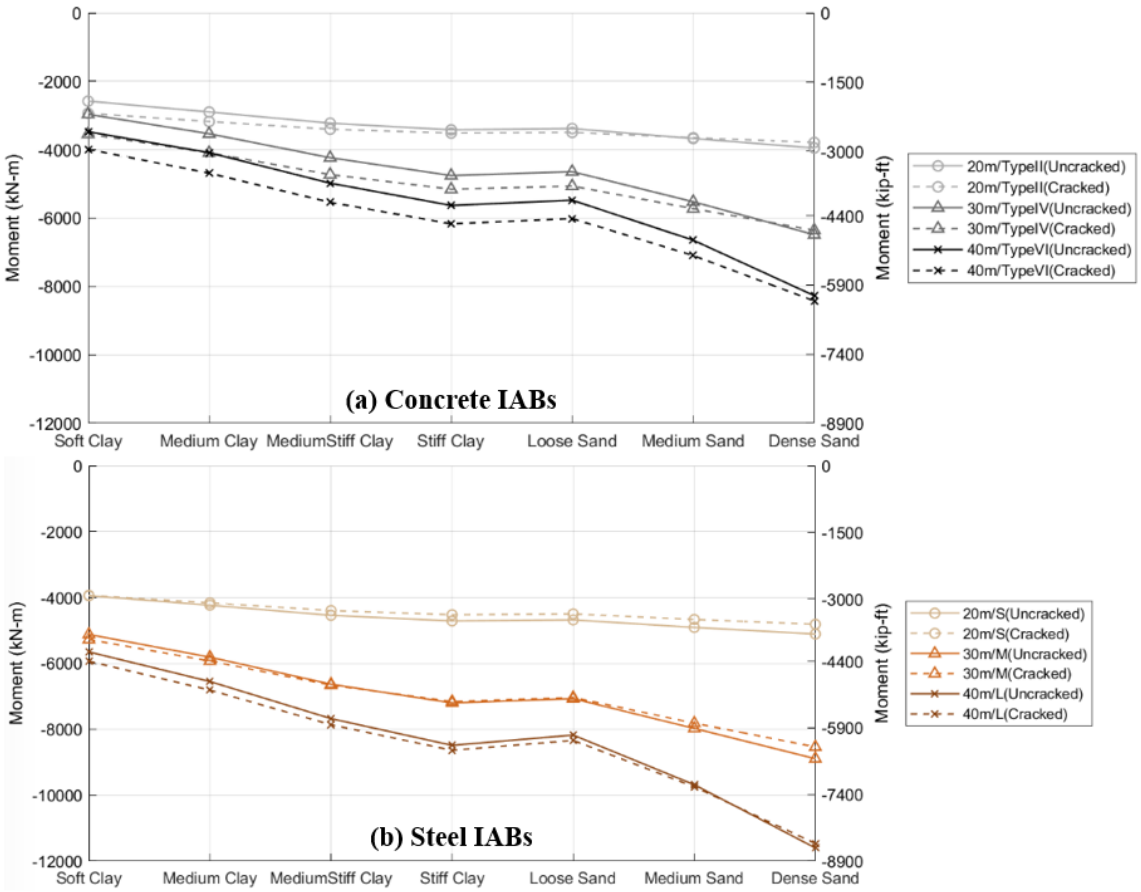

Figure 0.14: Minimum End-Span Full Bridge Cross Section Moment under 1.75L + 1.2T(+) for (a)Concrete IABs and (b)Steel IABs
Note: IAB parameters: Pile = HP310x125 and Weak Axis Bending

Table 0.4: Summary of Effects of Foundation Soil Stiffness

Load Cases	Direction of Shift in Moment Diagram from Soft Clay to Dense Sand
T(+)	Downward
T(-)	Upward
L	Downward
1.75L+1.2T(-)	Constant
1.75L+1.2T(+)	Downward

The maximum mid-span full bridge cross section moment under the critical load combination (1.75L+1.2T(-)) for all uncracked IABs with varying span lengths, girder sizes, and foundation soil stiffness is presented in Figure 0.15. These include the IABs with unrealistic girder sizes, but they were compared to analyze the effect of the relative stiffness of superstructure to substructure on the maximum mid-span moment. Even though all seven-foundation soil stiffnesses were analyzed for the IABs with ideal girder sizes, only three-foundation soil stiffnesses were analyzed for the IABs with unrealistic girder sizes; the results of IABs with other soil stiffness were assumed to follow the trend.

The results showed that regardless of the substructure stiffness, the mid-span moment increased as girder size increased; this was resulted from greater relative rotational stiffness of the superstructure to substructure. Dead load would also increase due to these larger girders but is not included in these results. As previously observed, the effects of live and negative loads are opposite with the change in foundation soil stiffness; mid-span moment decreases under live load and increases under negative thermal change as the foundation soil becomes stiffer. As the girder size increases for a given span, the effect from negative thermal load increases due to the increase in relative rotational stiffness of superstructure to substructure, thus this also increases the rate of change in increasing in the moment as foundation soil became stiffer. When the girder size decreases for a given span (lower relative rotation stiffness of superstructure to substructure), the effect from negative thermal load becomes less significant, and the effect of live load becomes dominating; this results in decreasing trend in the mid-span moment as foundation soil becomes stiffer. Additionally, the effect from the thermal

loads is more significant in longer span bridges, and less significant in shorter span bridges. From these trends and effects of each load case, increasing trends of the mid-span moment was observed in 20m span bridges with the largest girders (stiffest superstructure), and decreasing trends of the mid-span moment was observed for 40m span bridges with the smallest girders (most flexible superstructure).

The increase of the relative rotational stiffness of superstructure to substructure by increasing the girder size always increases the mid-span moment, but the effects of increase in the relative stiffness of superstructure to substructure by loosening the foundation soil depend on the stiffness of superstructure for the given IAB. Overall, the mid-span moment was relatively consistent regardless of the substructure stiffness in IABs with ideal girder sizes, having the equal effects from live and thermal loads, as was also observed previously in Figure 0.13. Table 0.5 summarizes the trend in the rate of change in mid-span moments from soft clay to dense sand as girder sizes increases for individual load cases.

Table 0.5: Summary of Trend of Maximum Mid-Span Full Bridge Cross Section Moment as Foundation Soil Stiffness Increases

Load Cases	Rate of Change with Increasing Foundation Soil Stiffness and Girder Size
T(+)	Increase
T(-)	Increase
L	Constant (as also observed in Figure 0.2)

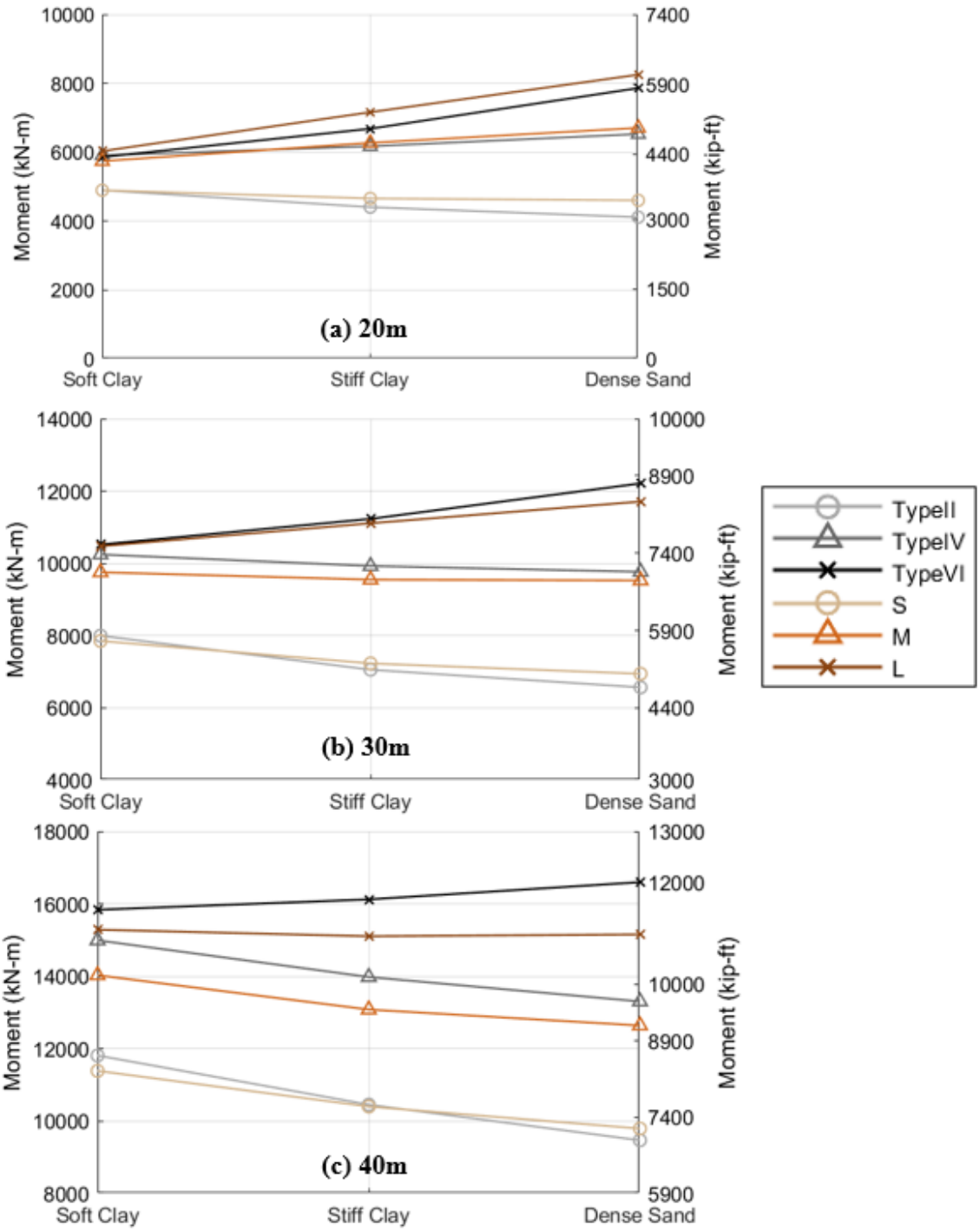

Figure 0.15: Maximum Mid-Span Full Bridge Cross Section Moment under 1.75L+1.2T(-) for (a)20m, (b)30m, and (c)40m IABs with Varying Girder Size
Note: 1.25D is not included.
IAB parameters: Pile = HP310x125 and Weak Axis Bending

Similarly, the minimum end-span full bridge cross section moment under its critical load combination (1.75L+1.2T(+)) for all uncracked IABs with varying span lengths, girder sizes, and foundation soil stiffness is presented in Figure 0.16. These also include the IABs with unrealistic girder sizes, but they were compared to analyze the effect of the relative stiffness of superstructure to substructure on the maximum negative end-span moment.

The results showed that generally, more negative moment was recorded at the end-span with stiffer foundation soil in all IABs due to the downward shifts caused by both live and positive thermal loads. IABs with steel girders resulted in more negative moments, and thus, a larger value of moment is distributed to the substructures of steel IABs. This is due to the larger effect that thermal load has on steel IABs than concrete IABs. The results also showed that when superstructure stiffness was compared, the change of rate in end-span moment from soft clay to dense sand is smaller for IABs with more flexible superstructure (with smaller girders). Stiffer superstructure increases the effects of both live and positive thermal loads, and the end-span moment increases more significantly as the foundation soil stiffness changes.

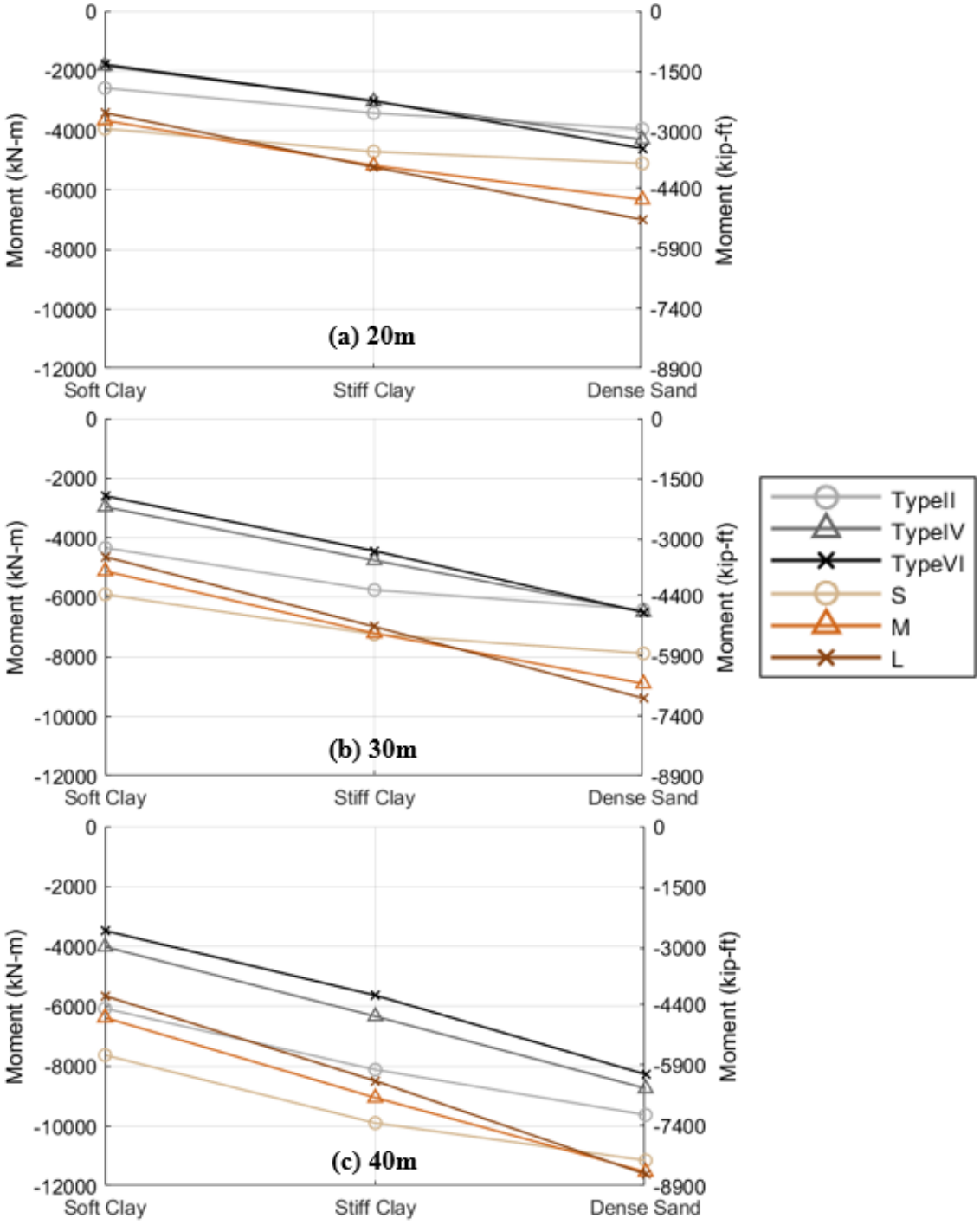

Figure 0.16: Minimum End-Span Full Bridge Cross Section Moment under 1.75L+1.2T(+) for (a)20m, (b)30m, and (c)40m IABs with Varying Girder Size
IAB parameters: Pile = HP310x125 and Weak Axis Bending

Additionally, the effect of pile sizes and orientation on the full bridge cross section moment was analyzed. Figure 0.17 presents the maximum full bridge cross section moment at mid-span for ideal girder IABs with varying pile sizes under its critical Strength 1 load combination (1.75L+1.2T(-)), and Figure 0.19 shows the maximum full bridge cross section moment at end span for the same IABs under its critical Strength 1 load combination (1.75L+1.2T(+)). Similarly, Figure 0.19 presents the mid-span moment under 1.75L+1.2T(-), and Figure 0.20 presents the end-span moment under 1.75L+1.2T(+) for ideal girder IABs with HP310x125 oriented about weak and strong axis bending.

The results showed that the pile geometry had minimal effects on the full bridge cross section moment at mid-span, as the effects from live load and thermal load counteracted; live load decreased, but thermal load increased as substructure stiffened. However, it had significant effects on end-span moment for 30m and 40m IABs. As substructure stiffened by a larger pile size or strong-axis orientation, it induced more negative moment at the end-span in addition to the foundation soil stiffness; more force would be transferred to substructure. This indicates that pile geometries also contributed to stiffening the substructure and shifted the moment diagram downward under the load combination of 1.75L+1.2T(+), but the substructure stiffness is negligible for the mid-span moment under 1.75L+1.2T(-) for any IABs and end-span moment under 1.75L+1.2T(+) for 20m IABs.

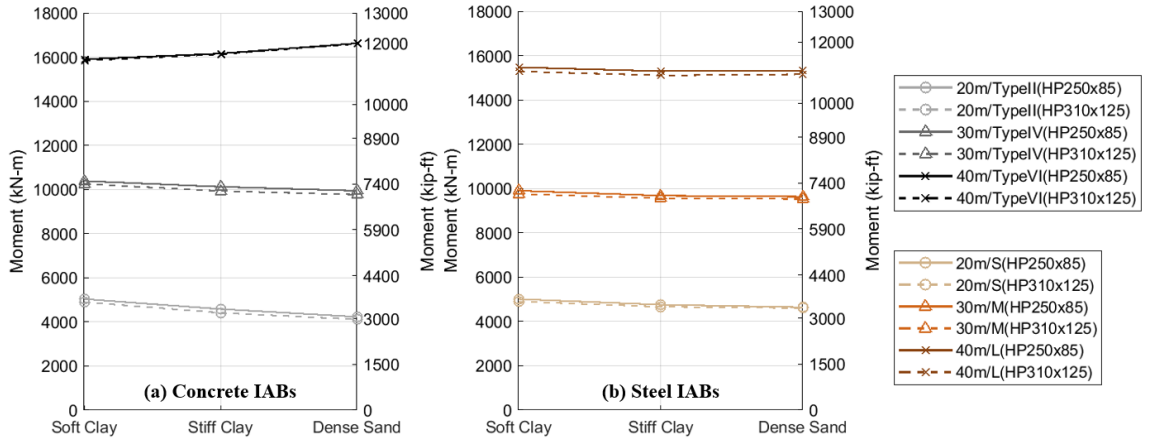

Figure 0.17: Maximum Full Bridge Cross Section Mid-Span Moment at Mid-Span under 1.75L + 1.2T(-) for (a)Ideal Concrete IABs and (b)Ideal Steel IABs with Varying Pile Sizes

Note: Dead load is not included.

IAB parameters: Uncracked sections, Pile = Weak Axis Bending

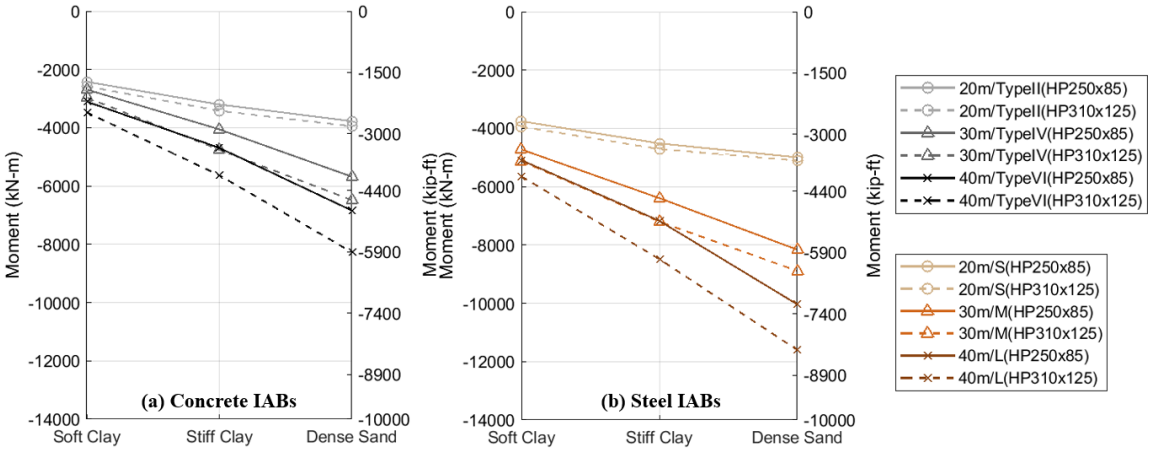

Figure 0.18: Maximum Full Bridge Cross Section End-Span Moment at Mid-Span under 1.75L + 1.2T(+) for (a)Ideal Concrete IABs and (b)Ideal Steel IABs with Varying Pile Sizes

Note: IAB parameters: Uncracked sections, Pile = Weak Axis Bending

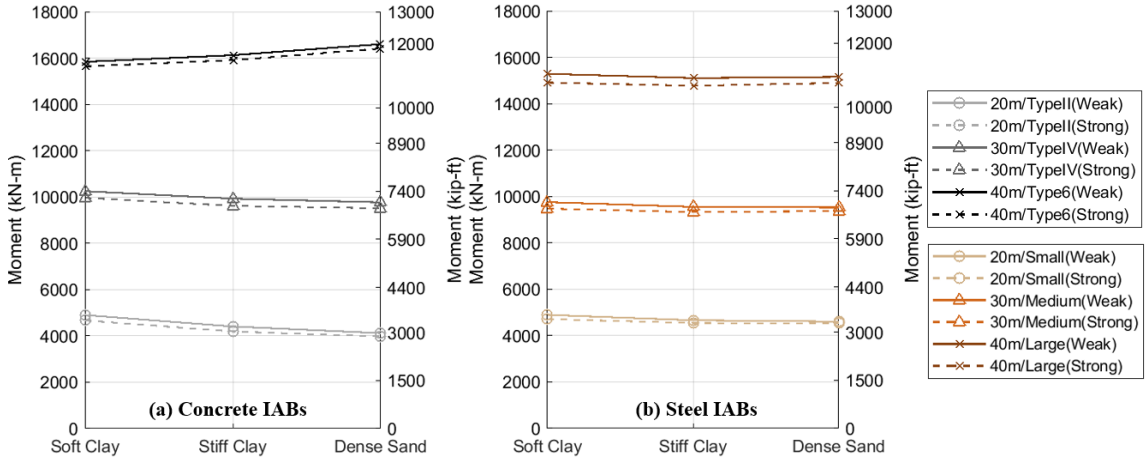

Figure 0.19: Maximum Full Bridge Cross Section Mid-Span Moment under 1.75L + 1.2T(-) for (a)Ideal Concrete IABs and (b)Ideal Steel IABs with Varying Pile Orientation

Note: Dead load is not included.

IAB parameters: Uncracked sections, Pile = HP310x125

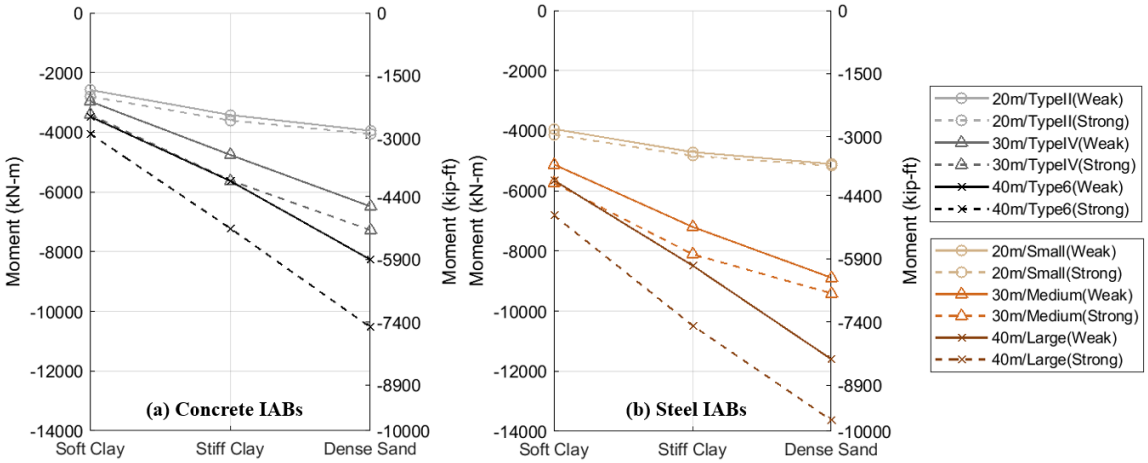

Figure 0.20: Maximum Full Bridge Cross Section End-Span Moment under 1.75L + 1.2T(+) for (a)Ideal Concrete IABs and (b)Ideal Steel IABs with Varying Pile Orientation

Note: IAB parameters: Uncracked sections, Pile = HP310x125

5.1.2 Bending Moment in Girders

Individual girder bending moment was also analyzed. The girder moments were expected to follow the similar trends as the full bridge cross section bending moment since the full bridge cross section moment is distributed to individual girders. The results presented in this section does not include the dead load; dead load was analyzed as SSBs in Chapter 4. However, the results of dead load presented in Chapter 4 must be superimposed when combined loads were considered. The dead load was assumed to be distributed equally to each girder and noted on applicable figures presented in this section. Distributions of live load only was considered in Chapter 5 with evaluation of LLDFs. Figure 0.21 and 5.20 present typical moment diagrams for the four individual girders of 40m IABs with ideal concrete and steel girders for that span built on soft clay and dense sand under the critical load combination (1.75L+1.2T(-)). All live load was concentrated on two lanes placed as close to the left edge of the bridges as allowed by AASHTO (2017).

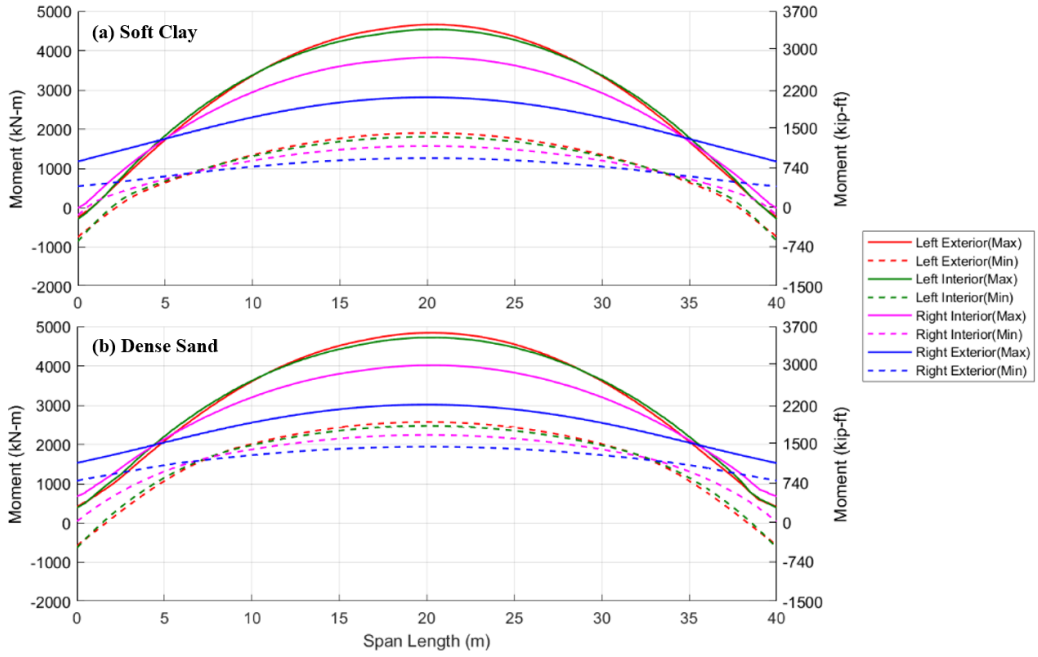

Figure 0.21: Typical Girder Moment Diagrams under 1.75L+1.2T(-) Load Combination for 40m IABs with AASHTO Type VI on (a)Soft Clay and (b)Dense Sand

Note: 1.25D = 6951kN-m (5127kip-ft) at mid-span is not included.

IAB parameters: Span Length = 40m, Girder = AASHTO Type VI, and Pile = HP310x125 and Weak Axis Bending

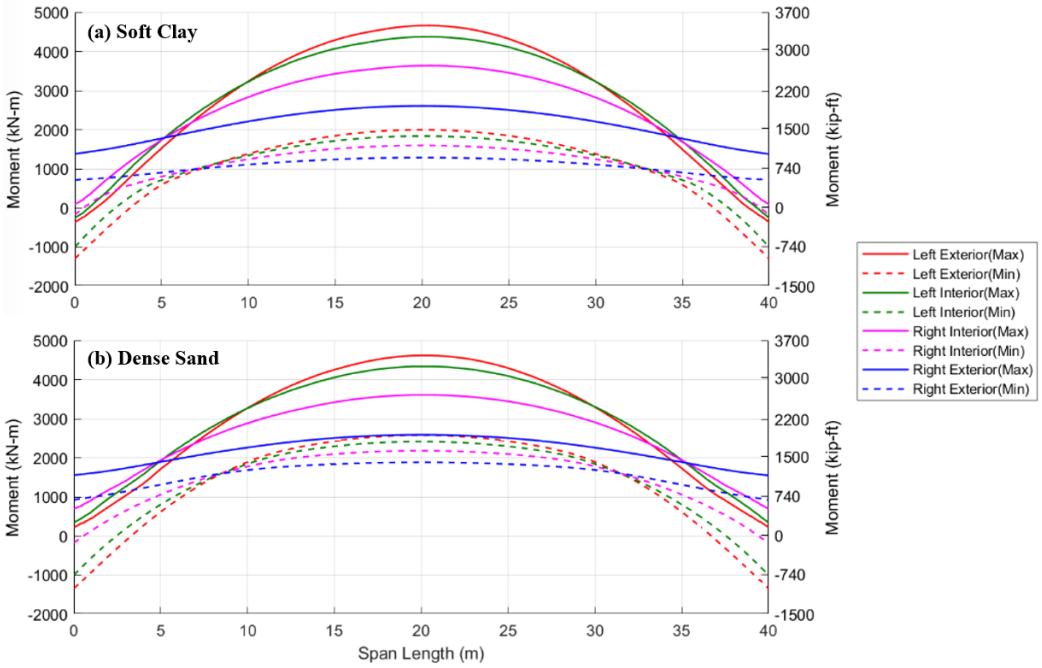

Figure 0.22: Typical Girder Moment Diagrams under 1.75L+1.2T(-) Load Combination for 40m IABs with Large Steel Girders on (a)Soft Clay and (b)Dense Sand

Note: 1.25D = 3784kN-m (2791kip-ft) at mid-span is not included.

IAB parameters: Span Length = 40m, Girder = Large Steel, and Pile = HP310x125 and Weak Axis Bending

Due to truck load being placed on the left side of the bridge, girder moments were higher on left exterior and left interior girders than right exterior and right interior girders. The left exterior girder moment was critical for all 40m span IABs, and the left interior girder moment was critical for some 20m and 30m span IABs. The difference between left exterior and interior girders were always within 10%, thus, the critical girder moment was compared even though the location of critical girder may be different. From the previous section, the critical Strength 1 Load combination for maximum and minimum superstructure moments were determined to be 1.75L+1.2T(-) and 1.75L+1.2T(+), respectively; this was also true for girder moments.

Figure 0.23 shows the maximum positive girder moment recorded at the mid-span under its critical Strength 1 load combination (1.75L+1.2T(-)) for all uncracked and cracked ideal girder IABs with HP310x125 oriented about the weak axis bending and varying foundation soil conditions. The results showed the trend of plots in Figure 0.23 is identical to the trends observed for full bridge cross section moment in Figure 0.13. Therefore, the observation made in the full bridge cross section moment is also true for the girder moment; the effect of substructure stiffness is minimal. The results also showed that the maximum mid-span girder moment was about 30% of the maximum mid-span full bridge cross section moment recorded for all IABs, regardless of bridge geometries and foundation soil. The moment induced by thermal load was equally distributed to each girder, but the moment induced by live load was distributed more heavily on two left girders. This resulted in approximately 5% higher critical mid-span girder moment than the quarter of critical mid-span full bridge cross section moment presented in Figure 0.13.

Figure 0.24 shows the minimum girder moment recorded at the end-span under its critical Strength 1 load combination (1.75L+1.2T(+)). Similarly, the minimum girder moment had identical trends as the minimum full bridge cross section moment presented in Figure 0.14. As similarly observed in Figure 0.14, the stiffness of foundation soil has effects on the minimum girder moment; more negative moment was observed with stiffer foundation soil, and the effect of foundation soil is more significant for longer span IABs.

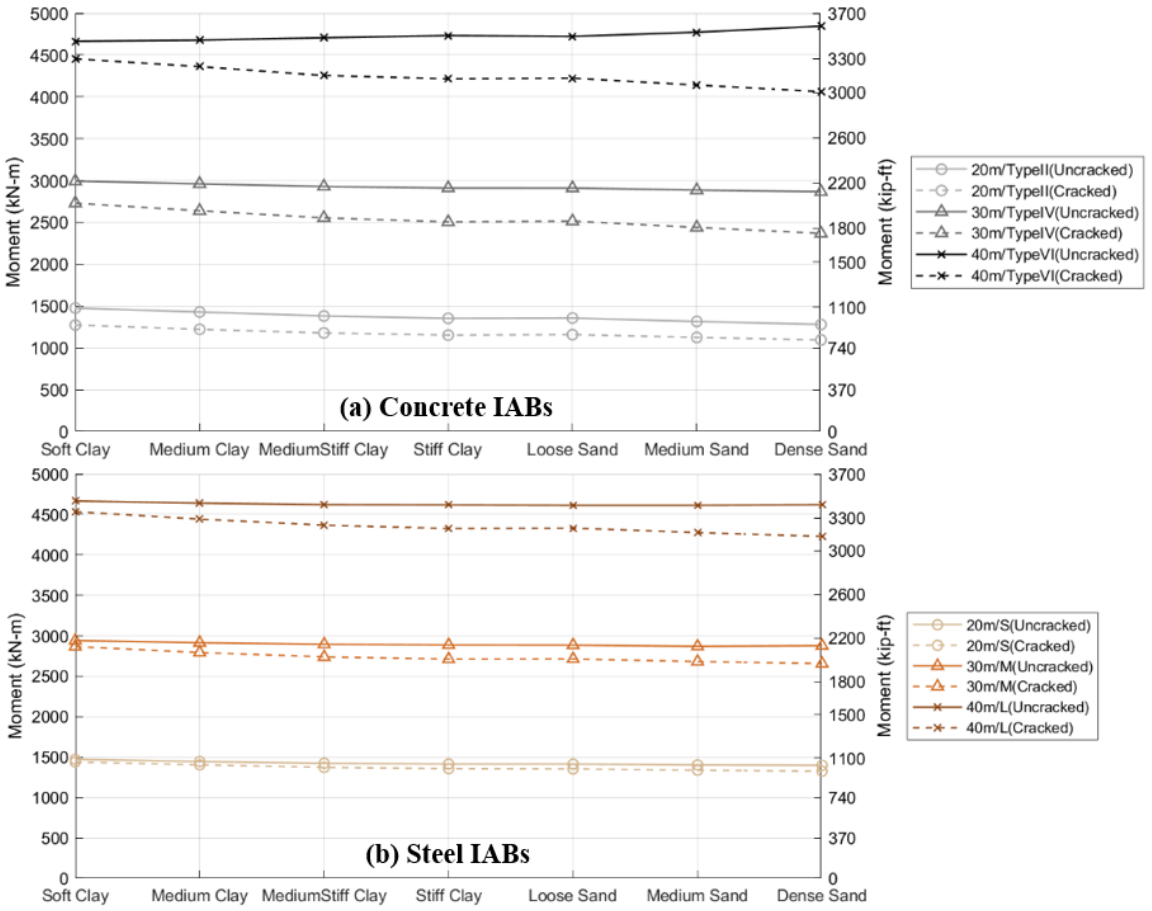

Figure 0.23: Maximum Girder Moment under 1.75L+1.2T(-) Load Combinations for (a)Concrete and (b)Steel Ideal Girder IABs
Note: 1.25D is not included.
IAB parameters: Pile = HP310x125 and Weak Axis Bending

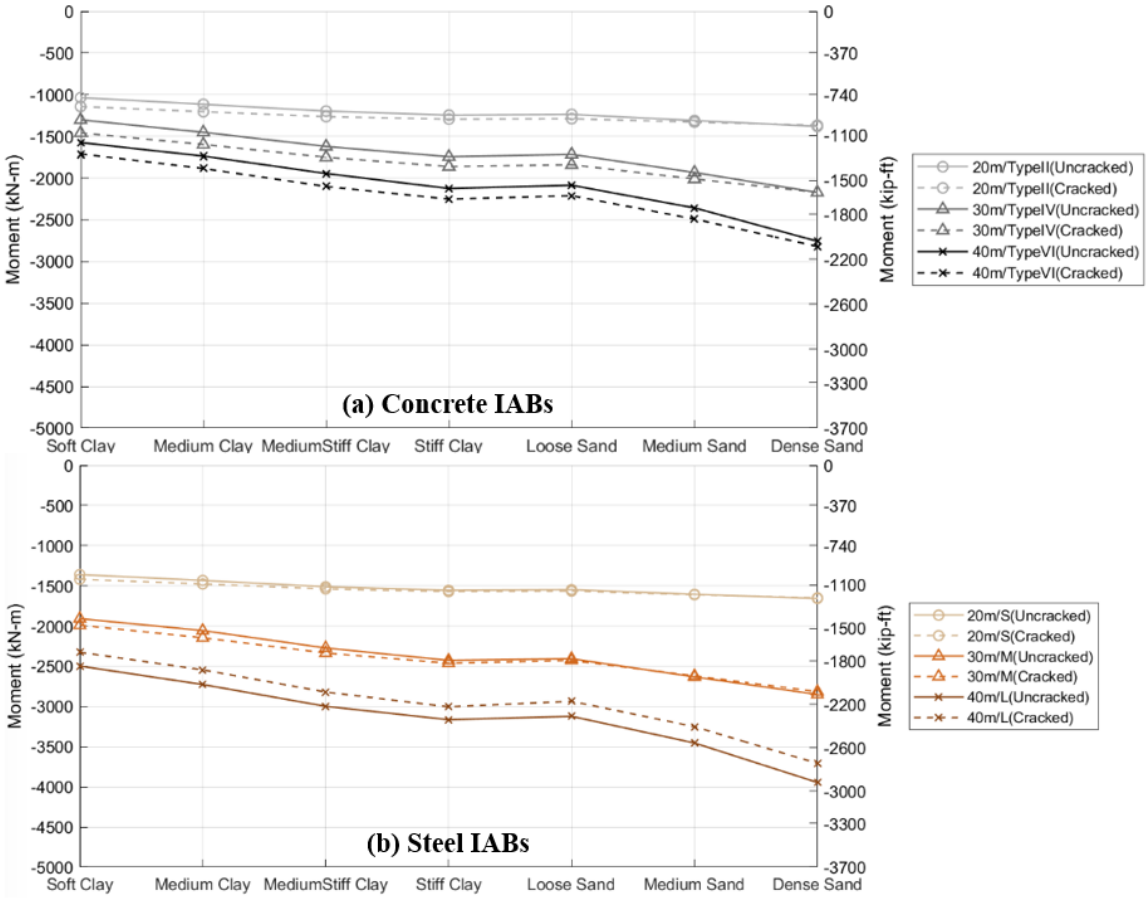

Figure 0.24: Minimum Girder Moment under 1.75L+1.2T(+) Load Combination for (a)Concrete and (b)Steel Ideal Girder IABs

IAB parameters: Pile = HP310x125 and Weak Axis Bending

5.2 Results of Substructure Displacement and Rotation

This section presents the displacement and rotation of the substructure: the abutment and pile. Dead load is not included due to the assumption made for the construction of IABs in this section, specifically that dead load would only induce axial load on the piles. The p-Δ effects were neglected due to the substructure displacement is small even under combined loads. The displacement of the substructure was critical at location of left exterior pile indicated by the dashed line in Figure 0.7 for all FEMs created in this study, thus the results presented in this section were the displacement and rotation of nodes along the left exterior pile. For each IAB, the minimum and maximum results were plotted for load combinations that include live load, as an envelope solution of all truck positions. Typical substructure displacements under Strength 1 load combinations for 40m ideal concrete and steel girder IABs are shown in Figure 0.25 and 5.24. 20m and 30m span ideal girder IABs resulted in similar substructure displacements with the values scaled down. The negative and positive values of displacements indicate the expansion and contraction of the bridge, respectively. The results showed that the load combination of live and positive temperature loads (1.75L+1.2T(+)) resulted in a greater absolute value of overall displacement of the substructure, which was also the critical load combination for the end-span superstructure moment and pile moment in most IABs analyzed in this study. The effect of each parameter (soil stiffness, span length and girder sizes, concrete cracking, and pile geometries) will be evaluated in the following sections.

Figure 0.27 and 5.26 present typical substructure rotations under Strength 1 load combinations for 40m ideal concrete and steel girder IABs. The rotation of the

substructure is consistent along the depth of abutments, as the abutment moves as a rigid body. The results showed that the greatest rotation was observed under the combination of live and positive thermal loads (1.75L+1.2T(+)) along the pile. In the opposite direction, negative thermal load (1.2T(-)) was the controlling load combination at about the same depth. The load combination of live and negative thermal loads (1.75L+1.2T(-)) resulted in the largest rotation of the abutment; the top of abutment moved towards the center of the bridge and the bottom of the abutment moved away from the center of the bridge. 1.75L+1.2T(-) was the smoothest curve throughout the depth of substructure. The rotation of the substructure is also closely related to the pile moment since the moment is associated with maximum curvature, and the curvature is defined as the rate of change in rotation. Thus, the results of substructure rotation are further discussed in the results of pile moment in the next section.

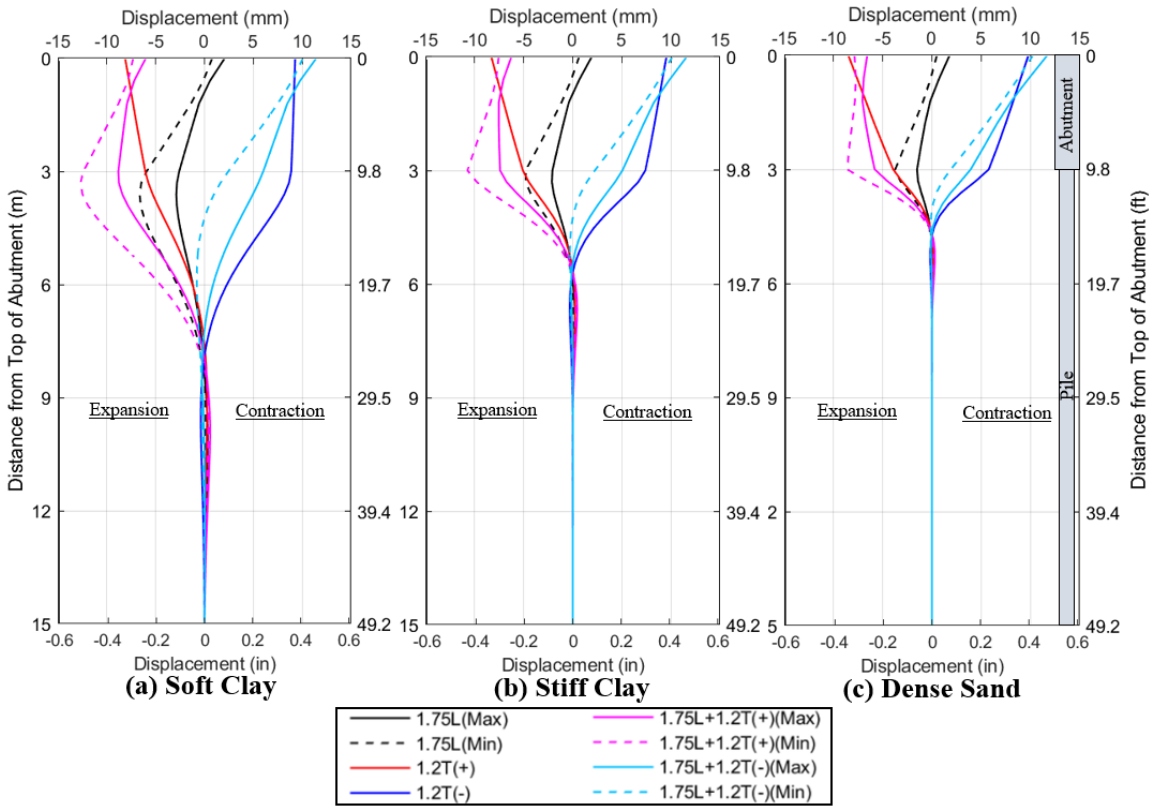

Figure 0.25: Substructure Displacement under Strength 1 Load Combinations for 40m IABs with AASHTO Type VI on (a)Soft Clay and (b)Stiff Clay, and (c) Dense Sand

IAB parameters: Span Length = 40m, Girder = AASHTO Type VI, and Pile = HP310x125 and Weak Axis Bending

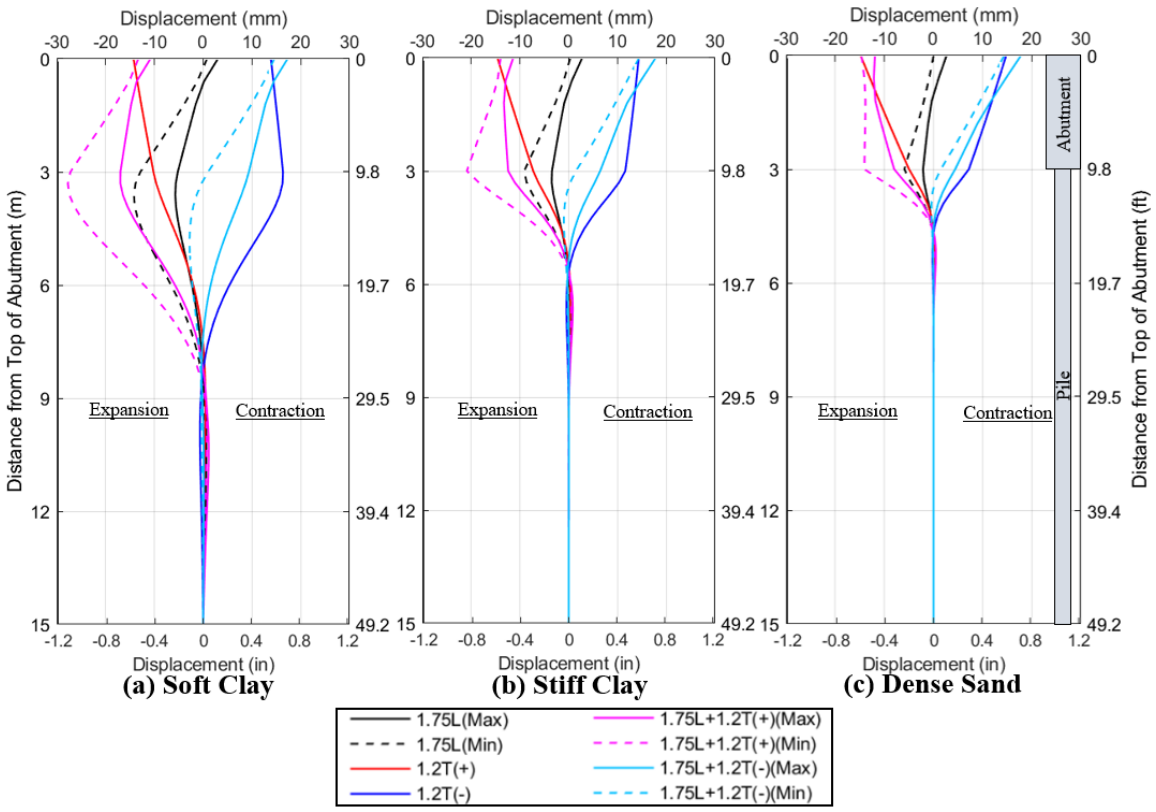

Figure 0.26: Substructure Displacement under Strength 1 Load Combinations for 40m IABs with Large Steel Girders on (a)Soft Clay and (b)Stiff Clay, and (c) Dense Sand

IAB parameters: Span Length = 40m, Girder = Large Steel, and Pile = HP310x125 and Weak Axis Bending

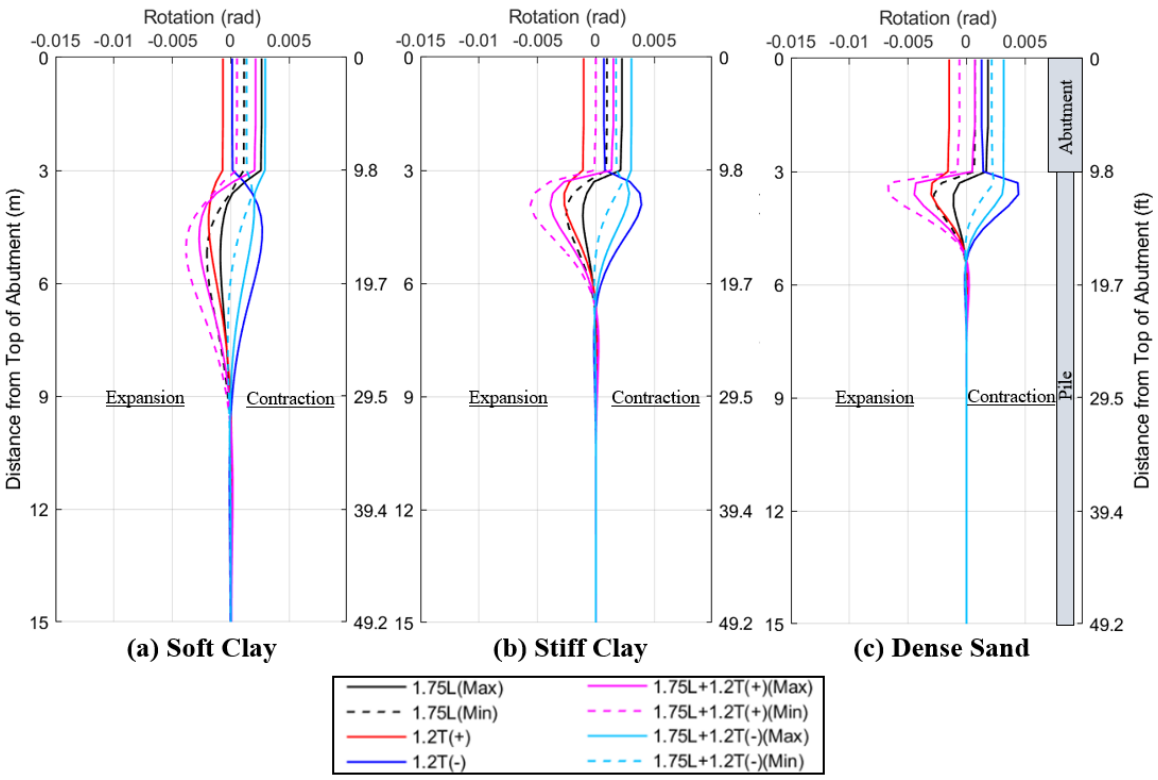

Figure 0.27: Substructure Rotation under Strength 1 Load Combinations for 40m IABs with AASHTO Type VI on (a)Soft Clay and (b)Stiff Clay, and (c) Dense Sand

IAB parameters: Span Length = 40m, Girder = AASHTO Type VI, and Pile = HP310x125 and Weak Axis Bending

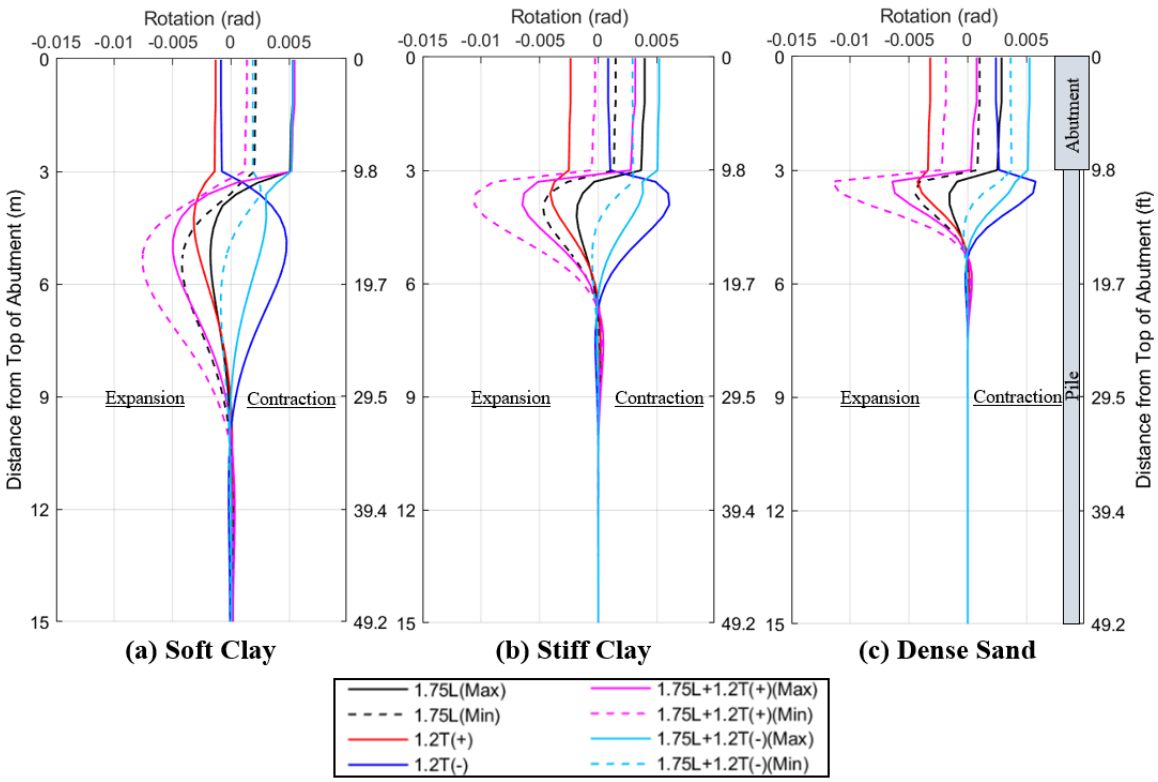

Figure 0.28: Substructure Rotation under Strength 1 Load Combinations for 40m IABs with Large Steel Girders on (a)Soft Clay and (b)Stiff Clay, and (c) Dense Sand
IAB parameters: Span Length = 40m, Girder = Large Steel, and Pile = HP310x125 and Weak Axis Bending

5.2.1 Effect of Soil Stiffness

The effect of soil stiffness on substructures displacement of IABs was analyzed by plotting the results for the same bridge with varying foundation soil. As an example, the substructure displacement for 40m ideal concrete and steel IABs with varying foundation soil under the load combination of 1.75L+1.2T(+) are shown in Figure 0.29. The results showed that the overall displacement of the substructure increased, and the substructure displaced at a deeper depth as the foundation soil became softer. The results also showed that the rotation of the abutment (top 3m (9.8ft) of the substructure) also decreases as the substructure stiffens, as was observed in Figure 0.27 and 5.26. They

indicate that the stiffer foundation soil limits the movement of substructure and rotation of abutment, and thus, it stiffens the substructure of the IAB. Regardless of any IABs under any loads and load combinations, IABs with a stiffer foundation soil had smaller substructure displacements. However, the results showed that the transition from the abutment to the pile in the curve became sharper as the foundation soil became stiffer, causing the pile to return to the zero displacement at shallower depth. This kinking in the pile at the top of piles is a location of high moment in all piles.

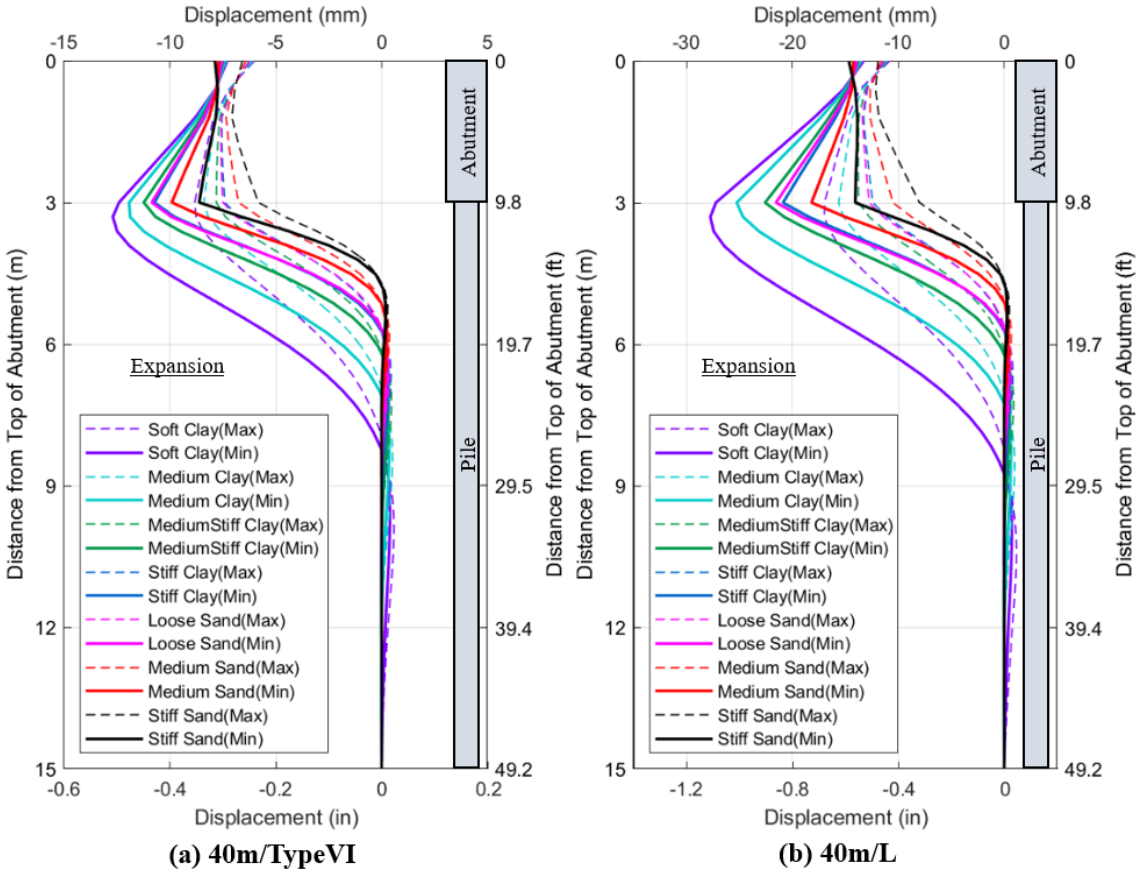

Figure 0.29: Substructure Displacement under 1.75L+1.2T(+) for 40m Ideal (a)Concrete and (b)Steel Girder IABs Varying Soil Condition

Note: IAB parameters: Piles = HP310x125 and Weak Axis Bending

Figure 0.30 and Figure 0.31 show the substructure displacement for 40m ideal concrete steel IABs with varying foundation soil under the contraction load cases, 1.2T(-) and 1.75L+1.2T(-). A greater displacement of pile was observed for 1.2T(-) at the top of pile, and a greater displacement of abutment was observed for 1.75L+1.2T(-) at the top of abutment. As similarly observed in the case of the thermal expansion, the displacement of the overall substructure was greater with softer foundation soil under the thermal contraction. However, the rotation of the abutment slightly increased as the foundation soil stiffened in the case of the thermal contraction. The stiffer foundation caused the pile to return to the zero displacement at shallower depth, which resulted in a greater rotation of abutment under thermal contraction.

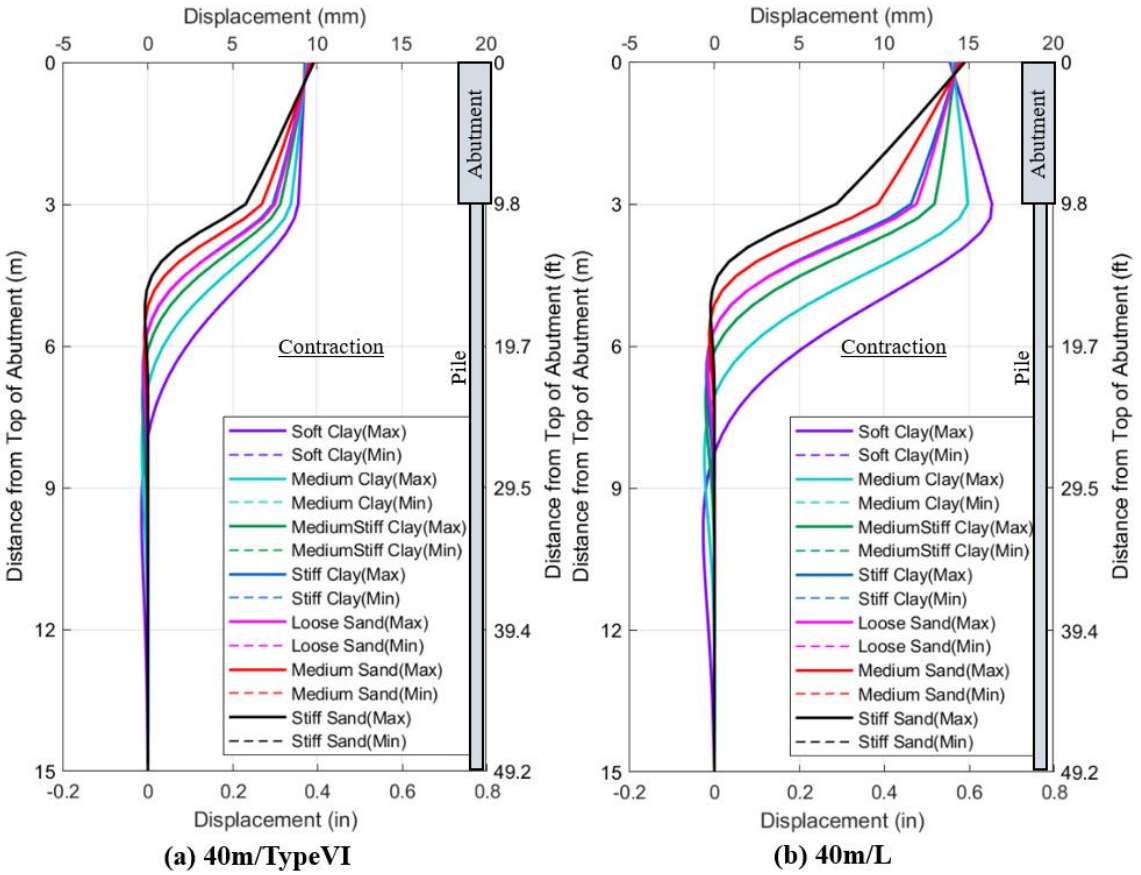

Figure 0.30: Substructure Displacement under 1.2T(-) for 40m Ideal (a)Concrete and (b)Steel Girder IABs Varying Soil Condition

IAB parameters: Piles = HP310x125 and Weak Axis Bending

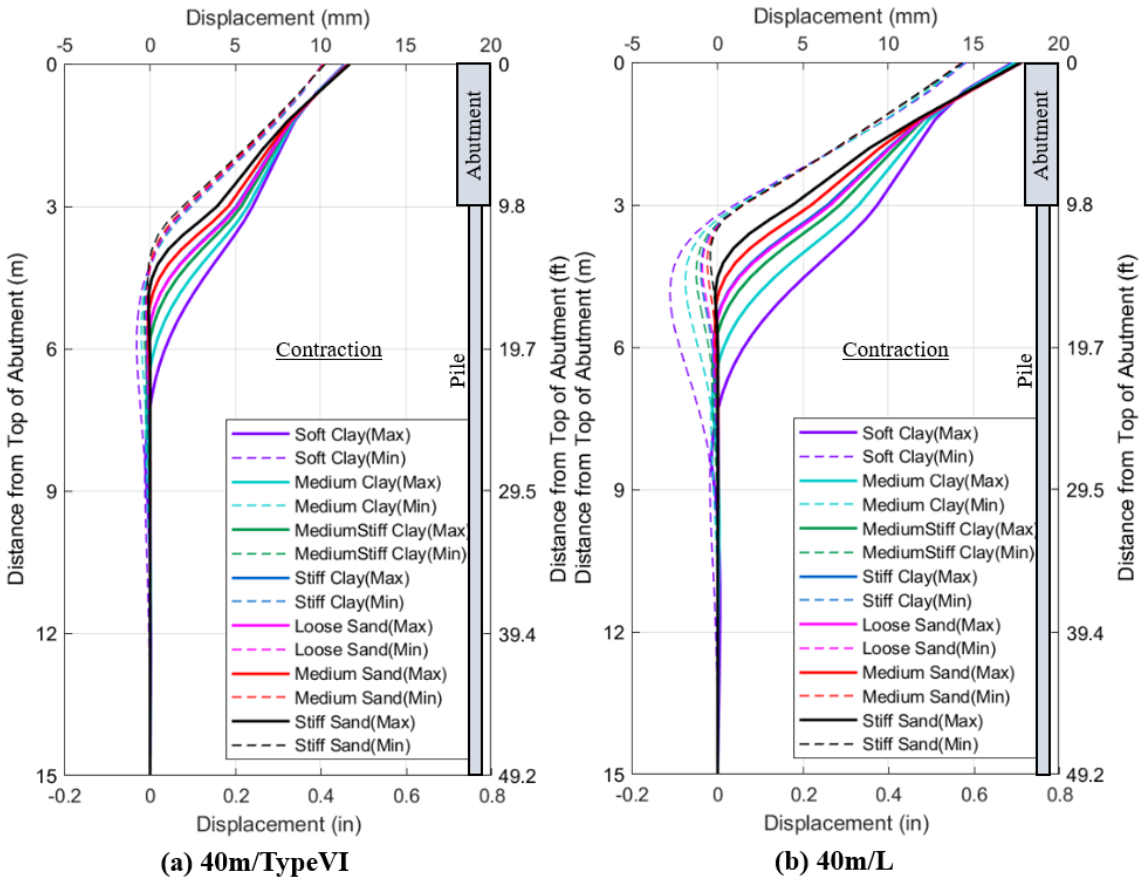

Figure 0.31: Substructure Displacement under 1.75L+1.2T(-) for 40m Ideal (a)Concrete and (b)Steel Girder IABs Varying Soil Condition
IAB parameters: Piles = HP310x125 and Weak Axis Bending

5.2.2 Effect of Span Length and Girder Sizes

The effect of span length was analyzed by plotting the results of IABs with varying span lengths under the critical Strength 1 load combination that resulted in the largest displacement of substructure (1.75L+1.2T(+)). As an example, IABs with AASHTO Type VI and large steel girders built on soft clay with varying span lengths are presented in Figure 0.32. These girders are not ideal size for shorter span IABs, but they

were plotted to analyze the effect of the relative stiffness of superstructure to substructure.

The results showed that greater displacement and rotation of the abutment were observed as the span length increased. The effects from each individual load case are greater for IABs with longer span, and thus, longer span IABs result in a larger displacement of the substructure. This behavior was typical in all IABs, regardless of other bridge geometries.

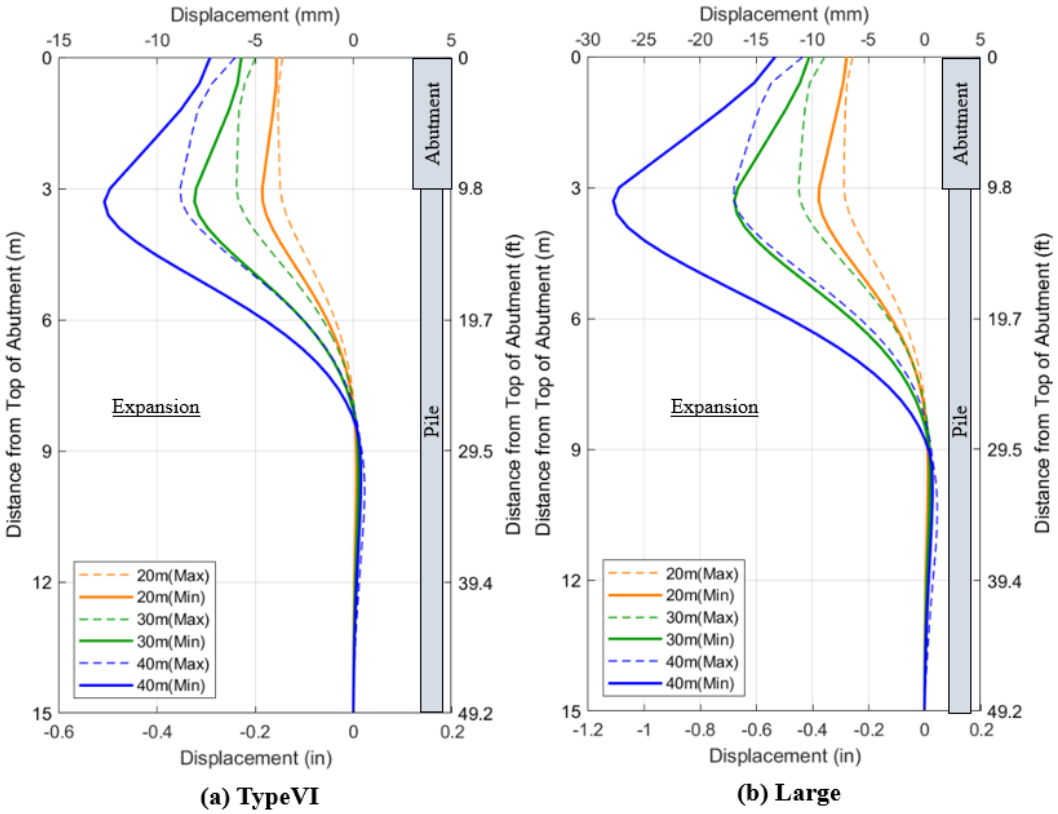

Figure 0.32: Substructure Displacement under 1.75L+1.2T(+) for 20m, 30m, and 40m IABs on Soft Clay with (a) AASHTO Type VI and (b) Large Steel Girders
IAB parameters: Piles = HP310x125 and Weak Axis Bending, Foundation Soil = Soft Clay

The effect of girder sizes was also analyzed by plotting the results of the same span length of IABs with the varying girder sizes. Figure 0.33 to Figure 0.36 show the substructure displacement of IABs on the softest foundation soil (soft clay) and stiffest soil (dense sand) with varying girder sizes under factored live load (1.75L) and positive temperature change (1.2T(+)). For all IABs, the substructure displacement increased with smaller girders (smaller moment of inertia of deck) under the live load, as shown in Figure 0.33 and Figure 0.34. As the moment of inertia of the deck decreased in the order of small steel, Type II, medium steel, large steel, Type IV, and Type VI (presented in Table 0.6), a larger displacement was observed. This indicates that the substructure displaces more as the superstructure becomes more flexible. However, under the thermal load shown in Figure 0.35 and Figure 0.36, the displacement of substructure decreased with smaller girders. The flexible superstructure with smaller girder sizes reduced the fixity of superstructure and substructure. This allowed the abutment to rotate more freely, and the substructure returned to zero displacements at shallower depth due to the soil. This relationship resulted in a smaller displacement of substructure with smaller girder size under the thermal load. The results also showed that steel IABs generally resulted in a larger substructure displacement. Since the thermal coefficient of steel is larger than concrete and a larger temperature change being applied on steel girder IABs, the effect of thermal loads on steel IABs is generally more significant. Similar observation was made for thermal contraction of the bridges (1.2T(-)) shown in Figure 0.37 as an example; the displacement of substructure generally decreased with smaller girders, but the substructure moved towards the center of bridge. However, the combination of live and

negative thermal loads is not critical since the substructure moves away from the center of bridge under live load and towards the center of bridge negative thermal load.

Since the behavior is opposite between live and thermal loads, it became difficult to predict the trend when these loads were combined. Figure 0.38 and Figure 0.39 show the displacement results under the combination of live load and positive temperature change for IABs on soft clay and dense sand (1.75L+1.2T(+)). The results showed that when live and positive thermal loads were combined, the displacement was larger with smaller girders in soft clay (Figure 0.38), however, the displacement was smaller with smaller girders in dense sand (Figure 0.39). This indicates that live load dominated in softer soil and thermal load dominated in stiffer soil.

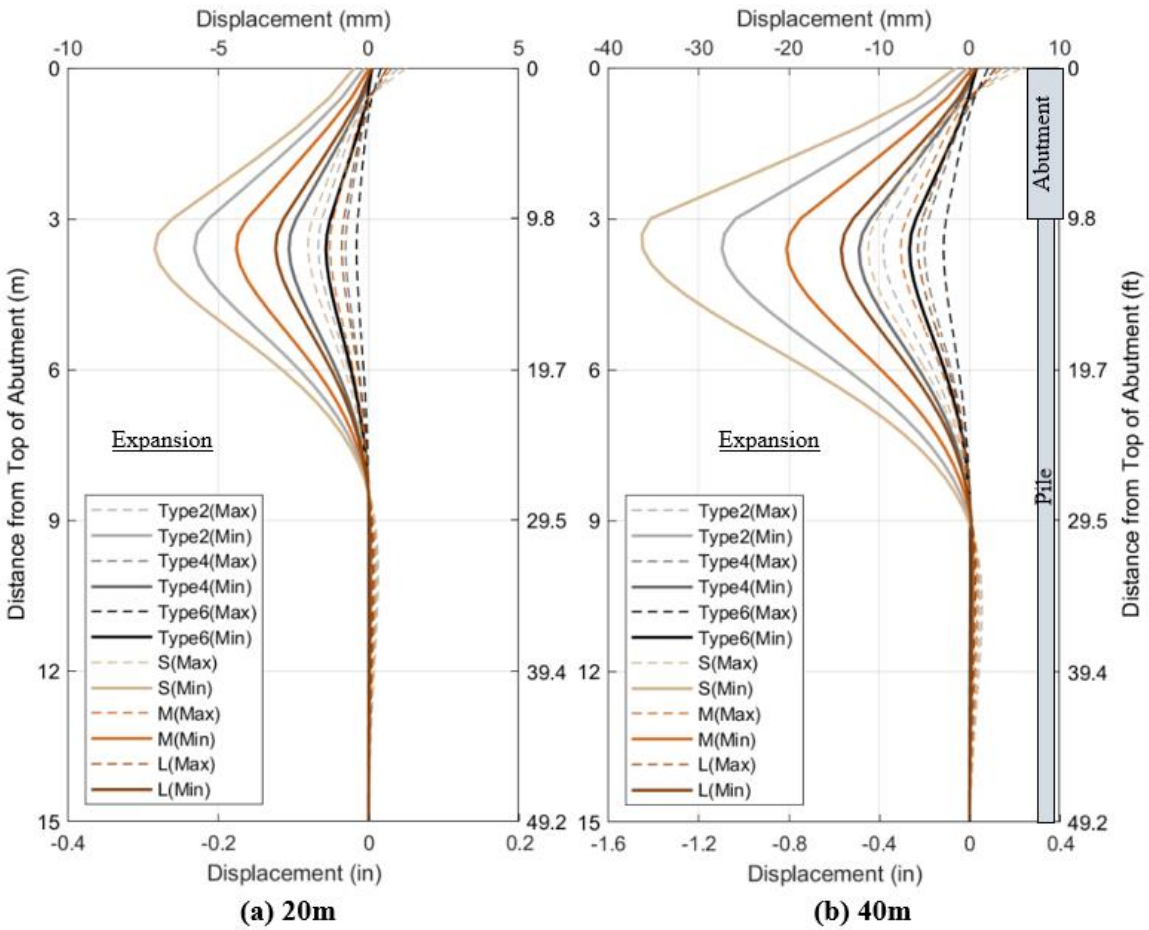

Figure 0.33: Substructure Displacement under Factored Live Load (1.75L) for (a)20m and (b)40m IABs on Soft Clay with Varying Girder Sizes

IAB parameters: Piles = HP310x125 and Weak Axis Bending, Foundation Soil = Soft Clay

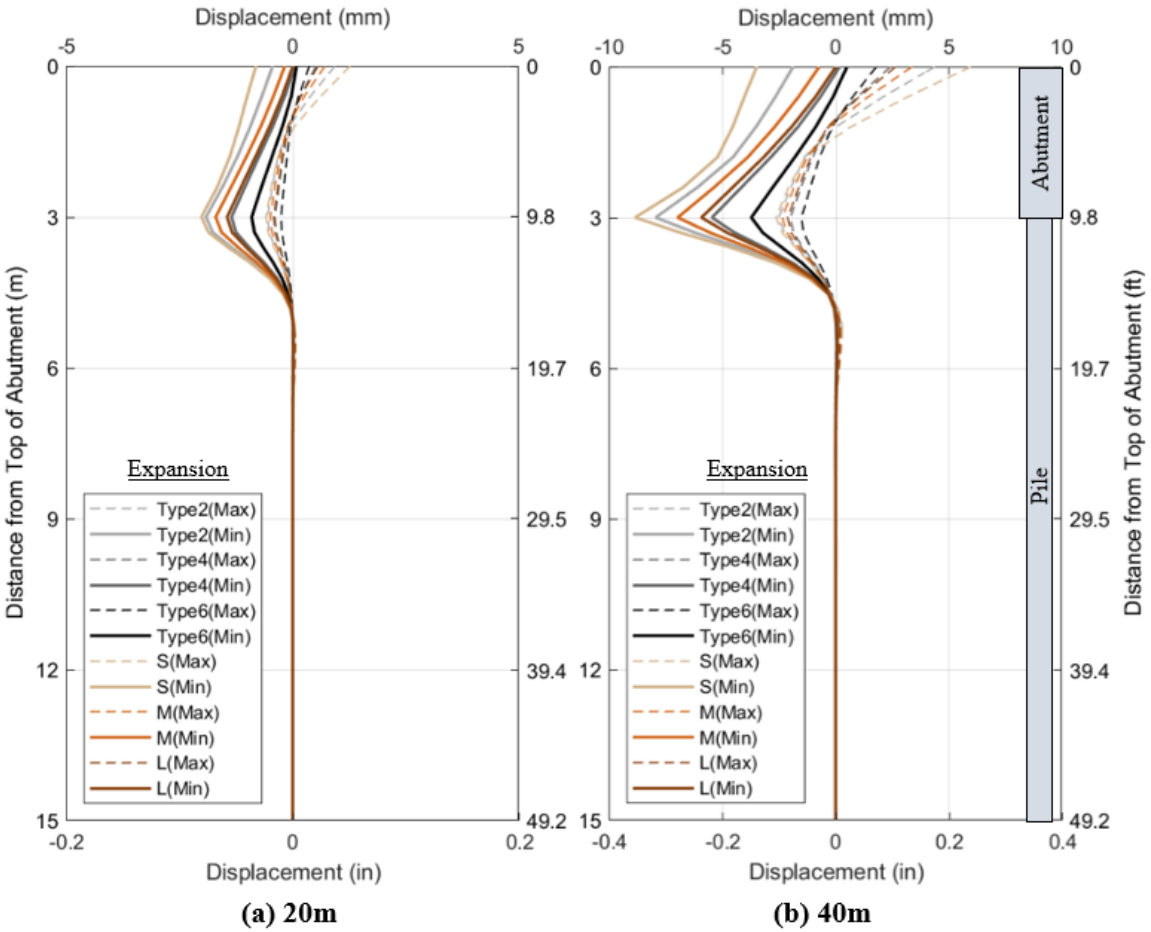

Figure 0.34: Substructure Displacement under Factored Live Load (1.75L) for (a)20m and (b)40m IABs on Dense Sand with Varying Girder Sizes

IAB parameters: Piles = HP310x125 and Weak Axis Bending, Foundation Soil = Dense Sand

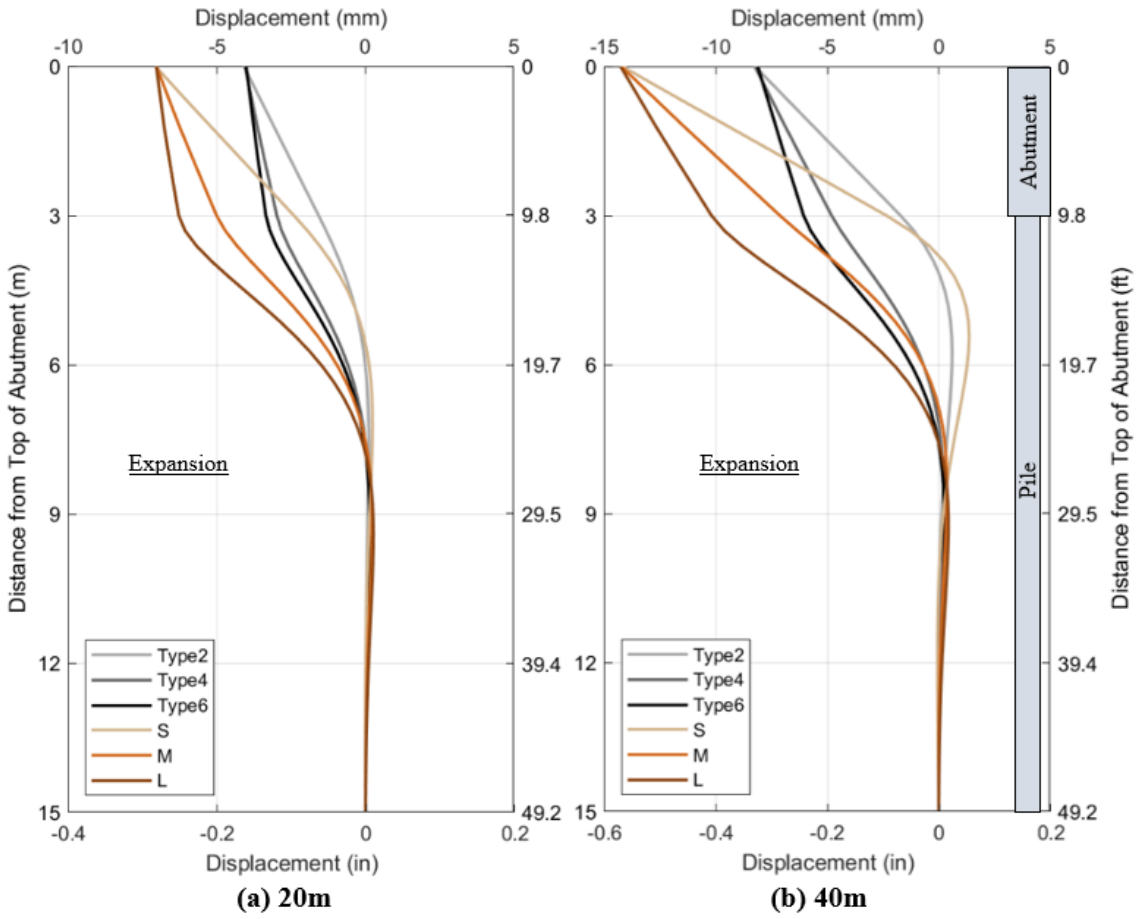

Figure 0.35: Substructure Displacement under Factored Positive Temperature Change (1.2T(+)) for (a)20m and (b)40m IABs on Soft Clay with Varying Girder Sizes
IAB parameters: Piles = HP310x125 and Weak Axis Bending, Foundation Soil = Soft Clay

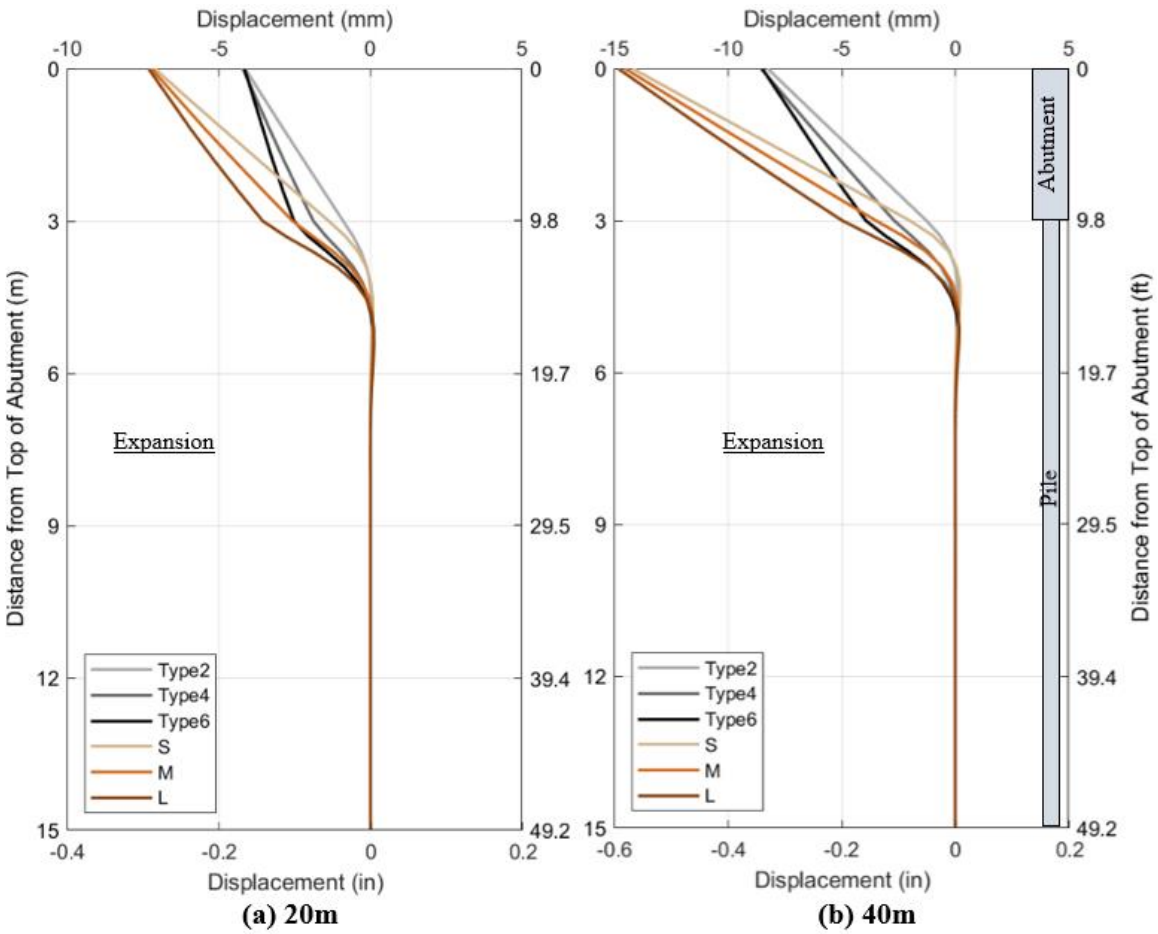

Figure 0.36: Substructure Displacement under Factored Positive Temperature Change (1.2T(+)) for (a)20m and (b)40m IABs on Dense Sand with Varying Girder Sizes
IAB parameters: Piles = HP310x125 and Weak Axis Bending, Foundation Soil = Dense Sand

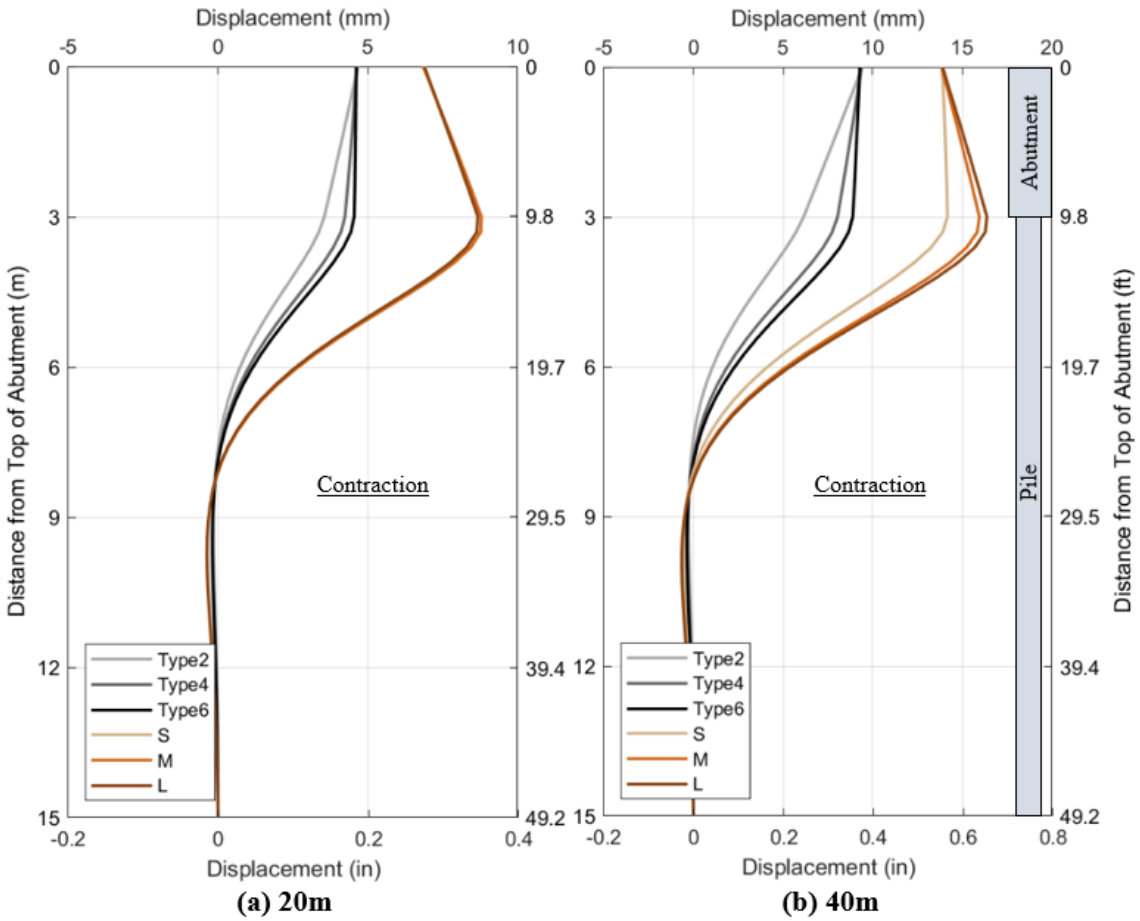

Figure 0.37: Substructure Displacement under Factored Negative Temperature Change (1.2T(-)) for (a)20m and (b)40m IABs on Soft Clay with Varying Girder Sizes
IAB parameters: Piles = HP310x125 and Weak Axis Bending, Foundation Soil = Soft Clay

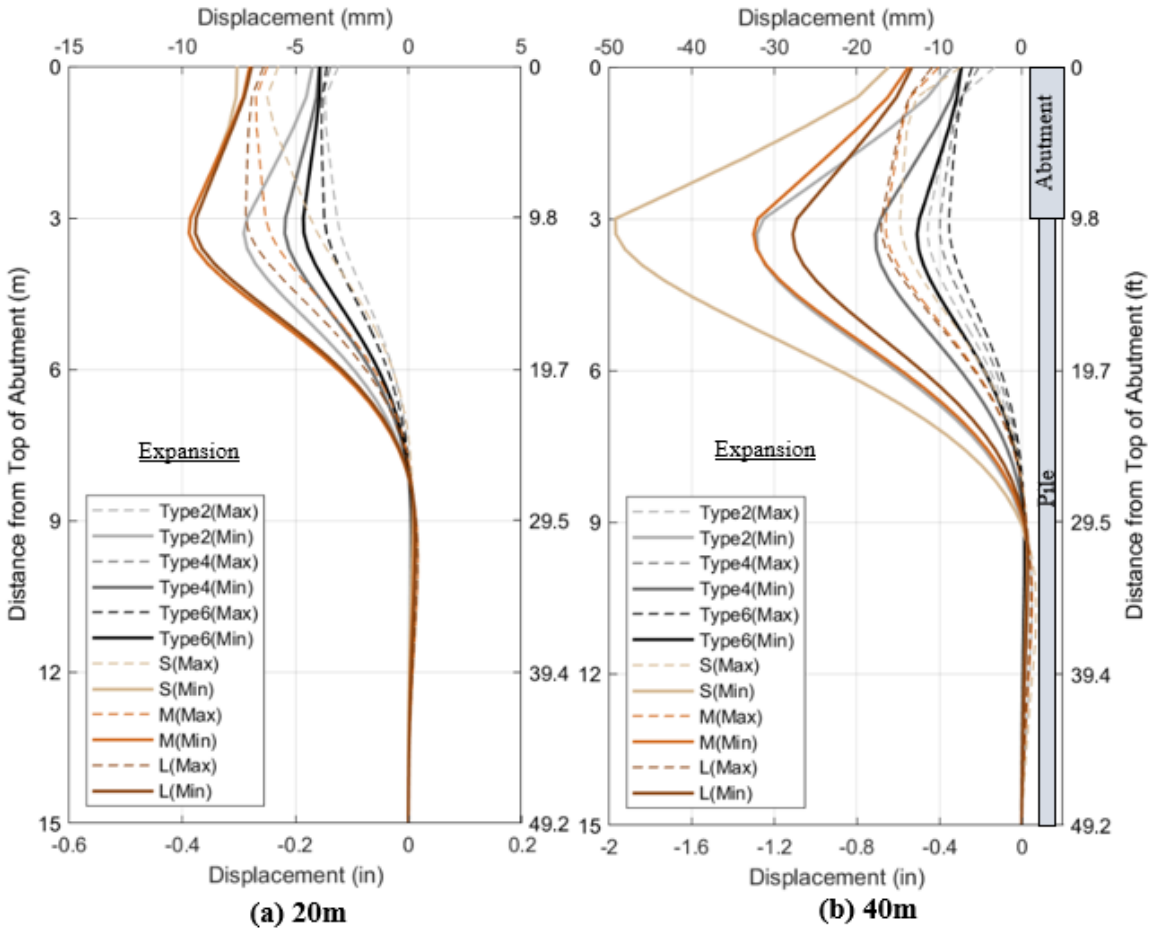

Figure 0.38: Substructure Displacement under 1.75L+1.2T(+) for (a)20m and (b)40m IABs on Soft Clay with Varying Girder Size

IAB parameters: Piles = HP310x125 and Weak Axis Bending, Foundation Soil = Soft Clay

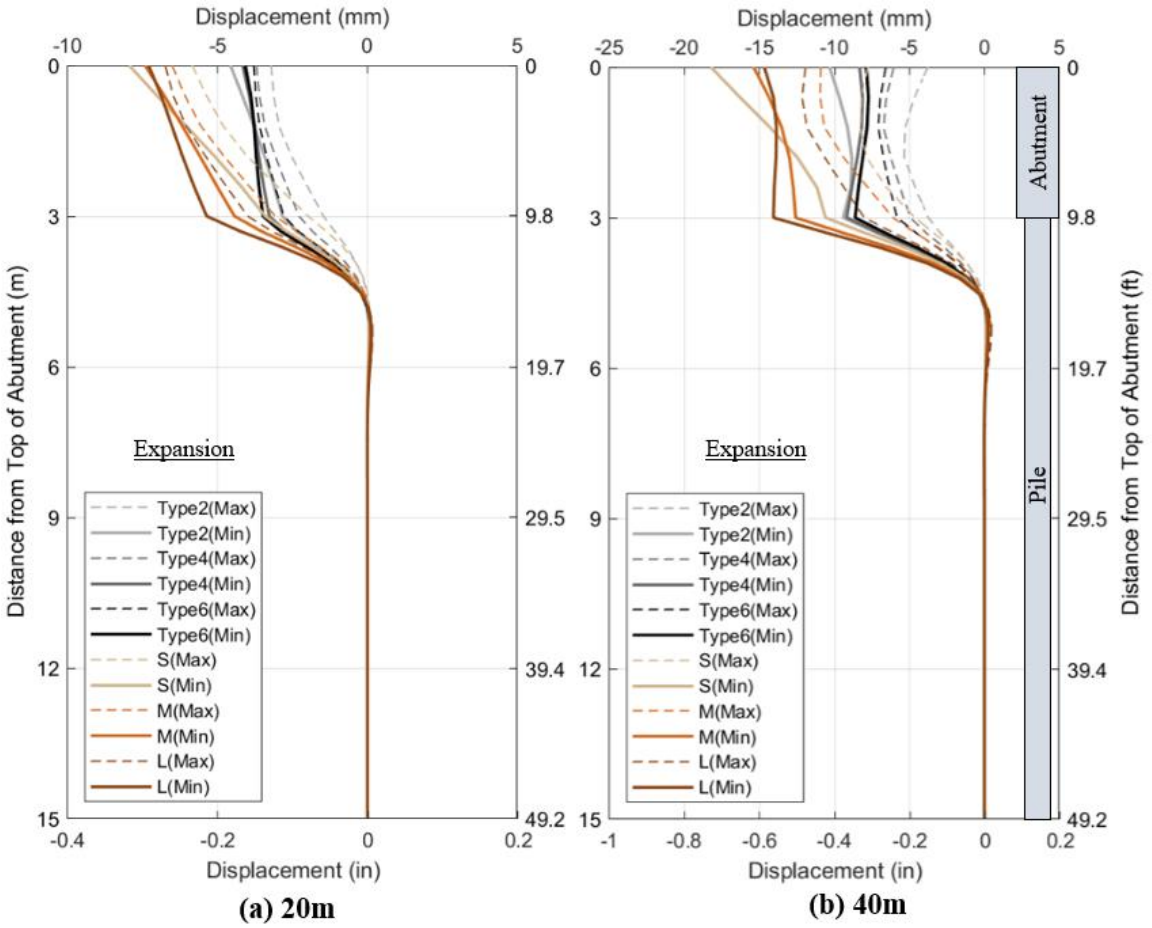

Figure 0.39: Substructure Displacement under 1.75L+1.2T(+) for (a)20m and (b)40m IABs on Dense Sand with Varying Girder Size

IAB parameters: Piles = HP310x125 and Weak Axis Bending, Foundation Soil = Dense Sand

5.2.3 Effect of Concrete Crack

The substructure displacement of IABs with cracked and uncracked sections were also compared. As an example, Figure 0.40 and Figure 0.41 show the substructure displacement for 20m and 40m ideal concrete and steel IABs on soft clay and stiff sand under 1.75L+1.2T(+) load combination. As similarly observed in the results of superstructure moment in previous sections, the difference between uncracked and cracked sections is generally more significant for concrete IABs due to girders also being

subjected to cracking; this behavior was observed in all IABs. The cracked sections allowed more rotation of the abutment in all IABs, leading to a greater displacement of the substructure. This is also a similar effect to IABs having smaller girder sizes, as these effects reduce the superstructure stiffness. The results also showed that the effect of concrete cracking decreased as span length decreased or foundation soil became stiffer.

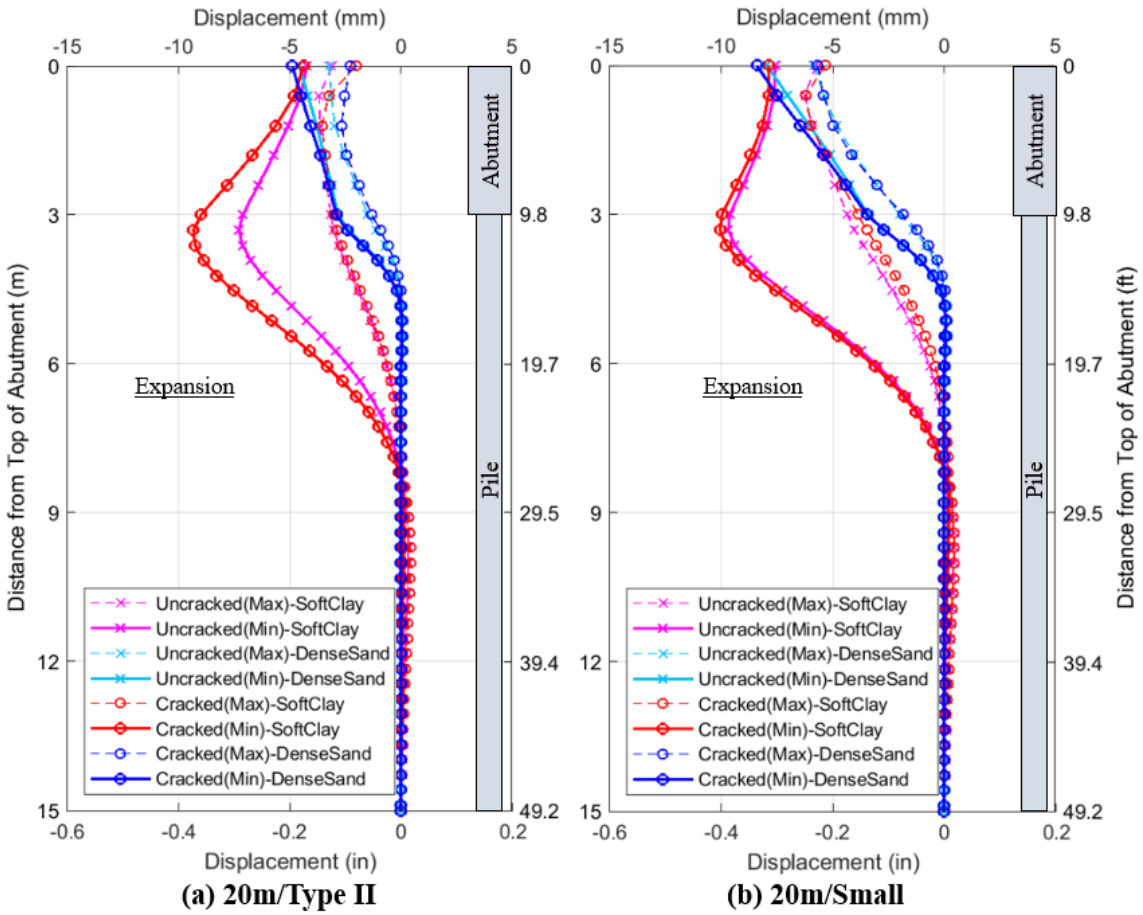

Figure 0.40: Substructure Displacement under 1.75L+1.2T(+) for Uncracked and Cracked 20m (a)Concrete and (b)Steel Ideal Girder IABs
IAB parameters: Girder = (a)AASHTO Type II (b)Small Steel Girder, Piles = HP310x125 and Weak Axis Bending

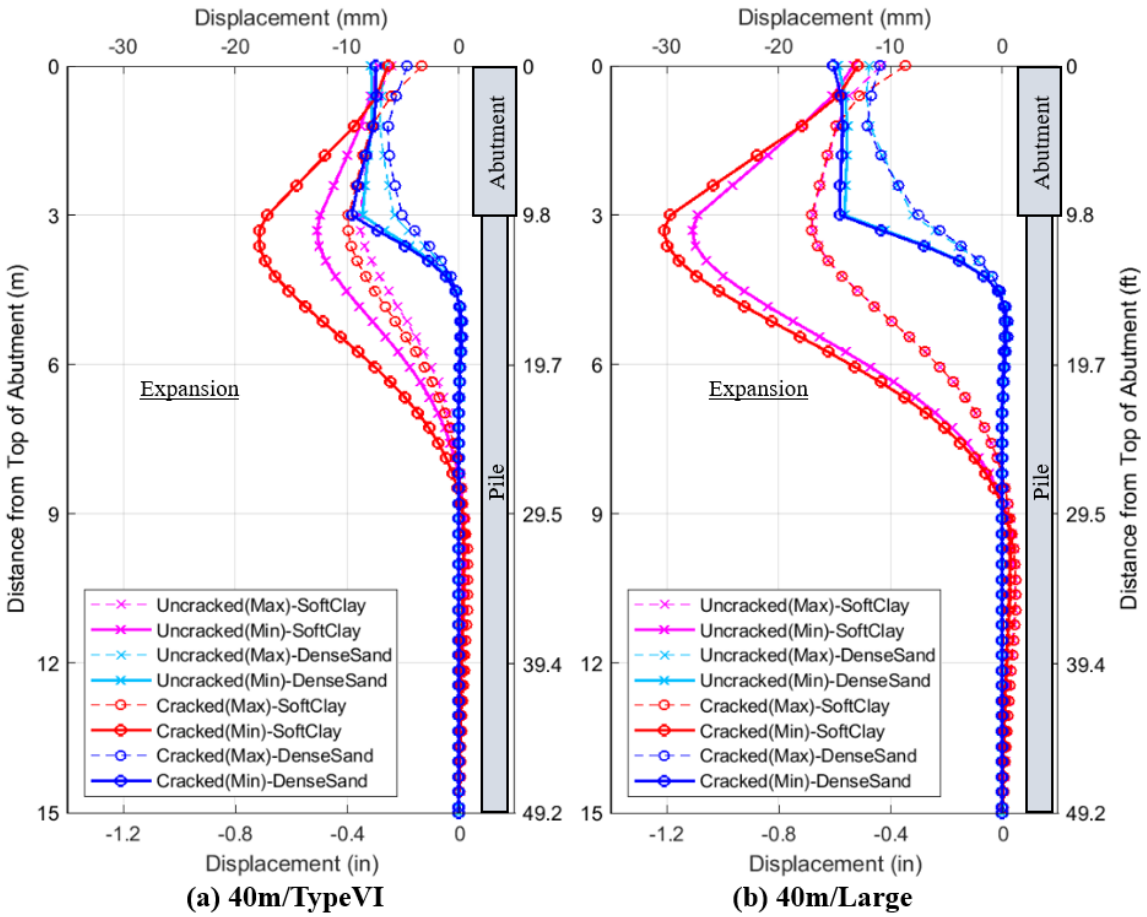

Figure 0.41: Substructure Displacement under 1.75L+1.2T(+) for Uncracked and Cracked 40m (a)Concrete and (b)Steel Ideal Girder IABs

IAB parameters: Girder = (a)AASHTO Type VI (b)Large Steel Girder, Piles = HP310x125 and Weak Axis Bending

5.2.4 Effect of Pile Size and Orientation

The effects of pile size and orientation were analyzed in this section. The substructure becomes stiffer as the pile size increases or the piles are oriented about the strong axis bending. However, overall substructure stiffness also has a significant contribution from the soil resistance. Figure 0.42 and Figure 0.43 show the substructure displacement under 1.75L+1.2T(+) load combination for 20m and 40m concrete and steel ideal girder IABs on soft clay and dense sand with varying pile size: HP250x85 and HP310x125. The substructure displacement with the smaller (more flexible) pile displaced slightly more but returned to zero displacement sooner due to the soil resistance on soft clay. This resulted in a sharper transition from the abutment to the piles. The difference between the pile sizes increased as the foundation soil stiffened. In shorter IABs, the difference became less significant. Additionally, under the thermal contraction, the difference is negligible even in longer span IABs, as shown in Figure 0.44.

Similar observation was made with the change of pile orientation. Figure 0.45 shows the results of 40m IABs with varying pile orientation under 1.75L+1.2T(+) load combination. The substructure displaced more at shallower depth in IABs with weak-axis orientation, but it returned to the zero displacement at shallower depth due to the soil resistance. However, the difference made in the substructure displacements from the change of pile size or pile orientation is less significant than the change of foundation soil stiffness. This indicates the substructure stiffness is contributed more by the soil stiffness rather than pile geometries.

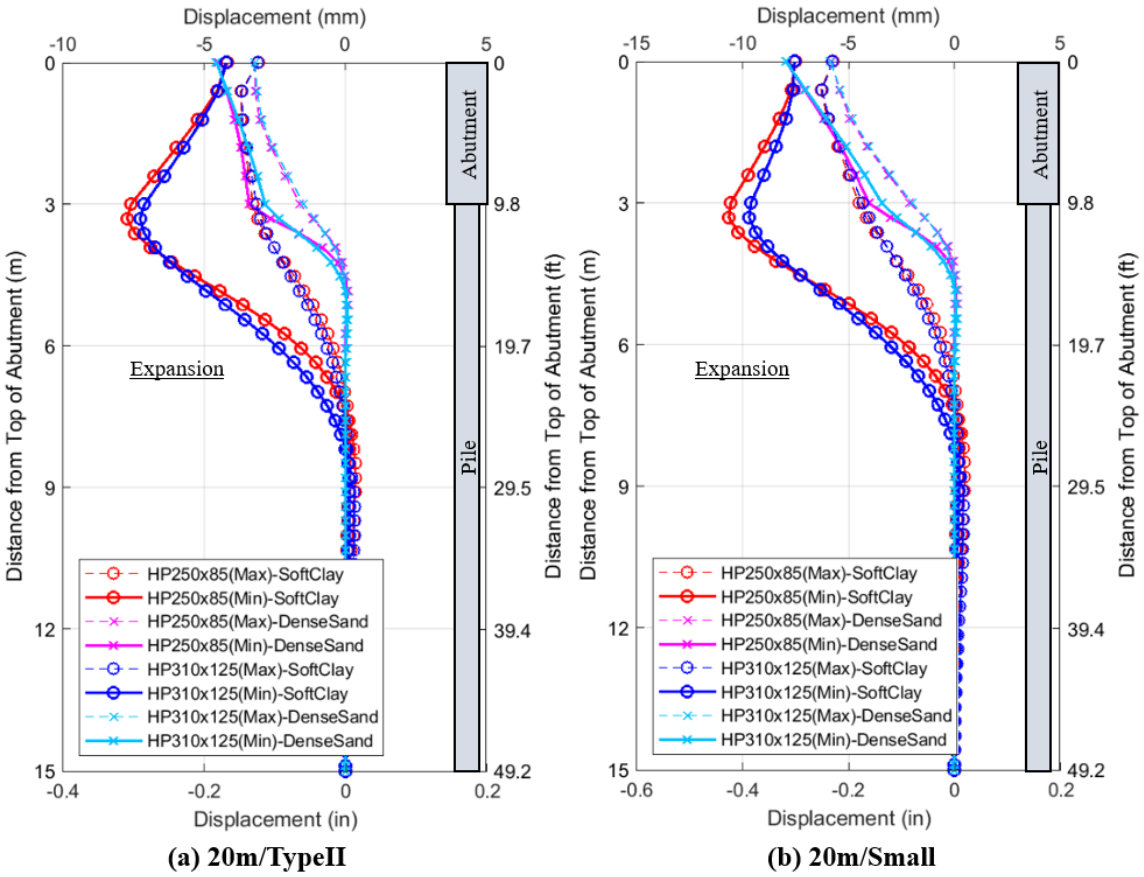

Figure 0.42: Substructure Displacement under 1.75L+1.2T(+) for 20m (a)Concrete and (b)Steel Ideal Girder IABs with Varying Pile Size

Note: IAB parameters: Girder = (a)AASHTO Type VI (b)Large Steel Girder, Piles = Weak Axis Bending

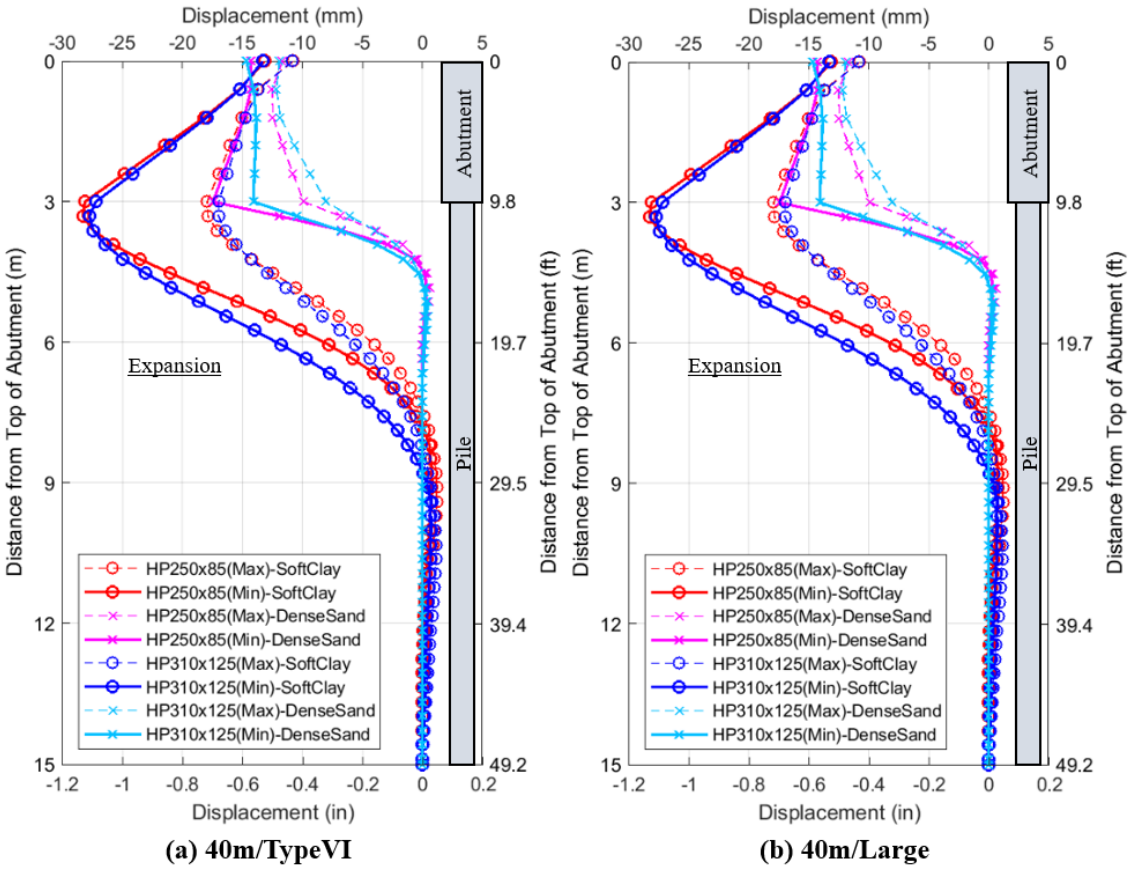

Figure 0.43: Substructure Displacement under 1.75L+1.2T(+) for 40m (a)Concrete and (b)Steel Ideal Girder IABs with Varying Pile Size

Note: IAB parameters: Girder = (a)AASHTO Type VI (b)Large Steel Girder, Piles = Weak Axis Bending

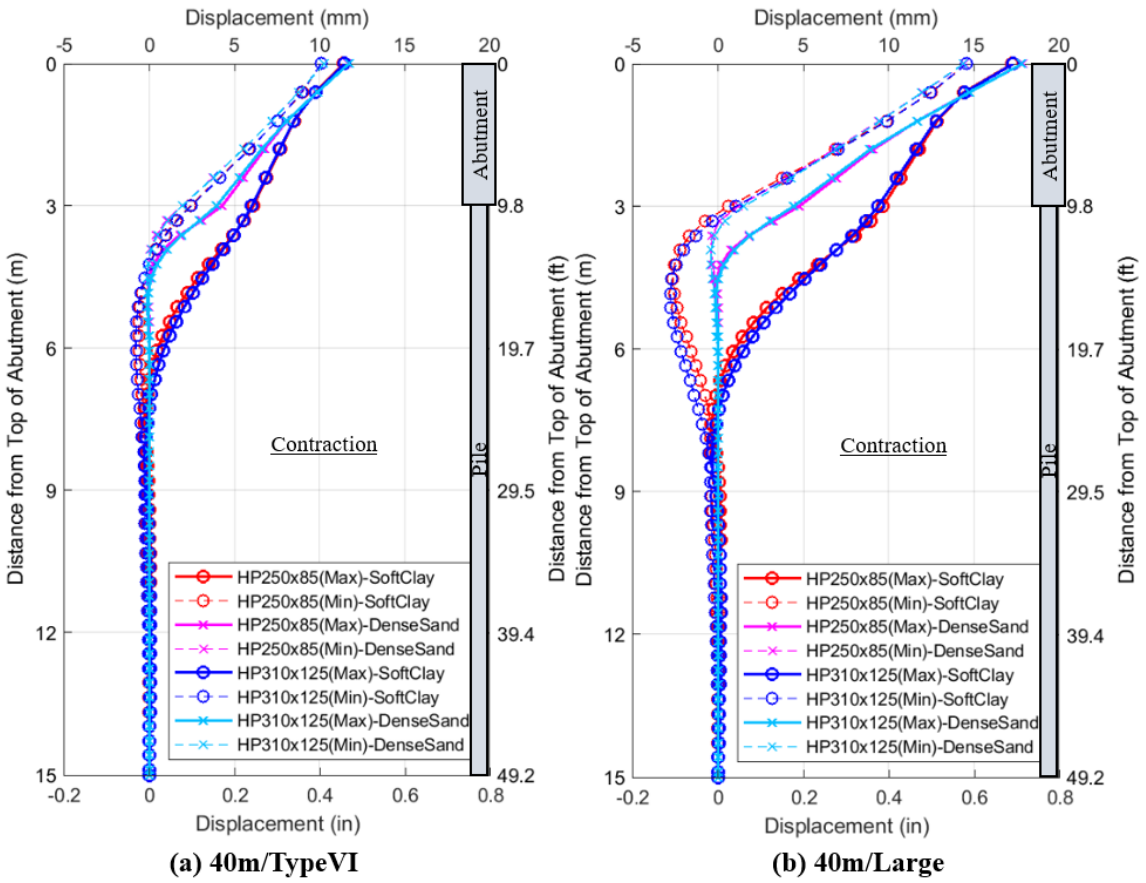

Figure 0.44: Substructure Displacement under 1.75L+1.2T(-) for 40m (a)Concrete and (b)Steel Ideal Girder IABs with Varying Pile Size

Note: IAB parameters: Girder = (a)AASHTO Type VI (b)Large Steel Girder, Piles = Weak Axis Bending

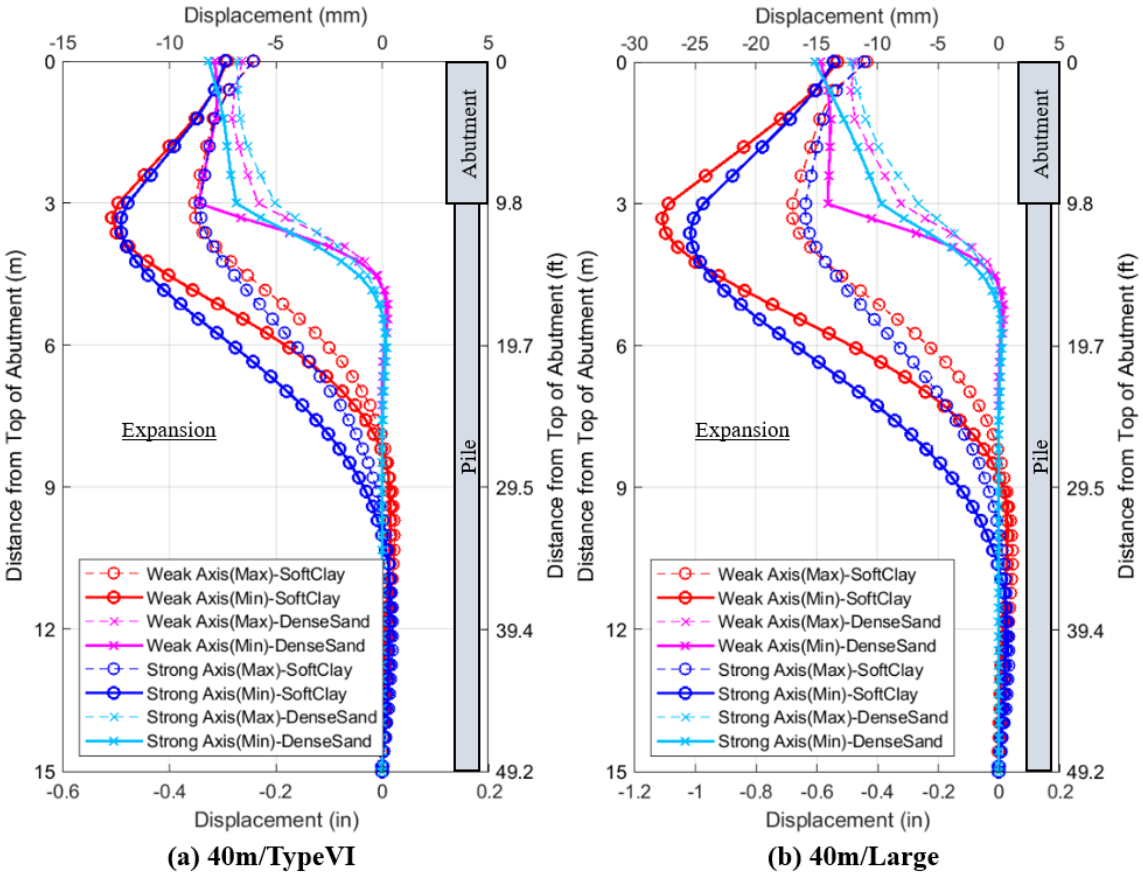

Figure 0.45: Substructure Displacement under 1.75L+1.2T(+) for 40m (a)Concrete and (b)Steel Ideal Girder IABs with Varying Pile Orientation

Note: IAB parameters: Girder = (a)AASHTO Type VI (b)Large Steel Girder, Piles = HP310x125

5.3 Results of Pile Bending Moment

This section presents the results of pile bending moment. Dead load does not influence the results due to the assumption made for the construction of IABs in this study. The plastic hinges were also included in all IABs presented in this section. The yield and plastic capacities of piles considered in this study included the axial load in the piles, thus, they were reduced from the nominal capacities of the piles, as described in Section 2.3. Some IABs yielded the piles, but the pile moment never reached the reduced

or nominal plastic moment capacity ($M_{p\_reduced}$ or $M_{p\_nominal}$) of the pile in all IABs. The reduced and nominal yield and plastic capacities are listed in Table 0.7.

Each abutment was supported by four piles for all IABs, and the maximum moment of each pile was recorded. Under the thermal loads, the results of the two right and two left piles at each abutment are symmetrical about the center of the deck width, and the moment is distributed equally among four piles, as presented in Table 0.6. When the bridges were analyzed under all possible Strength 1 load combinations, the results showed that the left exterior pile always became the critical pile, as highlighted in Table 0.7, thus the maximum pile moment of exterior left pile was compared in the rest of this section.

Table 0.8 present the maximum pile moment under individual Strength 1 load combinations for all ideal IABs. The critical load combination was 1.75L+1.2T(+) for all 30m and 40m IABs, but varied for 20m IABs, as highlighted in the table. The critical load combination for the end-span superstructure moment presented in Section 5.1 was 1.75L+1.2T(+) for all IABs, but the critical load combination for the pile moment was not necessarily 1.75L+1.2T(+) load combination. The results also showed that the pile moment of load combination is not a direct addition of the results of individual load cases due to nonlinearity of models. The results presented in Table 0.6, Table 0.7, and Table 0.8 are limited to IABs with ideal girder and pile sizes on loosest and stiffest foundation soils. However, these results are typical for all other IABs studied, and the effect of other parameters will be presented in the following sections.

Table 0.6: Maximum Exterior and Interior Pile Moments for Ideal IABs under Thermal Loads

Bridge Dimension				Maximum Pile Moment (kN-m)			
				T(+)		T(-)	
Span Length (m)	Girder Size	Pile Size	Foundation Soil	Exterior Pile	Interior Pile	Exterior Pile	Interior Pile
20	Type II	HP250x85	Soft Clay	2.1	2.1	13.7	13.8
20	Type II	HP250x85	Dense Sand	7.6	7.7	20.4	20.9
20	S	HP250x85	Soft Clay	4.1	4.1	46.1	46.1
20	S	HP250x85	Dense Sand	13.0	13.1	48.3	48.9
30	Type IV	HP310x125	Soft Clay	16.5	16.6	36.8	37.0
30	Type IV	HP310x125	Dense Sand	46.5	47.4	82.2	83.2
30	M	HP310x125	Soft Clay	20.2	20.5	83.4	83.5
30	M	HP310x125	Dense Sand	35.0	35.3	106.3	107.5
40	Type VI	HP310x125	Soft Clay	30.5	30.6	55.6	55.7
40	Type VI	HP310x125	Dense Sand	104.4	105.5	154.6	155.1
40	L	HP310x125	Soft Clay	45.1	45.4	102.7	102.8
40	L	HP310x125	Dense Sand	82.8	84.6	157.4	158.1

Note: Results are limited for uncracked IABs with piles oriented about the weak axis.

Table 0.7: Maximum Absolute Moment of Individual Piles for Ideal IABs under Critical Strength 1 Load Combination

Bridge Dimension				Maximum Pile Moment (kN-m)				Critical Load Combination
Span Length (m)	Girder Size	Pile Size	Foundation Soil	Left Exterior	Left Interior	Right Exterior	Right Interior	
20	Type II	HP250x85	Soft Clay	50.4	49.5	47.7	46.1	1.75L+1.2T(+)
20	Type II	HP250x85	Dense Sand	91.1	89.3	85.3	81.2	1.75L+1.2T(+)
20	S	HP250x85	Soft Clay	61.4	60.5	58.8	57.1	1.75L+1.2T(+)
20	S	HP250x85	Dense Sand	92.8	90.4	86.0	81.8	1.75L
30	Type IV	HP310x125	Soft Clay	101.6	99.9	96.3	92.9	1.75L+1.2T(+)
30	Type IV	HP310x125	Dense Sand	194.1	191.8	183.8	175.3	1.75L+1.2T(+)
30	M	HP310x125	Soft Clay	149.3	147.4	144.4	142.1	1.75L+1.2T(+)
30	M	HP310x125	Dense Sand	205.5	202.4	196.4	188.2	1.75L+1.2T(+)
40	Type VI	HP310x125	Soft Clay	118.8	116.7	112.3	108.1	1.75L+1.2T(+)
40	Type VI	HP310x125	Dense Sand	233.6	231.2	225.5	220.1	1.75L+1.2T(+)
40	L	HP310x125	Soft Clay	193.3	191.4	187.5	184.1	1.75L+1.2T(+)
40	L	HP310x125	Dense Sand	255.0	253.0	249.8	246.7	1.75L+1.2T(+)

Note: Results are limited for uncracked IABs with piles oriented about the weak axis. Highlighted cell is the critical pile moment for that bridge.

HP250x85(Weak Axis): $M_{y\_reduced}$ = 78.3kN-m and $M_{p\_reduced}$ = 166.0kN-m

HP310x125(Weak Axis): $M_{y\_reduced}$ = 136.3kN-m and $M_{p\_reduced}$ = 289.1kN-m

Table 0.8: Maximum Pile Moment for Ideal IABs under Individual Strength 1 Load Combinations

Bridge Dimension					Maximum Pile Moment (kN-m)					Figure
Span Length (m)	**Girder Size**	**Pile Size**	**Soil**	**Concrete Crack**	**1.75L**	**1.2T(+)**	**1.2T(-)**	**1.75L+ 1.2T(+)**	**1.75L+ 1.2T(-)**	
20	Type II	HP250x85	Soft Clay	Uncrack	-48.9	2.6	16.5	-50.4	-46.3	Figure 0.46(a)
				Crack	-70.6	6.9	11.7	-66.5	-75.9	Figure 0.47(a)
			Dense Sand	Uncrack	-88.2	9.2	24.6	-91.1	-79.7	Figure 0.46(c)
				Crack	-101.7	11.1	-11.0	-96.1	-105.2	Figure 0.47(c)
	S		Soft Clay	Uncrack	-58.9	4.9	54.3	-61.4	-40.8	Figure 0.48(a)
				Crack	-70.2	11.4	49.3	-64.7	-61.8	
			Dense Sand	Uncrack	-92.8	15.6	58.1	-92.2	-57.5	Figure 0.48(c)
				Crack	-101.0	19.8	40.6	-91.4	-83.4	
30	Type IV	HP310x125	Soft Clay	Uncrack	-82.9	-19.8	44.1	-101.6	-51.2	Figure 0.49(a)
				Crack	-134.9	6.6	34.7	-140.0	-129.3	
			Dense Sand	Uncrack	-161.0	-55.5	98.9	-194.1	-92.3	Figure 0.49(c)
				Crack	-195.0	23.9	40.5	-198.9	-181.8	
	M		Soft Clay	Uncrack	-122.1	-25.8	97.8	-149.3	-63.8	Figure 0.50(a)
				Crack	-145.5	11.9	86.1	-158.5	-119.6	
			Dense Sand	Uncrack	-183.2	42.0	128.1	-205.5	-102.5	Figure 0.50(c)
				Crack	-198.7	44.0	86.7	-205.1	-159.4	
40	Type VI	HP310x125	Soft Clay	Uncrack	-88.4	-37.0	65.0	-118.8	-28.7	Figure 0.51(a)
				Crack	-147.0	-17.0	60.1	-157.8	-125.3	
			Dense Sand	Uncrack	-187.2	-125.4	173.9	-233.6	98.2	Figure 0.51(c)
				Crack	-226.7	-44.0	115.5	-241.3	-188.1	
	L		Soft Clay	Uncrack	-151.5	-55.1	119.6	-193.3	-77.3	Figure 0.52(a)
				Crack	-180.6	-32.8	105.2	-206.1	-144.7	
			Dense Sand	Uncrack	-224.2	-100.9	180.3	-255.0	-131.1	Figure 0.52(c)
				Crack	-239.9	62.5	140.3	-256.8	-198.0	

Note: Results are limited to piles orientated about the weak axis bending. Highlighted cell is the critical pile moment for that bridge.

HP250x85(Weak Axis): $M_{y\_reduced}$ = 78.3kN-m and $M_{p\_reduced}$ = 166.0kN-m

HP310x125(Weak Axis): $M_{y\_reduced}$ = 136.3kN-m and $M_{p\_reduced}$ = 289.1kN-m

Typical pile moment diagrams for IABs with varying span length and girder sizes on soft clay, stiff clay, and dense sand under all possible Strength 1 load combinations are shown in Figure 0.46 to Figure 0.52. For the load combinations that include live loads, the results are recorded as envelopes of moments for all possible truck locations. The maximum absolute value of pile moment for each load combination is indicated with markers in each figure. The figures are limited to IABs with ideal girders and pile sizes on three foundation soil types.

The results of the individual load cases (1.75L, 1.2T(+), or 1.2T(-)) showed that the negative thermal load (1.2T(-)) opposed the live (1.75L) and positive thermal loads (1.2T(+)). The results also showed that the maximum absolute pile moment was usually recorded at the top of pile under live and negative thermal loads, but under positive thermal load, the location of the maximum absolute value of pile moment was recorded either at the top of the pile or at a deeper depth, depending on the bridge; the location tended to be at a deeper depth under thermal loads for shorter IABs in which the effect of thermal load is smaller.

When loads were combined and factored, the critical combination of loads varied. The critical load combination was 1.75L+1.2T(+) consistently in all 30m and 40m IABs with ideal girder sizes or larger girder sizes, but the critical load combination varied for 20m IABs or any length of IABs with the smallest concrete (AASHTO Type II) or steel girders (Small Steel). This indicates that the critical load combination becomes 1.75L+1.2T(+) consistently for bridges with certain relative stiffness of superstructure to substructure and having more influence from the thermal load. For those 20m IABs having 1.75L or 1.75L+1.2T(-) as their critical load combinations, the effects of thermal

loads were minimal; the maximum pile moment under 1.75L+1.2T(+) in those IABs were within 10% to 15% of their critical maximum pile moments.

The pile moment is also related significantly to the substructure displacement and rotation presented in Section 5.2. The results showed that the maximum pile moment is recorded at the depth at which the rate of change in rotation plot is the greatest, as observed from the rotation plot in Figure 0.27 and pile moment diagram in Figure 0.51 for the same IABs. The maximum moment is associated with maximum curvature, and the curvature is defined as the rate of change in rotation, and thus, the pile moment is zero at the depth of the maximum rotation. A sharper transition between the abutment and pile in a displacement plot for the IABs with stiffer foundation soil; this was also related to the increase in pile moment at the top of piles as soil stiffness increases.

The results also showed that the pile moment is significantly smaller than the end-span superstructure moments even after the end-span moment was divided by four piles. This may be caused by the force couple between axial load built up in girders and soil springs. However, an apparent relationship was not determined.

The following sections present the effect of each parameter (foundation soil stiffness, span length and girder size, and pile geometries) on pile moment. Unless otherwise noted, the absolute maximum pile moment at the top of pile under 1.75L+1.2T(+), as this load combination controlled in most IABs, and for other IABs, the differences in the critical pile moment to the results of 1.75L+1.2T(+) was relatively minimal as mentioned earlier.

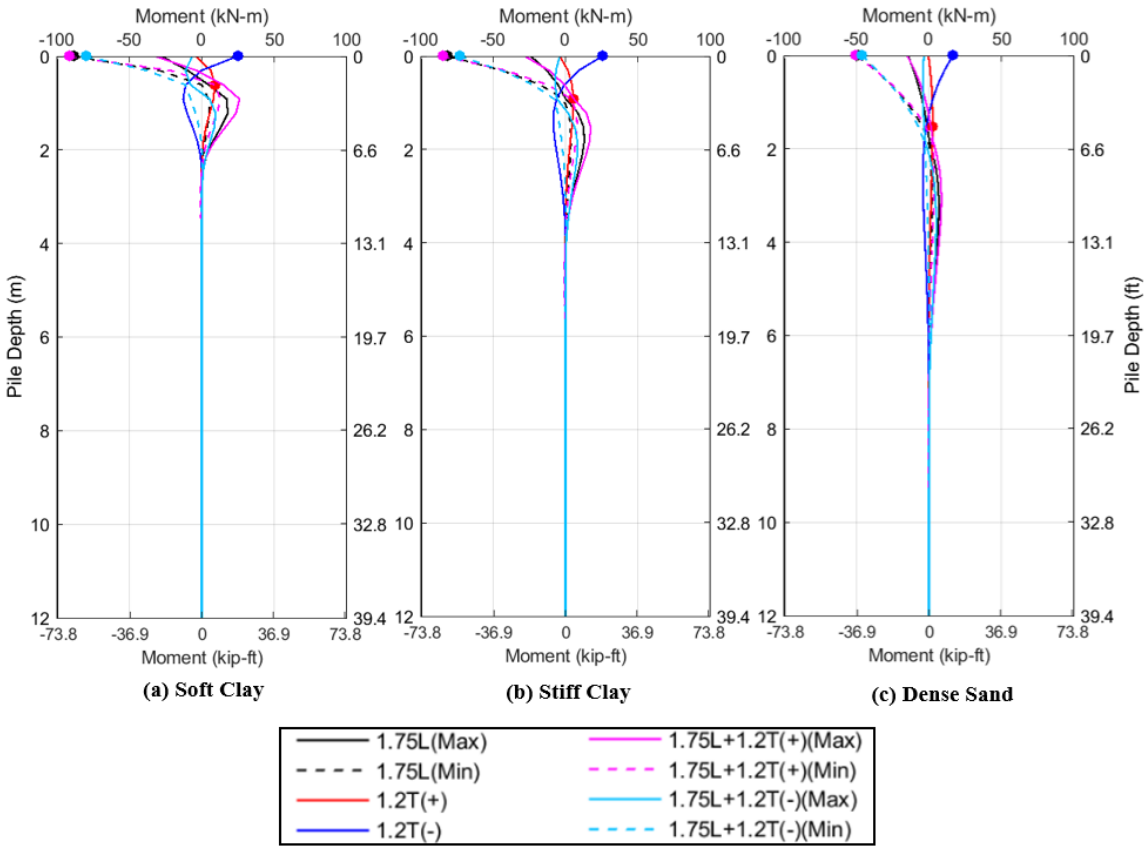

Figure 0.46: Pile Moment Diagram under Strength 1 Load Combinations for Uncracked 20m IABs with AASHTO Type II on (a)Soft Clay, (b)Stiff Clay, and (c)Dense Sand
IAB parameters: Span Length = 20m, Girder = AASHTO Type II, and Pile = HP250x85 and Weak Axis Bending

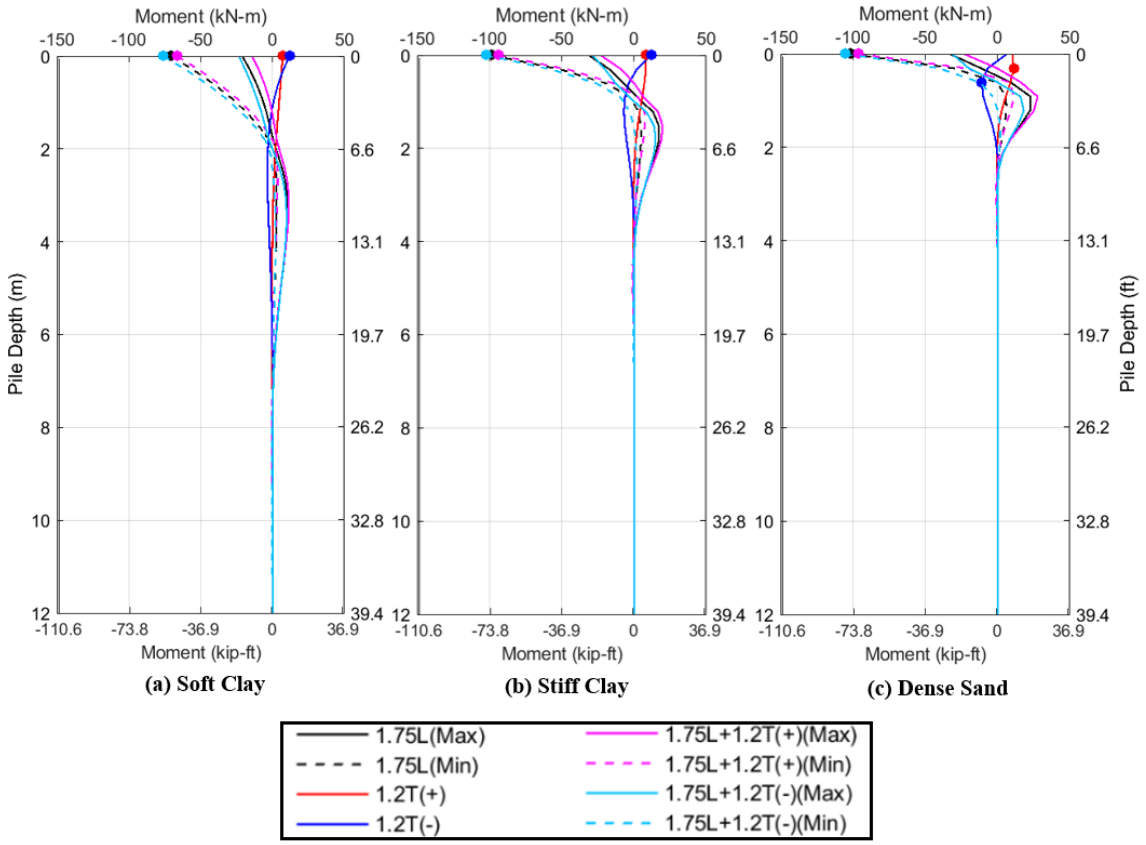

Figure 0.47: Pile Moment Diagram under Strength 1 Load Combinations for Cracked 20m IABs with AASHTO Type II on (a)Soft Clay, (b)Stiff Clay, and (c)Dense Sand

IAB parameters: Span Length = 20m, Girder = AASHTO Type II, and Pile = HP250x85 and Weak Axis Bending

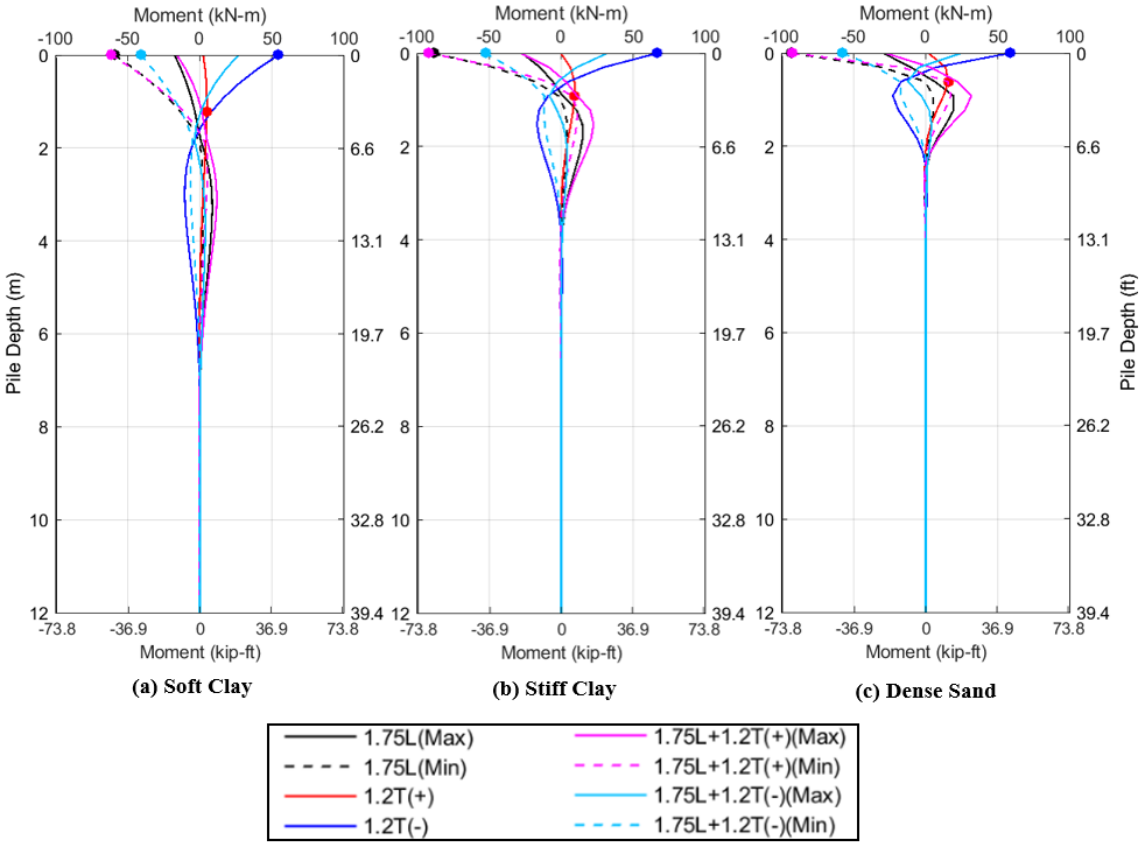

Figure 0.48: Pile Moment Diagram under Strength 1 Load Combinations for Uncracked 20m IABs with Small Steel Girders on (a)Soft Clay, (b)Stiff Clay, and (c)Dense Sand

IAB parameters: Span Length = 20m, Girder = Small Steel, and Pile = HP250x85 and Weak Axis Bending

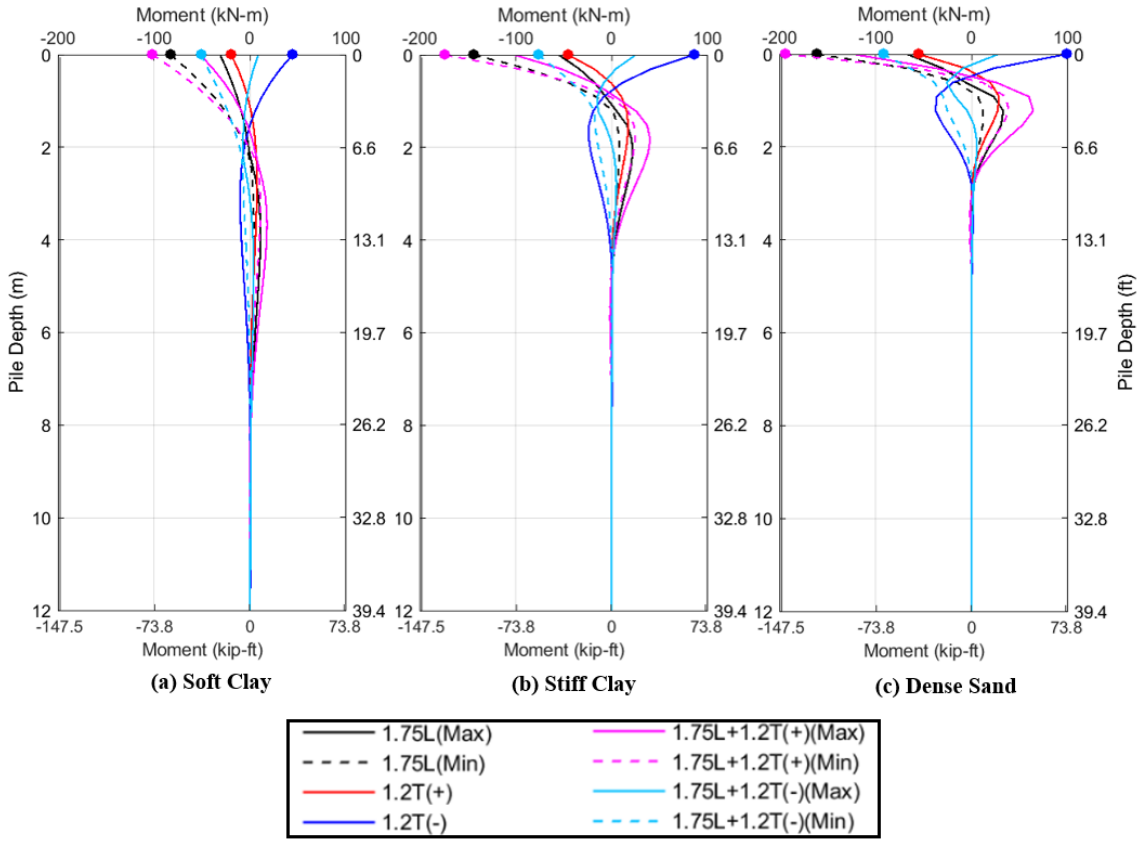

Figure 0.49: Pile Moment Diagram under Strength 1 Load Combinations for Uncracked 30m Concrete IABs on (a)Soft Clay, (b)Stiff Clay, and (c)Dense Sand

IAB parameters: Span Length = 30m, Girder = AASHTO Type IV, and Pile = HP310x125 and Weak Axis Bending

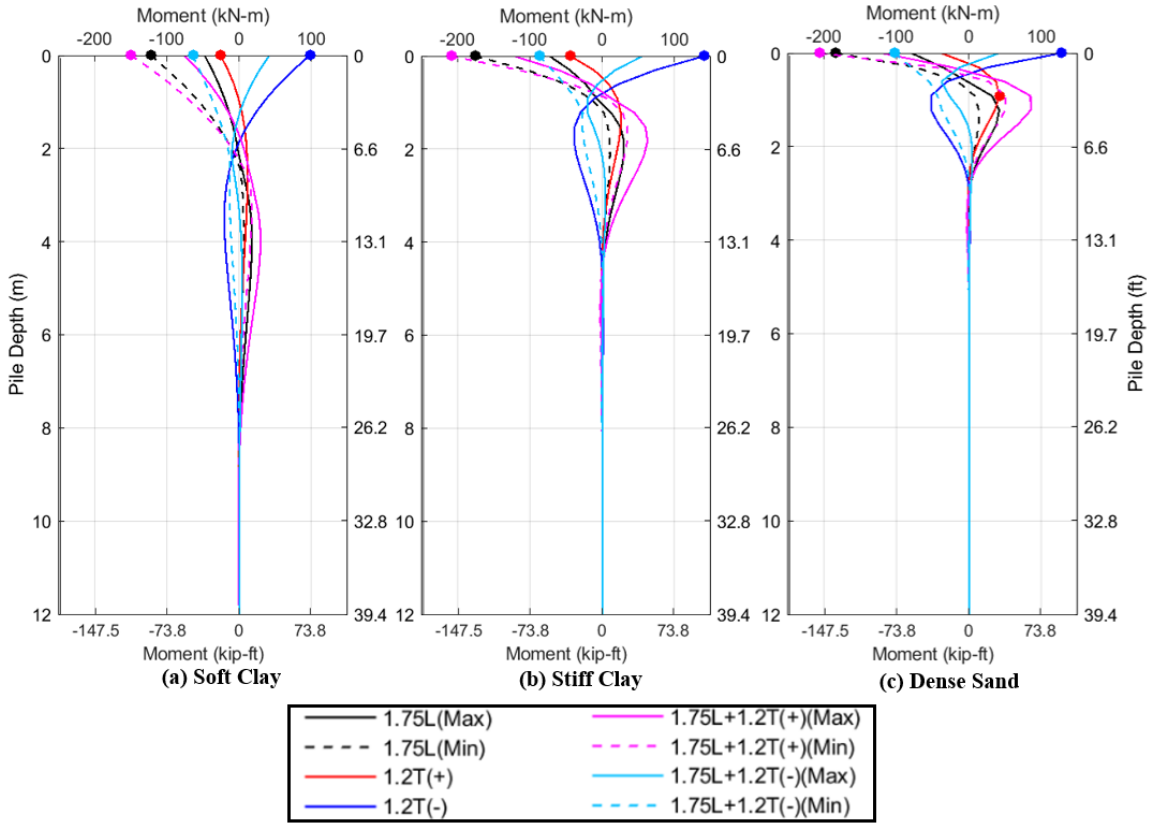

Figure 0.50: Pile Moment Diagram under Strength 1 Load Combinations for Uncracked 30m IABs with Medium Steel Girders on (a)Soft Clay, (b)Stiff Clay, and (c)Dense Sand
IAB parameters: Span Length = 30m, Girder = Medium Steel, and Pile = HP310x125 and Weak Axis Bending

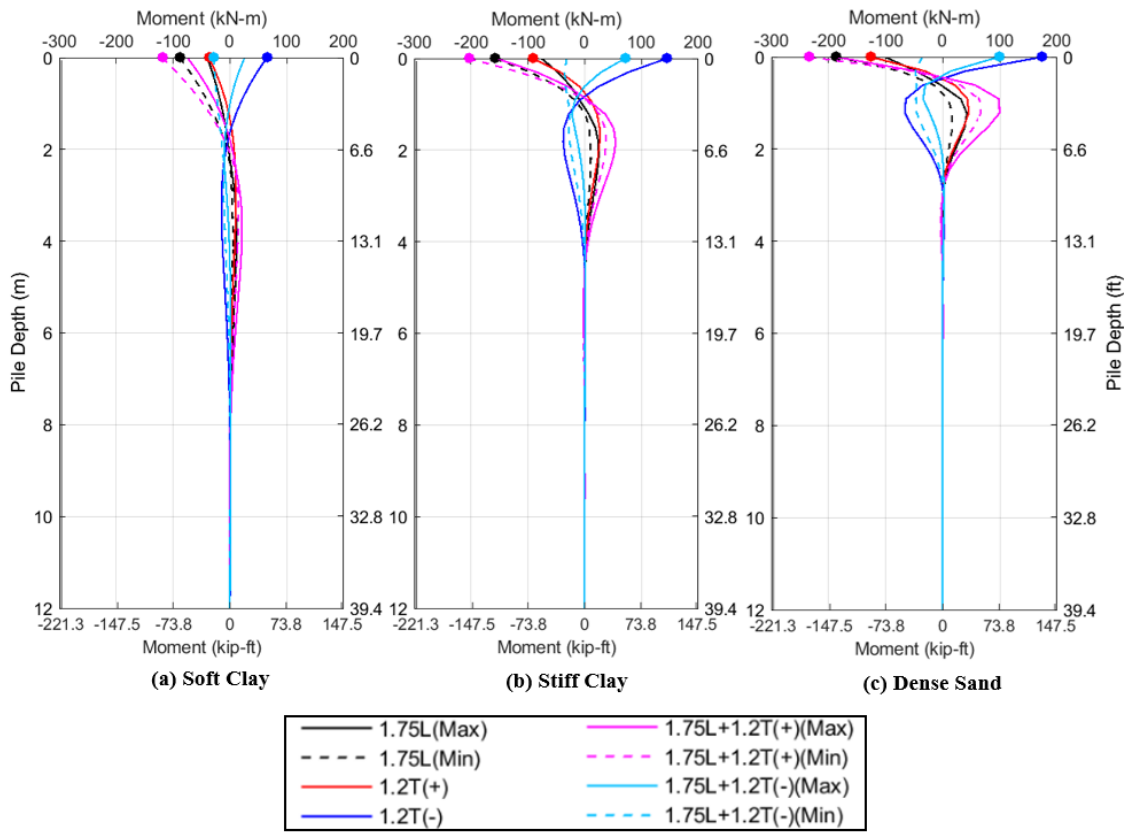

Figure 0.51: Pile Moment Diagram under Strength 1 Load Combinations for Uncracked 40m IABs with AASHTO Type VI on (a)Soft Clay, (b)Stiff Clay, and (c)Dense Sand

IAB parameters: Span Length = 40m, Girder = AASHTO Type VI, and Pile = HP310x125 and Weak Axis Bending

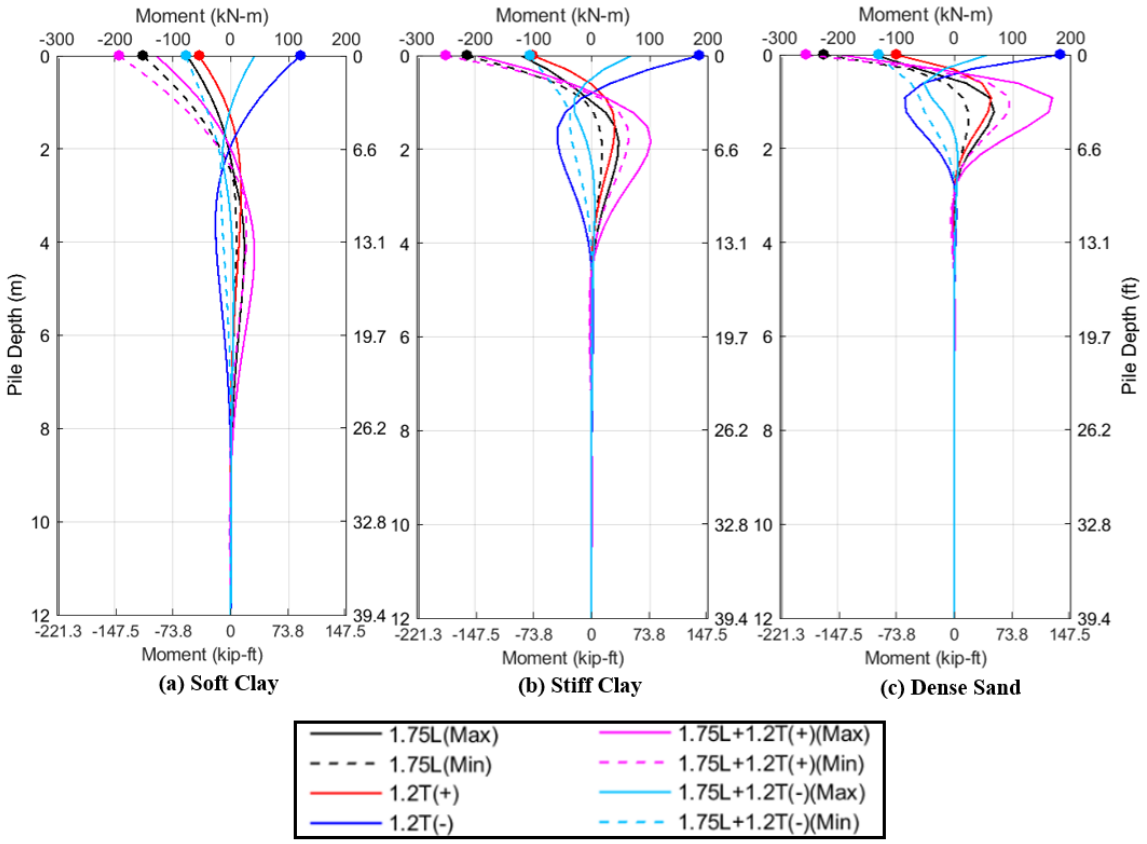

Figure 0.52: Pile Moment Diagram under Strength 1 Load Combinations for Uncracked 40m IABs with Large Steel Girders on (a)Soft Clay, (b)Stiff Clay, and (c)Dense Sand
IAB parameters: Span Length = 40m, Girder = Large Steel, and Pile = HP310x125 and Weak Axis Bending

5.3.1 Effect of Soil Stiffness

In this section, the effect of soil stiffness on the maximum pile moment was investigated. Figure 0.53 - Figure 0.55 show the comparison of the maximum absolute pile moment for all ideal IABs with HP310x125 oriented about the weak axis under 1.2T(+), 1.2T(-), and 1.75L+1.2T(+), respectively. The results of thermal loads in Figure 0.53 and Figure 0.54 present the comparison of absolute maximum pile moment along the pile, even though the depth of the maximum pile moment may be different for 20m

IABs, as previously shown. Thermal contraction (1.2T(-)) generally induced more absolute values of pile moment than thermal expansion (1.2T(+)). However, 1.75L+1.2T(+) controlled in most IABs because pile moment diagram of 1.2T(-) opposed to those of 1.75L and 1.2T(+), as presented in previously. The maximum pile moment under 1.75L+1.2T(+) load combination was always recorded at the top of pile.

The results showed that under thermal loads (1.2T(+) or 1.2T(-)), the uncracked sections induced more pile moment than the cracked sections in both 30m and 40m concrete and steel IABs. On the other hand, the cracked sections induced more pile moment under live load, and thus, the cracked sections induced more pile moment by up to 30% for concrete IABs under 1.75L+1.2T(+) load combination. For steel IABs, the effect of concrete cracking became negligible under 1.75L+1.2T(+) load combination. The results of 1.75L+1.2T(+) load combination also showed that maximum pile moment also increased as the foundation soil stiffened. This indicates that lower relative stiffness of superstructure to substructure (more flexible superstructure with concrete cracking or small girders or having stiffer substructure) increases the pile moment due to a larger influence of live load.

Under thermal expansion (1.2T(+)), the pile moment never reached yield moment capacity ($M_{y\_reduced}$) of HP section, however, the pile moment reached $M_{y\_reduced}$ in practically all 30m and 40m span IABs when combined with live load (1.75L+1.2T(+)). This was accommodated through the pile hinging included in the models. The results also showed that the pile moment did not reach plastic moment capacity ($M_{p\_reduced}$) defined in Table 0.7. For a reference, Figure 0.56 shows the maximum pile moment for the same

IABs under 1.0L+1.2T(+). Even under service load combinations, some longer IABs with stiffer foundation soil exceeded the yield moment capacity of the section.

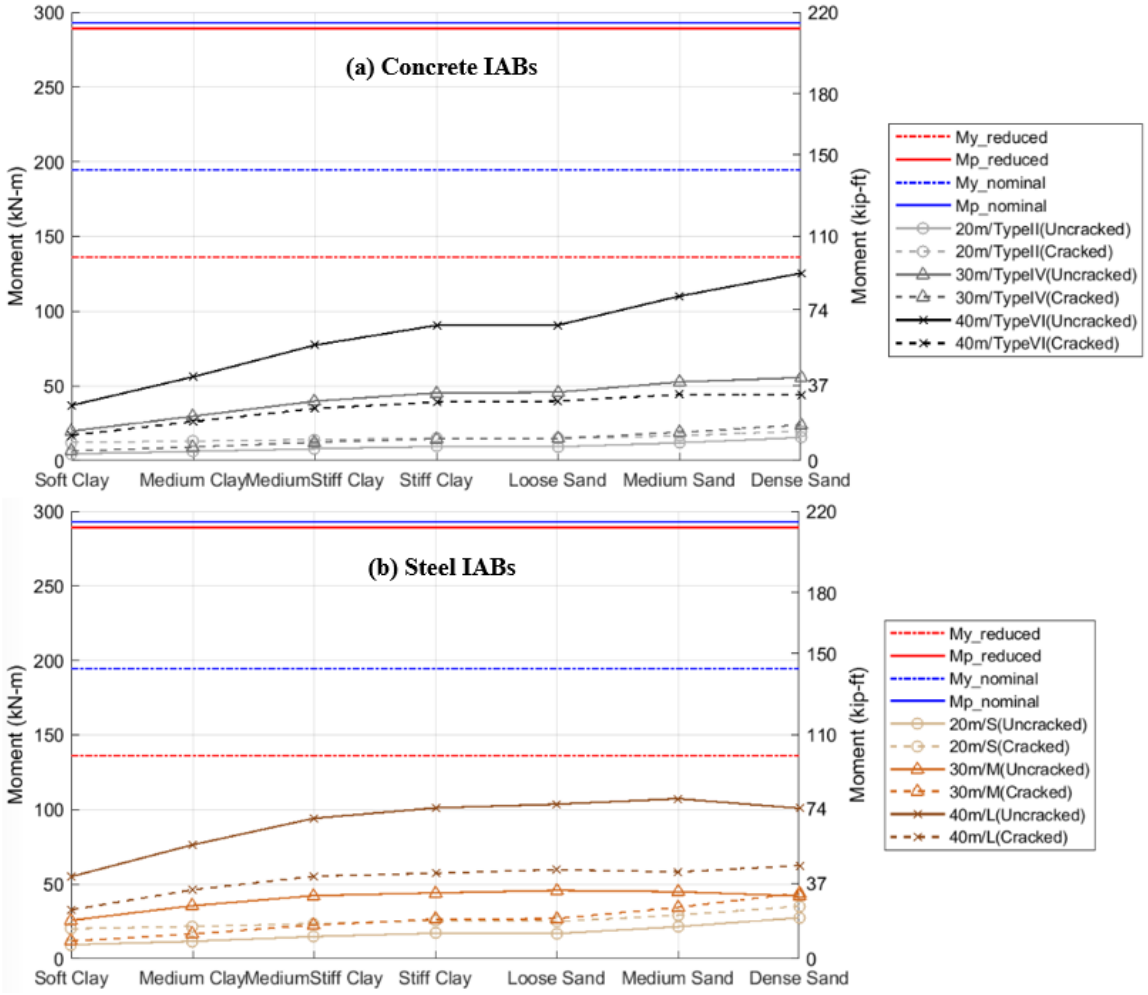

Figure 0.53: Maximum Absolute Pile Moment under 1.2T(+) for (a)Concrete and (b)Steel Ideal Girder IABs

Note: The yield and plastic moment capacities of HP310x125 are reduced from the nominal moment capacities due to axial load consideration.

IAB parameters: Pile = HP310x125 and Weak Axis Bending

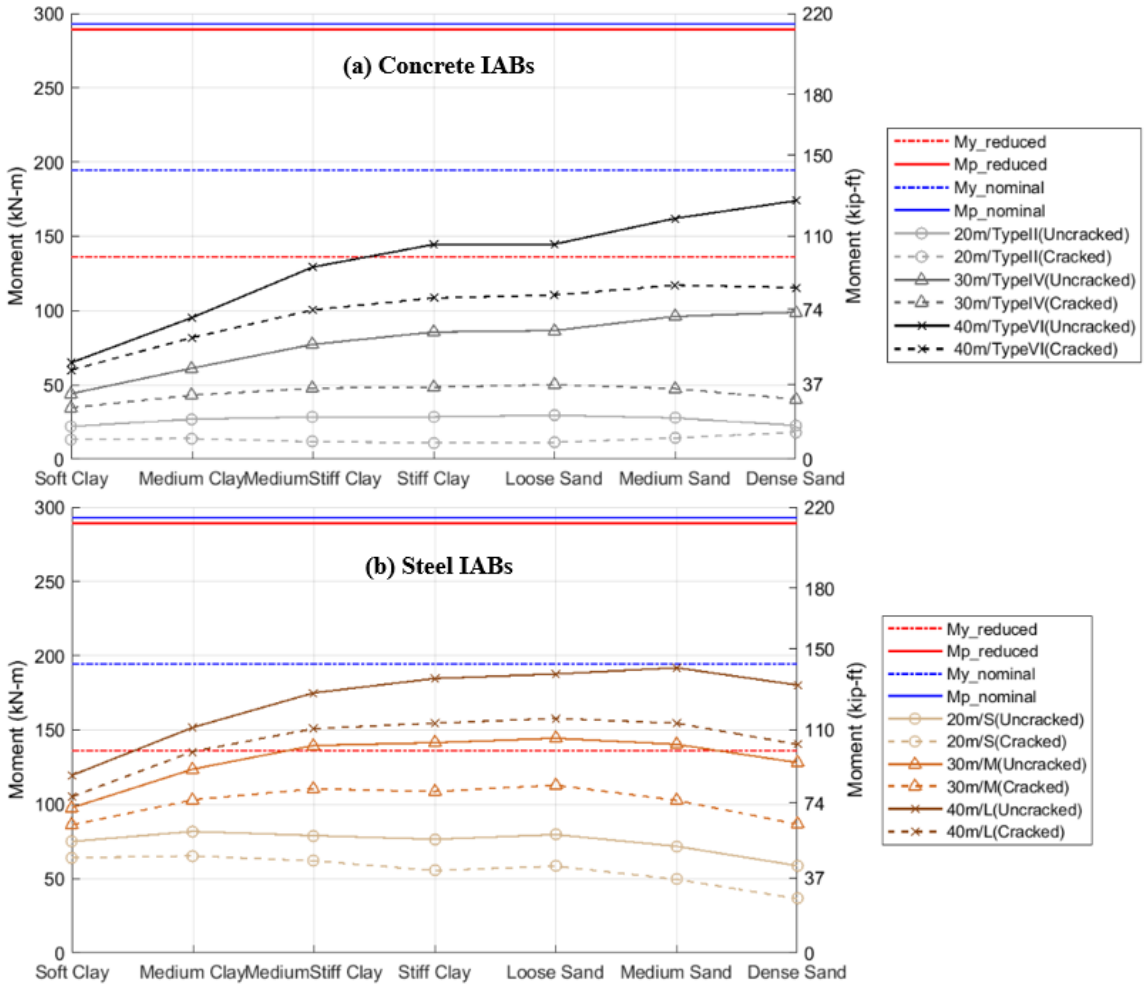

Figure 0.54: Maximum Absolute Pile Moment under 1.2T(-) for (a)Concrete and (b)Steel Ideal Girder IABs

Note: The yield and plastic moment capacities of HP310x125 are reduced from the nominal moment capacities due to axial load consideration.

IAB parameters: Pile = HP310x125 and Weak Axis Bending

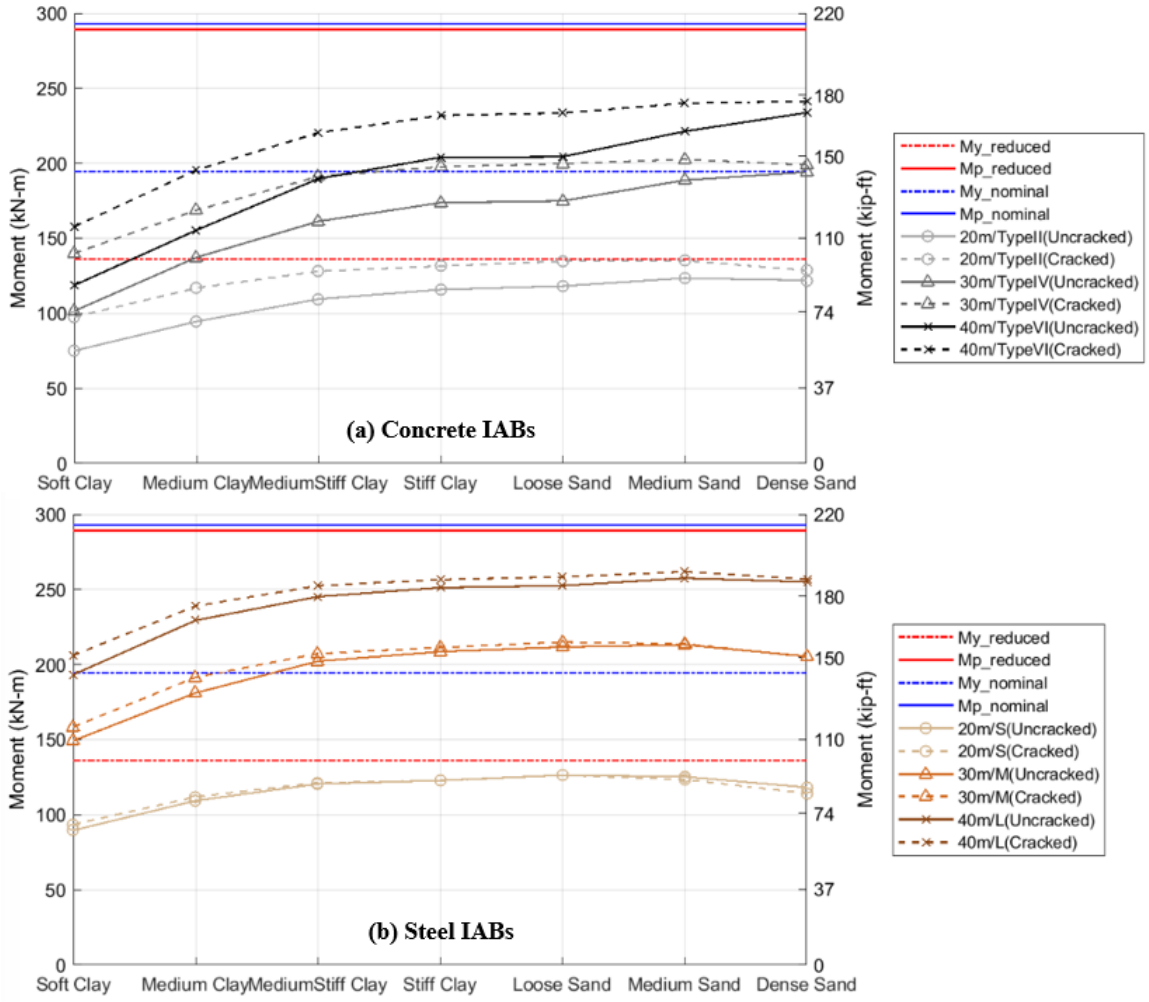

Figure 0.55: Maximum Absolute Pile Moment under 1.75L+1.2T(+) for (a)Concrete and (b)Steel Ideal Girder IABs

Note: The yield and plastic moment capacities of HP310x125 are reduced from the nominal moment capacities due to axial load consideration.

IAB parameters: Pile = HP310x125 and Weak Axis Bending

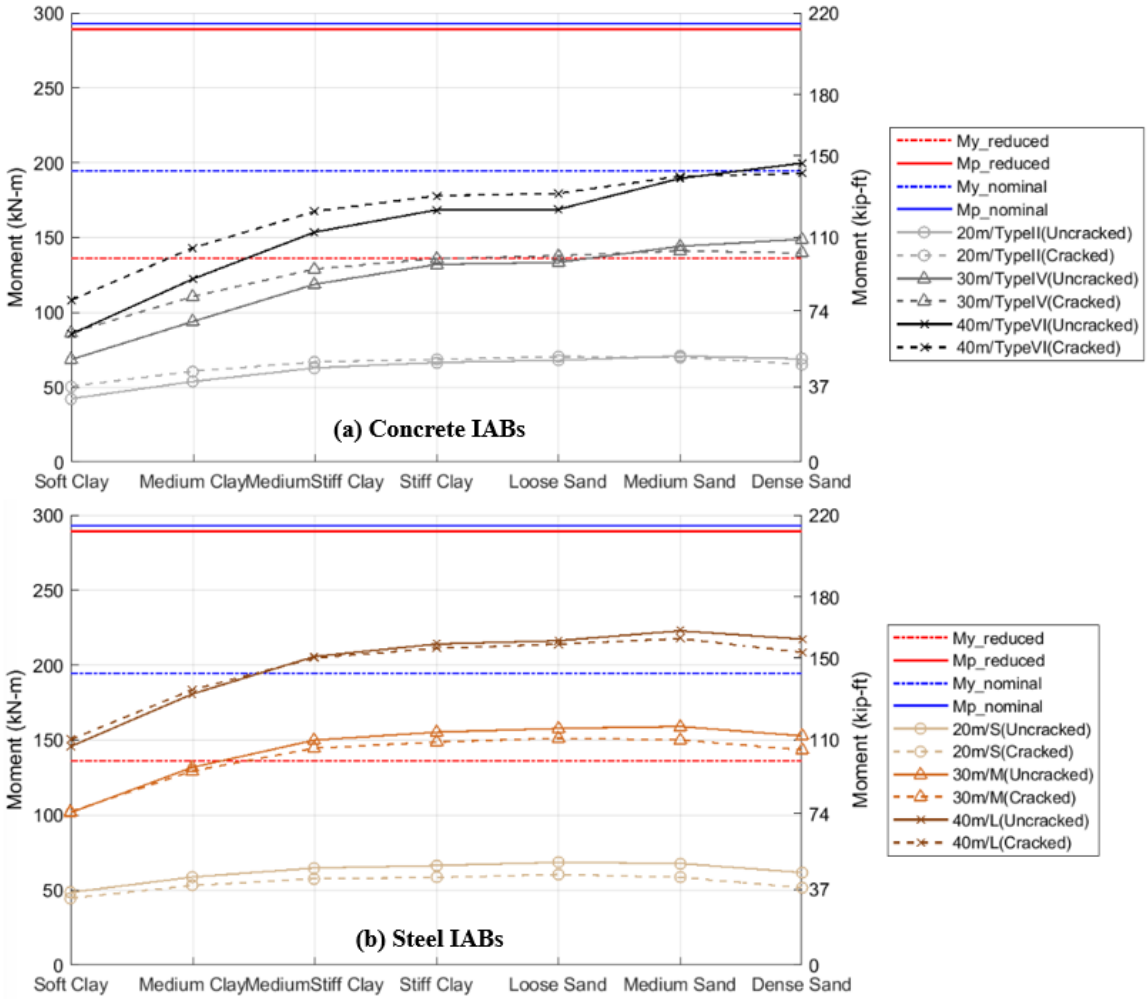

Figure 0.56: Maximum Pile Moment under 1.0L+1.2T(+) for (a)Concrete and (b)Steel Ideal Girder IABs

Note: The yield and plastic moment capacities of HP310x125 are reduced from the nominal moment capacities due to axial load consideration.

IAB parameters: Pile = HP310x125 and Weak Axis Bending

5.3.2 Effect of Span Length and Girder Size

The effects of span length and girder size on pile moments were also investigated. Figure 0.57 presents the maximum pile moment of IABs under 1.75L+1.2T(+) with varying girder sizes and HP310x125 oriented about the weak axis for each span length. IABs with unrealistic girder size were included in the figures to analyze the relative stiffness of superstructure to substructure on pile moment. The results are also limited to three soil types analyzed in this research.

The results showed that the pile moment increased as the span length increased for both concrete and steel IABs with the same girder sizes, as longer span IABs are influenced by larger loads. However, the effects of girder sizes were significantly varied between concrete and steel girder IABs due to stiffness of girders. With softer foundation soil, the results showed that the pile moment decreased as the superstructure stiffens with larger girders. In denser foundation soil, this trend became opposite in steel IABs and the effect of girder sizes became relatively negligible in concrete IABs. It also showed that the increasing rate from soft clay to dense sand became larger as the girder size became larger.

As observed in Figure 0.57 and substructure displacement results, when the effect of superstructure stiffness was analyzed under combined loads, the trend became unpredictable because the effects from live load and thermal load were opposite with the change of girder sizes. For a reference, the pile moment under live load (1.75L) and positive thermal load (1.2T(+)) at the top of pile are presented in Figure 0.58 and Figure 0.59, respectively. Under live load, the maximum pile moment increased with smaller girders, but the pile moment decreased with smaller girders under positive thermal load.

It is important to note that the maximum pile moment was not recorded at the top of pile under thermal load for some 20m IABs. However, for observing the effect from each load, Figure 0.59 shows the pile moment at the top of pile since it becomes critical under combined loads at the top of pile. The results are not included in this thesis, but the pile moment decreased with smaller girders under the negative thermal load (1.2T(-)) as well. However, as observed in the pile moment diagram, the pile moment under negative thermal load has an opposite sign in values, thus it reduces the moment and becomes not critical when combined with live load. The results also showed that the effect of thermal loads at the top of pile is overall negligible for 20m IABs.

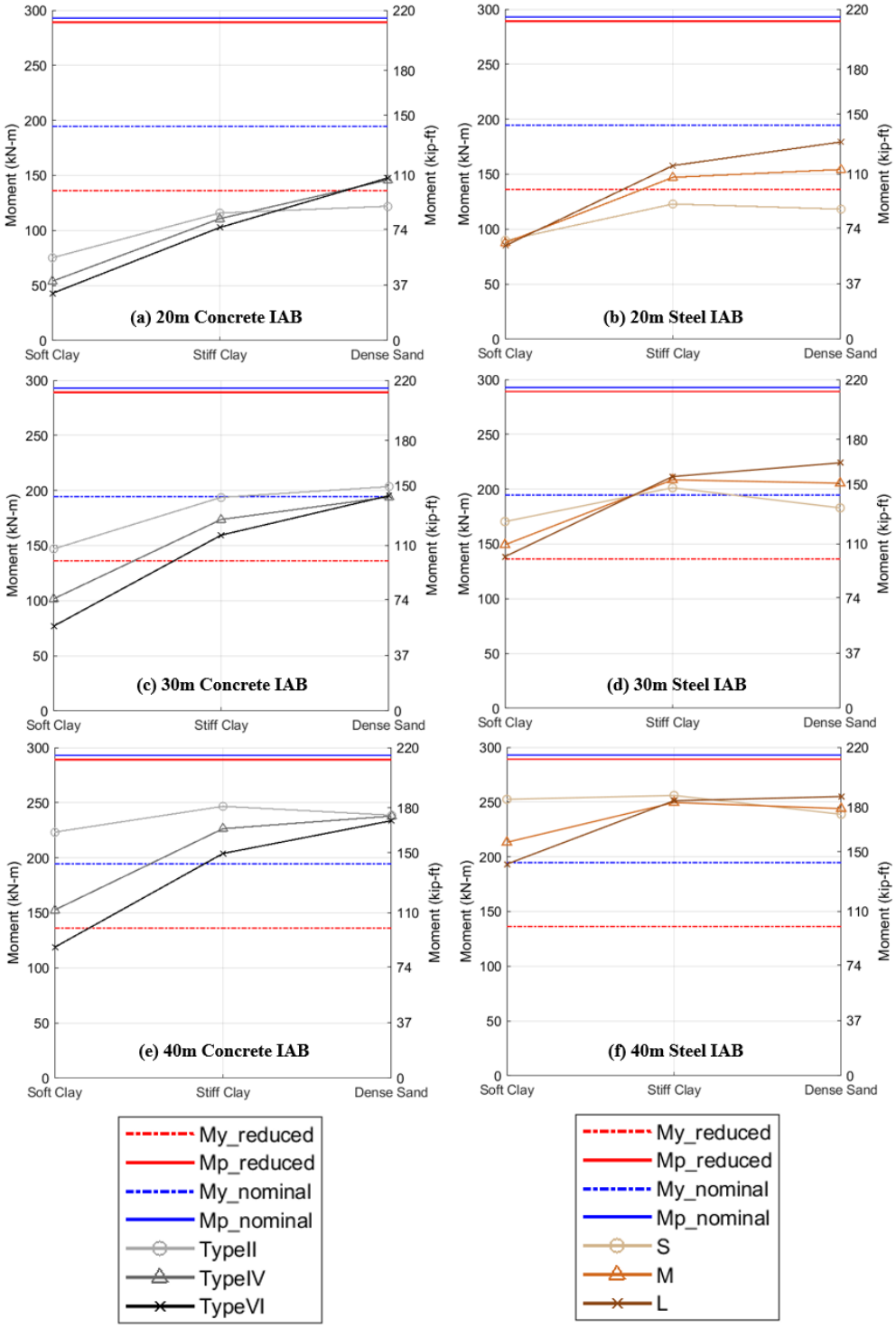

Figure 0.57: Maximum Pile Moment under 1.75L+1.2T(+) for (a)20m Concrete, (b)20m Steel, (c)30m Concrete, (d)30m Steel, (e)40m Concrete, and (f)40m Steel IABs with Varying Girder Size

Note: The yield and plastic moment capacities of HP310x125 are reduced from the nominal moment capacities due to axial load consideration.

IAB parameters: Pile = HP310x125 and Weak Axis Bending

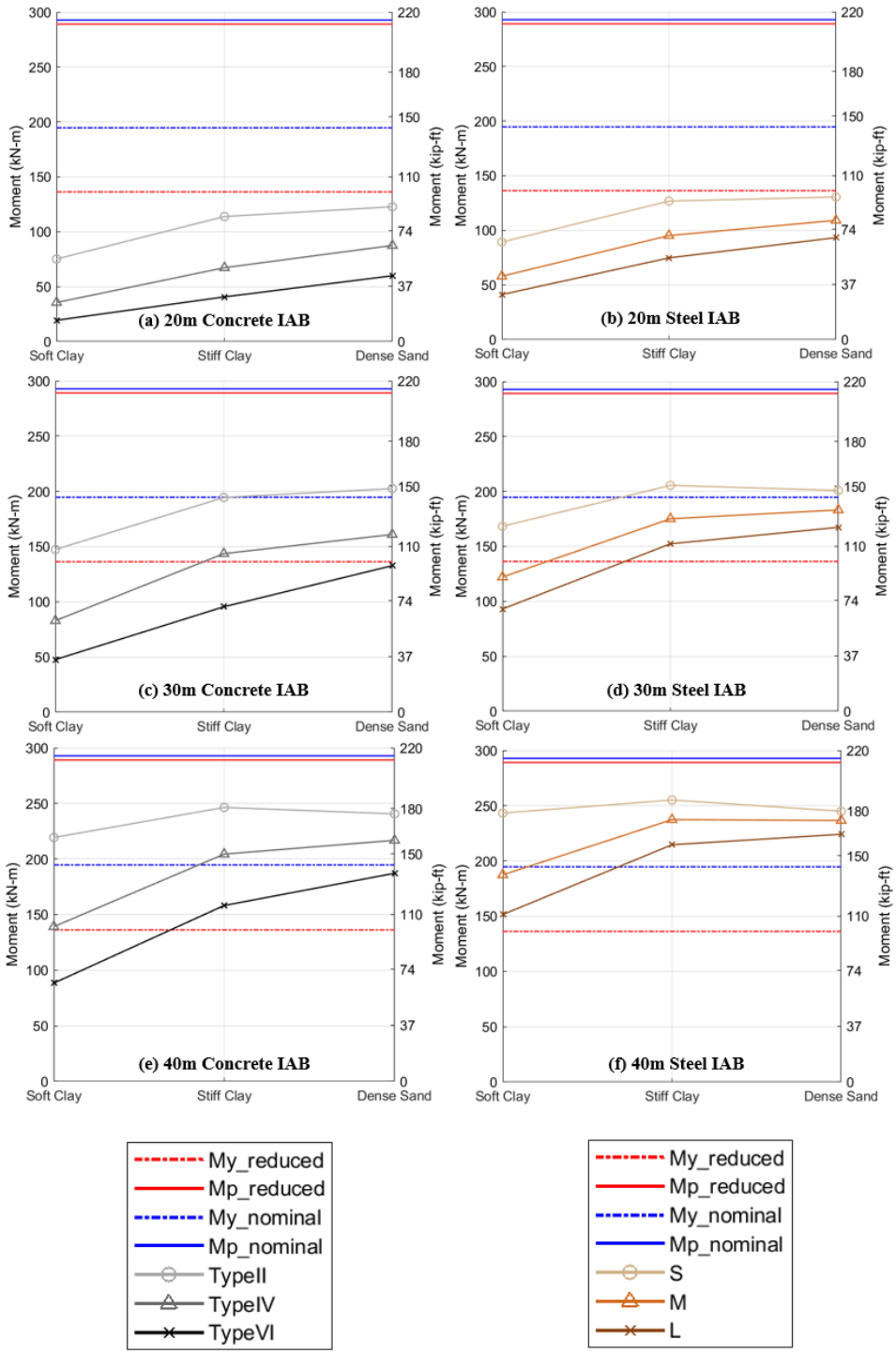

Figure 0.58: Maximum Pile Moment at under 1.75L for (a)20m Concrete, (b)20m Steel, (c)30m Concrete, (d)30m Steel, (e)40m Concrete, and (f)40m Steel IABs with Varying Girder Size

Note: The yield and plastic moment capacities of HP310x125 are reduced from the nominal moment capacities due to axial load consideration.

IAB parameters: Pile = HP310x125 and Weak Axis Bending

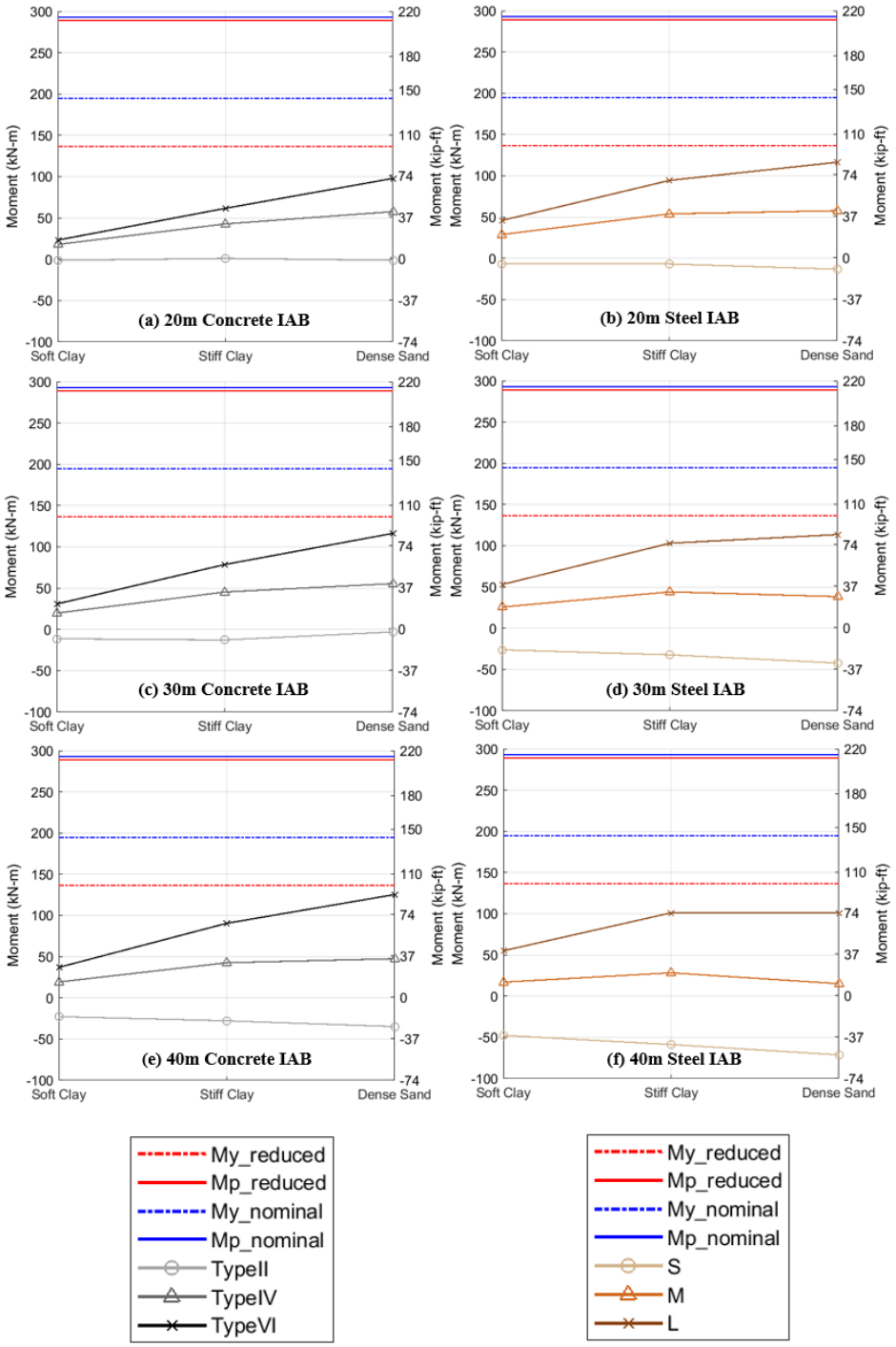

Figure 0.59: Maximum Pile Moment at under 1.2T(+) at Top of Piles for (a)20m Concrete, (b)20m Steel, (c)30m Concrete, (d)30m Steel, (e)40m Concrete, and (f)40m Steel IABs with Varying Girder Size

Note: The yield and plastic moment capacities of HP310x125 are reduced from the nominal moment capacities due to axial load consideration. Maximum pile moment under 1.2T(+) is not always at the top of pile.

IAB parameters: Pile = HP310x125 and Weak Axis Bending

5.3.3 Effect of Pile Size and Orientation

The effect of pile size and orientation on pile moment was investigated in this section. Figure 0.60 shows the maximum pile moment under 1.75L+1.2T(+) for IABs with varying pile size. Even though the pile size had minimal effects on the superstructure bending moment (as shown in Figure 0.17), the results showed that it has significant effects on maximum pile moment. As pile size increased from HP250x85 to HP310x125, the maximum pile moment increased, and the moment capacity of the section also increased. Essentially, as a stiffer pile is included, it requires a greater force to deform it. Even though the sharper transition from the abutment to pile was observed in the substructure of IABs with smaller piles (shown in Figure 0.43), the overall moment of inertia is smaller for HP250x85, thus it resulted in smaller pile moments despite the higher curvature. Since the moment capacity of the pile significantly increased, HP310x125 avoided the yielding of piles in all 20m IABs. However, piles in 30m and 40m IABs that yielded with HP250x85 still yielded with HP310x125. Implementing a larger pile size significantly increased the pile moment, and slightly reduced the chance of yielding the piles. The results shown in the figures are limited to three soil types, but the results of other soil types also follow the trend.

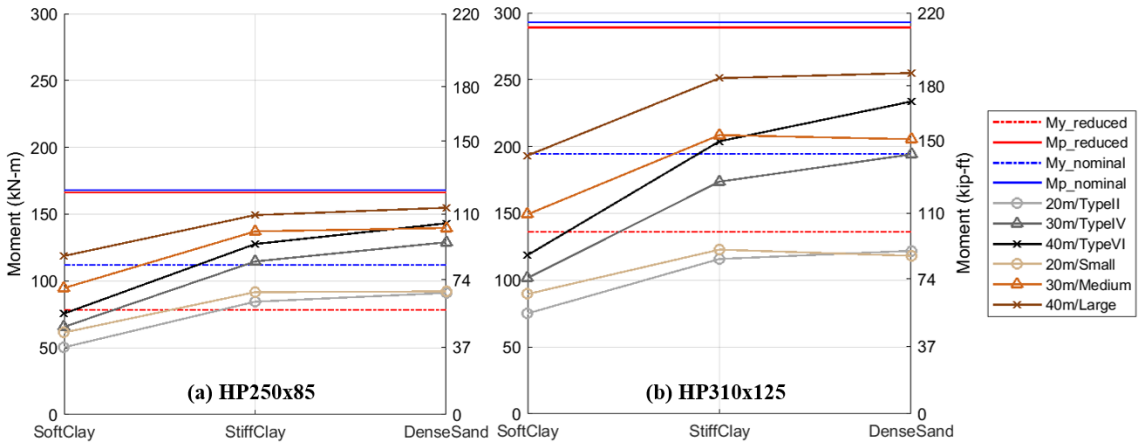

Figure 0.60: Maximum Pile Moment under 1.75L+1.2T(+) for IABs with Ideal Girders and (a)HP250x85 and (b)HP310x125 about Weak Axis Bending
Note: The yield and plastic moment capacities of piles are reduced from the nominal moment capacities due to axial load consideration in FEMs.
IAB parameters: Pile = Weak Axis Bending

Figure 0.61 and Figure 0.62 present the maximum pile moment for IABs with two pile sizes oriented about the weak and strong axes. The results showed that maximum pile moment overall increased when the pile was oriented about the strong axis. However, the moment capacity of the piles with strong-axis orientation also siginificnatly increased. When piles were oriented about the weak axis bending, most 30m and 40m IABs with stiffer foundation soil exceeded $M_{y\_reduced}$ (some 20m IABs also yielded for HP250x85). Even though the capacity increased for strong axis bending, 40m IABs with stiffer foundation soil still exceeded $M_{y\_reduced}$. This indicates that change in pile orientation does not always avoid the yielding of piles, but weak axis orientation is more likely to yield the piles due to its smaller flexural capacity. Even though it might yield the piles, weak axis orientation may still be prefereable to reduce the moment transferd from abutment to piles. All IABs were still below both the nominal and reduced yielding

capacity of the pile. The results shown in figures are limited to three soil types, but the results of other soil types also follow the trend.

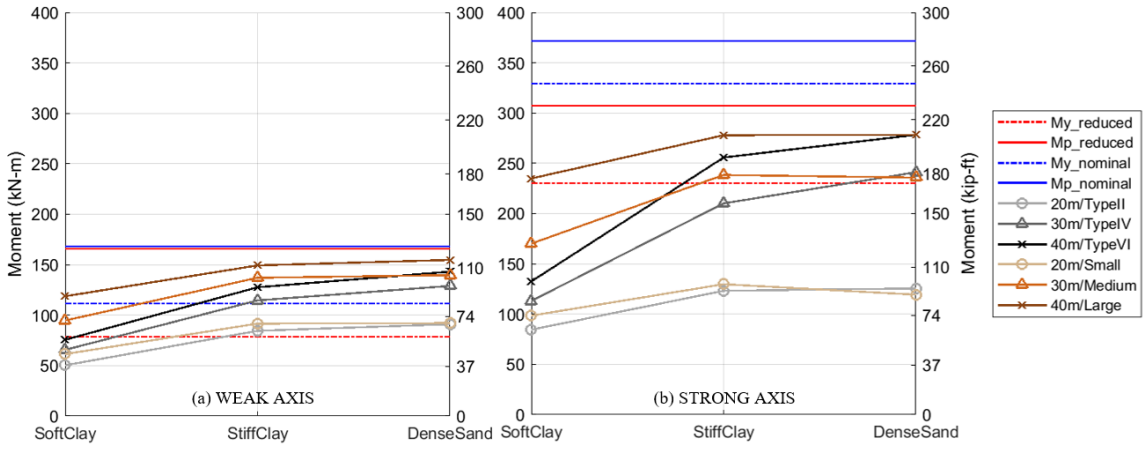

Figure 0.61: Maximum Pile Moment under 1.75L+1.2T(+) for IABs with Ideal Girders and HP250x85 Oriented about (a)Weak Axis and (b)Strong Axis Bending
Note: The yield and plastic moment capacities of HP250x85 are reduced from the nominal moment capacities due to axial load consideration in FEMs.
IAB parameters: Pile = HP250x85

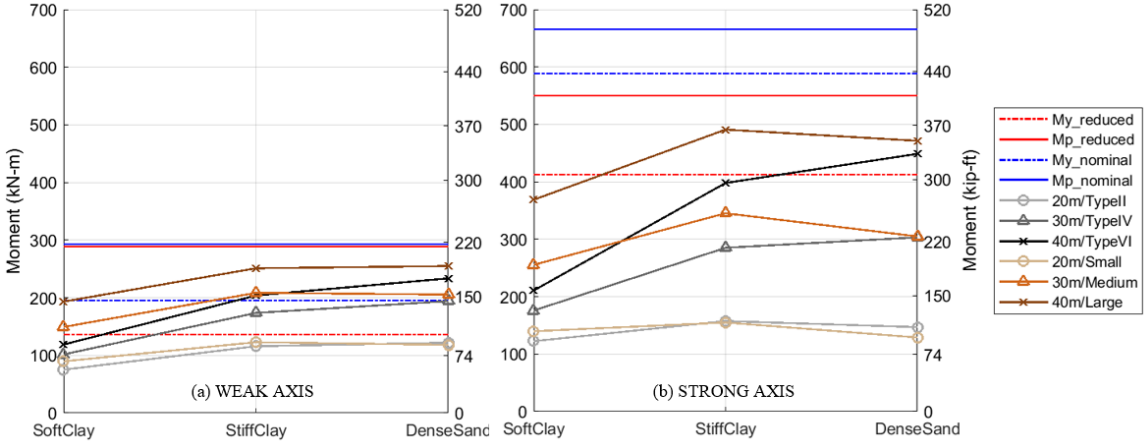

Figure 0.62: Maximum Pile Moment under 1.75L+1.2T(+) for IABs with Ideal Girders and HP310x125 Oriented about (a)Weak Axis and (b)Strong Axis Bending
Note: The yield and plastic moment capacities of HP310x125 are reduced from the nominal moment capacities due to axial load consideration in FEMs.
IAB parameters: Pile = HP310x125

5.4 Removal of Top 3m (10ft) Pile Springs

In the previous section, yielding of piles was observed in most IABs analyzed in this study under the critical strength and service load combinations. The yield criteria included the effects of axial load, so a reduction from the nominal yield moment capacity on the order of 30%. Several DOT's have used a construction method in which the dense soil is bored out for approximately 3m (10ft) at the top of piles and filled with softer materials to minimize the soil effects and minimize the potential for pile yielding. Several states have discontinued this practice due to not observing signs of pile yielding in practice where it was omitted. In this section, the effect of this method was investigated by removing the top 3m (10ft) of pile springs.

Table 0.9 shows the maximum mid-span full bridge cross section moment and pile moments recorded for some 30m and 40m concrete and steel IABs with sand foundation soil before and after the springs were removed. The results are limited to IABs with ideal girder sizes and HP310x125 oriented about the weak axis. The results showed that it maximum mid-span full bridge cross section moment was minimally affected, with the difference within 5%. On the other hand, it reduced the pile moment significantly. The pile moment in concrete IABs decreased by almost 50% and about 20 to 30% in steel IABs. This result indicates that replacing the soil around the top sections of piles is an effective way to reduce the pile moment, especially for concrete IABs.

The results also showed that the values of maximum pile moments for IABs with springs removed were almost identical to the results for the same IABs with soft clay or medium clay with springs fully attached. This is also observed from the substructure displacements, as presented in Figure 0.63 and Figure 0.64. When top 3m (10ft) of

springs were removed, no matter how stiff the rest of substructure is, the results became almost identical to the results of soft clay with springs fully attached. This indicates that the top 3m (10ft) of foundation soil plays an important role in the substructure stiffness.

Although the values of maximum pile moments were close to those for soft clay with springs fully attached, the moment diagram of the pile differed. Figure 0.65 and Figure 0.66 show the comparison of pile moment diagram of 40m concrete and steel ideal girder IABs between soft clay and dense sand with springs fully attached, and dense sand without the top 3m (10ft) of springs removed. At the top of pile, the moment in dense sand without top springs removed ((c) of figures) was almost identical to the moment for soft clay with springs fully attached ((a) of figures). A sharper kink was observed in (c) of each figure at the depth of 3m (10ft) due to stiff soil present from this depth, causing more moment than the moment for soft clay ((a) of figures) at the 3m (10ft); however, it was not as critical as the moment at the top of pile.

Table 0.9: Maximum Superstructure and Pile Moments Before and After the Soil Springs Removal under the Critical Strength 1 Load Combination

Bridge Dimension				**Maximum Mid-span Full Bridge Cross Section Moment (kN-m)**			**Maximum Pile Moment (kN-m)**		
Span Length (m)	Girder Size	Pile Size	Foundation Soil	Before Removal	After Removal	% Difference	Before Removal	After Removal	% Reduction
30	Type IV	HP310x125	Medium Sand	9834	10290	4.5	189	97	48.7
30	Type IV	HP310x125	Dense Sand	9768	10270	5.0	194	103	47.1
30	M	HP310x125	Loose Sand	9543	9813	2.8	212	149	29.4
30	M	HP310x125	Medium Sand	9502	9786	2.9	213	159	25.5
30	M	HP310x125	Dense Sand	9529	9765	2.4	205	164	20.4
40	Type VI	HP310x125	Medium Sand	16296	15758	-3.4	221	115	48.2
40	Type VI	HP310x125	Dense Sand	16598	15754	-5.2	234	122	47.8
40	L	HP310x125	Loose Sand	15086	15322	1.6	252	201	20.3
40	L	HP310x125	Medium Sand	15104	15292	1.2	257	209	18.8
40	L	HP310x125	Dense Sand	15157	15268	0.7	255	214	16.2

Note: HP310x125(Weak Axis): $M_{y\_reduced}$ = 136.3kN-m and $M_{p\_reduced}$ = 289.1kN-m

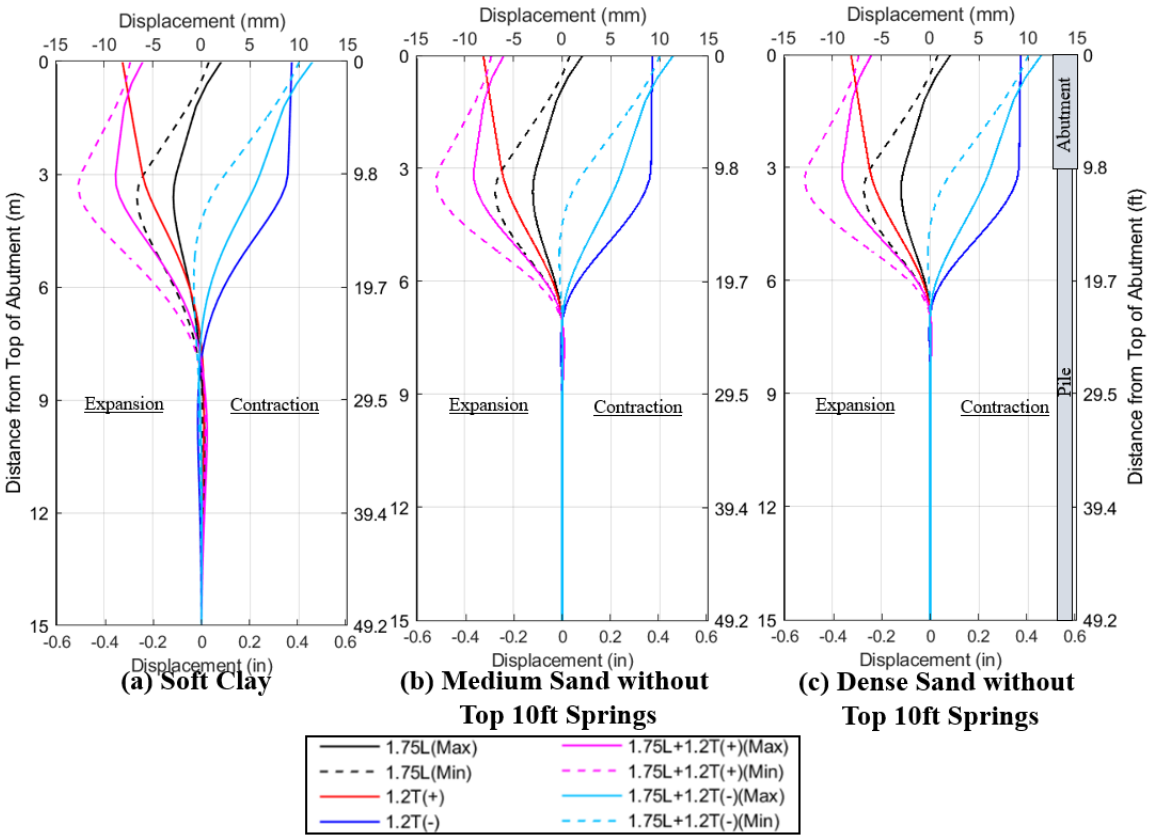

Figure 0.63: Substructure Displacement under Strength 1 Load Combination for 40m IABs with AASHTO Type VI on (a)Soft Clay with Springs Fully Attached, (b)Medium Sand, and (c) Dense Sand without Top 3m (10ft) Springs

IAB parameters: Pile = HP310x125 and Weak Axis Bending

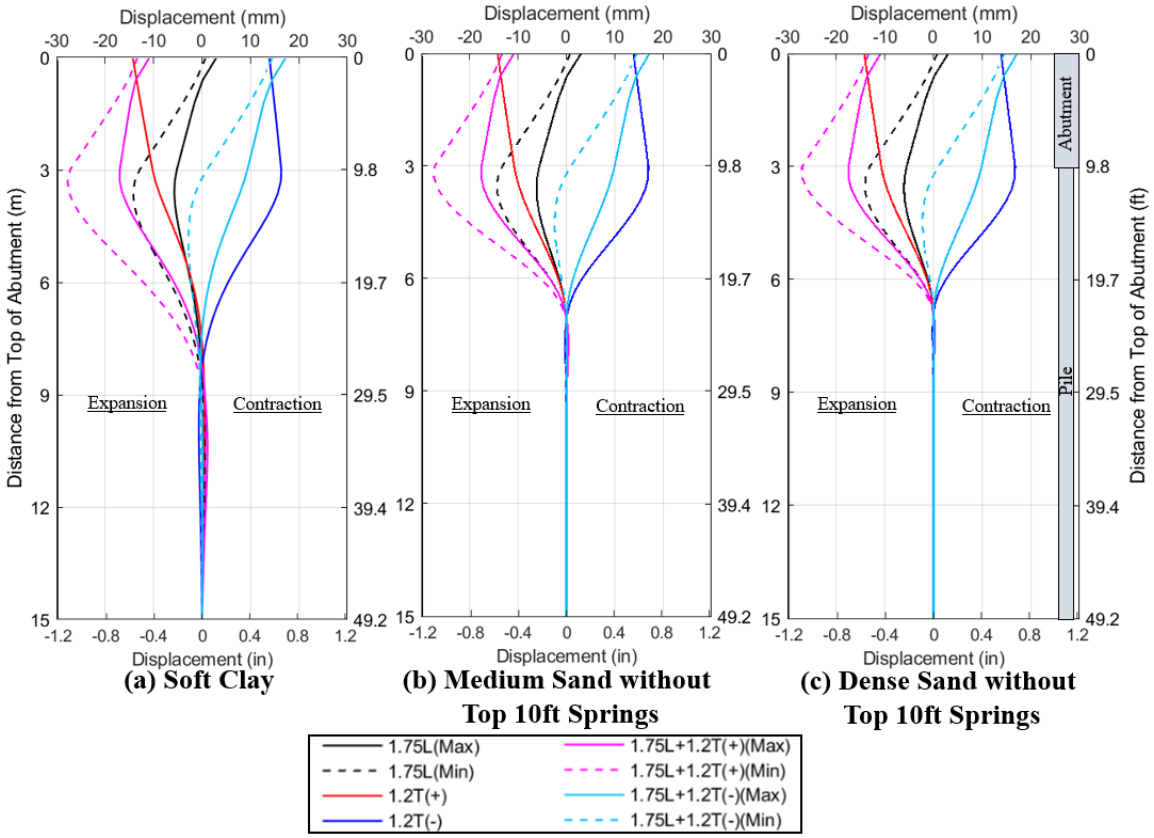

Figure 0.64: Substructure Displacement under Strength 1 Load Combination for 40m IABs with Large Steel Girders on (a)Soft Clay with Springs Fully Attached, (b)Medium Sand, and (c) Dense Sand without Top 3m (10ft) Springs

IAB parameters: Pile = HP310x125 and Weak Axis Bending

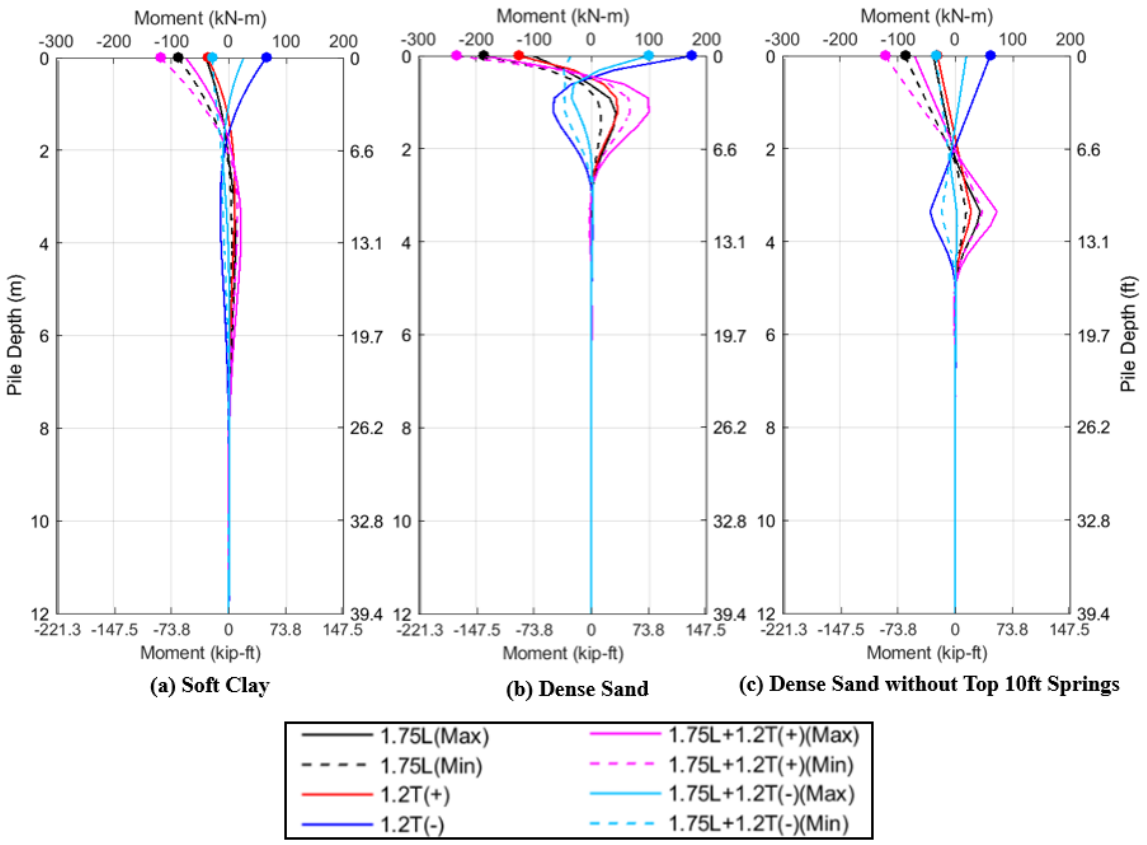

Figure 0.65: Pile Moment Diagrams under Strength 1 Load Combinations for 40m IABs with AASHTO Type VI on (a)Soft Clay and (b) Dense Sand with Springs Fully Attached, and (c) Dense Sand without Top 3m (10ft) Springs

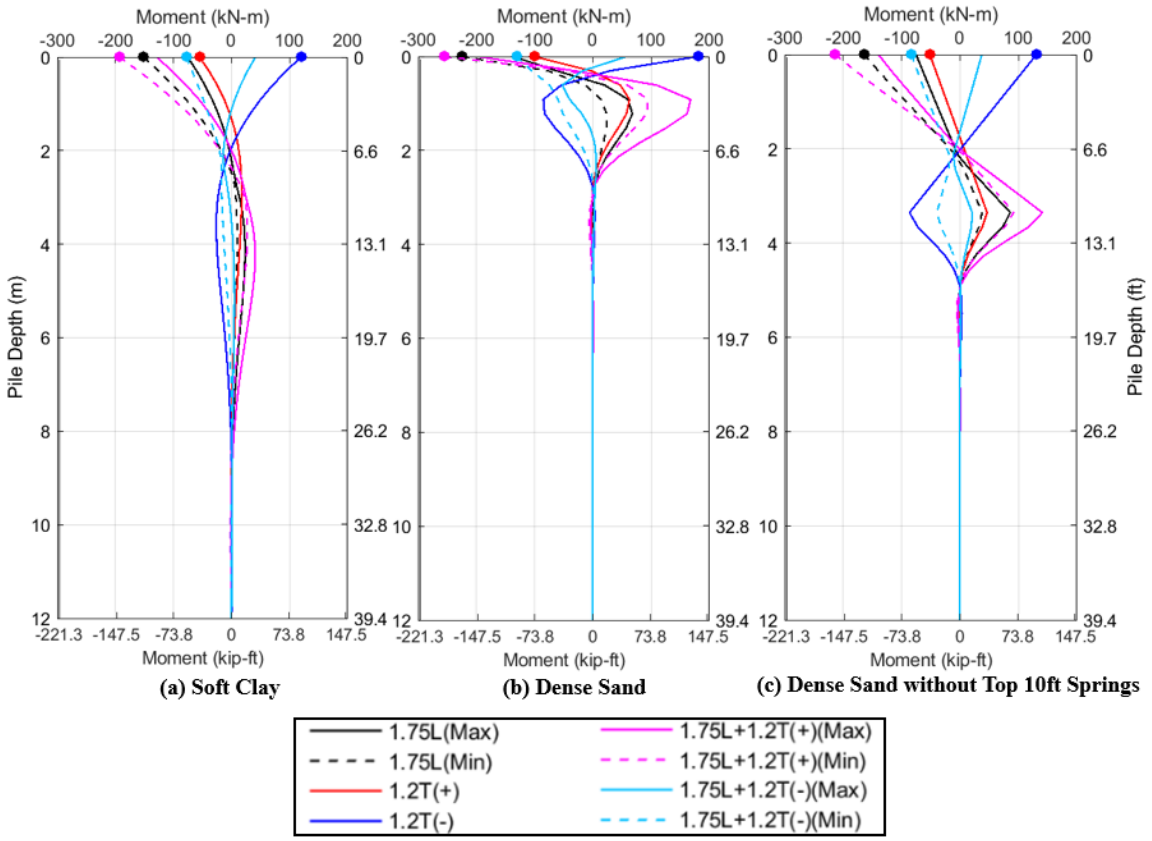

Figure 0.66: Pile Moment Diagrams under Strength 1 Load Combinations for 40m IABs with Large Steel Girders on (a)Soft Clay and (b) Dense Sand with Springs Fully Attached, and (c) Dense Sand without Top 3m (10ft) Springs

5.5 Discussion of Results

In this chapter, the effects of various structural and geotechnical parameters on the performance of single-span IABs under combined loads were analyzed, using the inelastic finite element analysis (FEA). There were several assumptions made in this analysis. Results presented in this chapter did not include the dead load since dead load was analyzed separately on simply supported beams in Chapter 3. The results of dead load must be superimposed when AASHTO LRFD load combinations were considered, but it only influences superstructure mid-span moment. Another assumption was made in

the moment-curvature relationships in defining plastic hinges of piles. The piles are subjected to axial dead and live loads; thus, the moment capacities of HP sections are expected to be smaller than the nominal moment capacities. The axial load was found to be 10 to 30% of the capacity of typical piles, and so 30% of axial pile capacity was included for a consistency regardless of the overall bridge size, even though the axial load could be smaller depending on the bridge dimensions; therefore, the yield capacity of piles was reduced by 30% from the nominal yield capacity of piles without axial load. The effect of axial load result in earlier yielding of piles in some of the models, however other moment curvature relationships can be compared to results presented per Figure 0.5.

The results of this chapter showed that individual load cases affected each type of bridge response differently. As the stiffness of foundation soil increased, the moment diagram of superstructure (full bridge cross section and girder moments) shifts downwards under live and positive thermal loads and shifts upwards under negative thermal load. The positive and negative thermal loads generate constant negative and positive superstructure moments, respectively throughout the span. The superstructure moments at end-span under live and positive thermal loads are negative values, thus, the increase in soil stiffness results in a larger negative value of superstructure moments at end-span. This increase in superstructure moments at end-span generally causes higher pile moments, as more moment is transferred to the substructure.

Since individual load cases impact the results differently, the trends in the results vary under the combined load cases, and the critical load combination also differs in each type of bridge responses. The combination of live and negative thermal loads controls the

superstructure mid-span moments, and the combination of live and positive thermal loads controls the superstructure end-span moments and pile moment. The effects of thermal loads on substructure results are significantly smaller for short span IABs, so the effect of live load becomes more significant for those IABs. Overall, in the design of IABs, the analysis under the load combination of live and thermal loads (both positive and negative thermal loads) is important to capture the effects from each individual load case on the bridge response.

Due to the fixity of superstructure and substructure in IABs, the relative stiffness of superstructure to substructure has significant effects on each type of bridge response: superstructure and pile bending moments and substructure displacement and rotation. Increasing the substructure stiffness with the change of foundation soil has minimal impacts on the superstructure bending moment at mid-span under the critical Strength 1 load combination (1.75L+1.2T(-)); live load decreases, but negative thermal load increases as the substructure stiffens, counteracting the effect from each load. Increasing the substructure stiffness with stiffer pile size or orientation also has minimal effects for the same reason. Therefore, the substructure stiffness has minimal effects on maximum superstructure mid-span moments under its critical load combination (1.75L+1.2T(-)). On the other hand, the substructure stiffness is significant in the superstructure moment at the end-span and substructure results. The increase of the substructure stiffness with stiffer foundation soil results in a more negative superstructure moment at the end, transferring more moments to substructure, thus, a larger pile moment is also observed for IABs with stiffer foundation soil. Additionally, when stiffer foundation soil is present around the piles, it limits the displacement of the overall substructure, creating a sharp transition

from the abutment to pile; this also increases the pile moment due to a higher curvature at that location.

The change of pile geometries also contributes to the change in substructure stiffness. The substructure stiffness increases with larger piles or piles oriented about the strong axis bending. IABs respond similarly to when the substructure is stiffened by foundation soil; the change of substructure stiffness by changing the substructure geometries has no effects on superstructure mid-span moments, however, it has significant effects on the end-span superstructure moments and substructure results. The increase of the substructure stiffness with larger piles or pile oriented about the strong axis limits the overall movement of the substructure, thus a smaller displacement is observed. When a larger pile size or strong-axis orientation are used, the capacities of piles increase significantly. However, the pile moment also increases significantly, and thus, the piles may still yield; most IABs that exceeded the reduced yield capacity of piles with the weak-axis orientation still exceeded the reduced yield capacity of piles with strong-axis orientation in this study. Therefore, replacing with larger piles or strong-axis orientation was not significantly effective for avoiding the yielding of the pile for the IABs of this study under the assumption made for the yield capacity of piles. Although most IABs exceeded the yield capacity of piles, the results also showed that replacing piles with larger piles or the strong-axis orientation never reached nominal or reduced plastic capacities of piles for all IABs. The weak-axis orientation may still be preferable in the design of IABs to reduce the force transferred from the abutment to the pile.

Even though the piles never reached the plastic moment capacity of the piles in this study, designers may still be concerned about yielding of the piles, especially in

dense soil. One of the methods designers sometimes use in dense soils is to bore out the soil around the top section of piles and fill with softer materials. This is beneficial in order to reduce the pile moment significantly, since pile moment is most critical around the top of piles. Reducing the stiffness around the top of the pile allows the piles to be more flexible and decreases the pile moment significantly. Overall, it reduced the maximum pile moment by 20 to 50%, and the reduction was much larger for concrete IABs. Thus, this method seems especially beneficial for avoiding yielding of the piles for concrete IABs.

The effects of changing the superstructure stiffness were also analyzed in this study. To analyze this effect, this study investigated IABs parametrically, including girder sizes that may be unrealistic for the span length. Longer span IABs generally have larger values in all types of results regardless of girder sizes, since longer span bridges are subjected to larger load effects: higher superstructure and pile moments, and larger displacement and rotation. The superstructure stiffness also changes by the change of girder sizes. Having larger girders always increases the mid-span superstructure moments under its critical load combination (1.75L+1.2T(-)). On the other hand, the change of the girder size had minimal effects on the end-span superstructure moments under its critical load combination (1.75L+1.2T(+)). As the girder size increases for the given span length, the change of values in end-span moment from soft clay to dense sand is an increasing value of end-span superstructure moments induced by positive thermal load (T(+)), but a decreasing value of end-span superstructure moments by live load (L). The positive thermal load influences the results almost equally as the live load. Therefore, the opposite

effect from each load counteracts under the combination of these loads, and end-span superstructure moments remain relatively consistent regardless of the girder size.

Although the effects of the change in superstructure stiffness on superstructure response was relatively apparent, this effect was difficult to predict on the substructure response. The opposite trend from live and thermal loads were also observed in substructure displacements and pile moment. Increasing girder size results in a larger substructure displacement and pile moment under the thermal loads (T(+) and T(-)) but a smaller substructure displacement and pile moment under the live load (L). The effects from each load case depend on the relative stiffness of superstructure to substructure, and thus, it is difficult to predict the clear trend when these loads were combined.

The effect of concrete cracking was also considered in this study. Overall, it has minimal effects on the results of steel IABs since steel girders are not subjected to the cracking. Concrete cracking reduces the superstructure stiffness; thus, it decreases the mid-span superstructure moments under thermal loads but increases the end-span negative superstructure moments and pile moment under the thermal loads. On the other hand, under the live load, it increases the mid-span superstructure moments but decreases end-span negative superstructure moments and pile moment. Generally, under the critical load combination of live and thermal loads, it follows the trend of the results for live load; the concrete cracking reduces the superstructure moments at mid-span but increases the end-span negative superstructure moment and pile moment. Overall, the concrete cracking had almost negligible effects on the pile moment and end-span superstructure moments for steel IABs as cracking did not reduce the superstructure stiffness as much as concrete IABs. The cracking increased the pile moment under the load combination of

1.75L+1.2T(+) in concrete IABs built on softer foundation soil by about 30%, but the effect also became less significant with stiffer foundation soil.

CHAPTER 6

CONCLUSION AND DESIGN RECOMMENDATION

This study investigated the difference between the performance of traditional jointed bridges and IABs, using FEA. The effects of various parameters (bridge geometries and soil stiffnesses) on the IAB responses were analyzed under load combinations. The results of this study are limited to short to moderate single-span straight bridges under dead, live, and thermal loads. The major findings from this study are following:

- The fixity of superstructure and substructure in IABs shifts the overall superstructure moment diagram downwards, resulting in negative end-span superstructure moments and lower mid-span superstructure moments compared to the moment diagram of SSBs.
- Substructure stiffness is contributed by both foundation soil stiffness and pile geometries, and superstructure stiffness is contributed by the stiffness of girders and concrete cracking.
- The effects of the increase in substructure stiffness and superstructure stiffness under individual load cases are summarized in Table 0.1 and Table 0.2, respectively.
- Under individual unfactored load cases considered, the results remained in the linear range of soil and pile properties (no yielding of piles). However, under factored and combined loads, yielding of the piles was observed in most 30m and 40m span IABs.

- The effect of substructure stiffness became minimal on mid-span superstructure moments under critical Strength 1 load combination of live and negative thermal loads (1.75L+1.2T(-)), as effects from each load counteracted. However, they were significant on the end-span superstructure moment under its critical Strength 1 load combination (1.75L+1.2T(+)), as the negative moment at end-span increased significantly with stiffer substructure.
- For 20m IABs, the thermal effects on pile moment were negligible.
- The pile moments were significantly lower than the end-span superstructure moments even after the end-span superstructure moments were divided by four piles.
- AASHTO LLDFs developed for SSBs were generally 20 to 50% higher than the LLDFs resulted for IABs in this study. They may be overly conservative for IABs when bridges were analyzed as SSBs. When IABs were analyzed as a 2-D rigid frame, the difference from AASHTO LLDFs was about ±10% for interior girder moment and up to 25% smaller for exterior girder moment.
- The LLDFs computed using the proposed equations for concrete IABs by Dicleli and Erhan (2009) agreed well with the LLDFs resulted from 2-D rigid frame analysis of this study for interior girder moments of both concrete and steel IABs. However, the resulting LLDFs for exterior girder moments of IABs were 10 to 20% larger. For IABs with ideal girders, increasing the LLDFs calculated using the proposed equation by about 10% may produce better estimates for the bridges studied.

- The change in pile size and pile orientation does not influence superstructure bending moments, but it has significant effects on the results of substructure; stiffer piles by having larger sizes or orienting piles about the strong axis bending increase the pile moment and decrease the substructure displacements. Even though increasing the stiffness of piles increases the capacities of piles and reduces the change of yielding slightly, the weak-axis orientation may still be preferable to reduce the force transferred between piles and abutment.
- Piles are subjected to axial load induced by dead and live loads. Axial load on piles reduces the yield and plastic capacity of piles. However, the reduction in the yield and plastic capacity of piles would not be proportional due to the redistribution of stress and strain hardening. Including these effects on moment-curvature relationship of piles may result in more realistic behavior of piles under combined axial and flexural loads.
- Boring out the soil around the top section of the pile and filling with softer materials may be beneficial for avoiding the yielding of the piles for bridges built on dense soil. The results showed that when top 3m (10ft) of soil was removed (replaced), the bridge responses became almost identical to IABs built on soft clay. This reduces the maximum pile moment about 50% in concrete IABs and 20 to 30% in steel IABs.
- The effects of concrete cracking are smaller on substructure response of the steel IABs, but concrete cracking is important to consider in the design of all IABs, as it significantly increases the pile moment by up to about 25% and reduces the mid-span moment by about 20%. Concrete cracking reduces the superstructure

stiffness; thus, it shifts the superstructure moment diagram down, and increases the substructure deformation and pile moment.

Table 0.1: Trend in Bridge Response with Increase in Substructure Stiffness

	Mid-Span Positive Superstructure Moment	**End-Span Negative Superstructure Moment**	**Absolute Substructure Displacement**	**Absolute Maximum Pile Moment**
L	Decrease	Increase	Decrease (Away)	Increase
T(+)	Decrease (Negative)	Increase	Decrease (Away)	Increase
T(-)	Increase	Decrease (Positive)	Decrease (Towards)	Decrease

Note: Positive = Positive value of moment. Negative = Negative value of moment.
Away = Substructure moves away from the center of bridge. Towards = Substructure moves towards to center of bridge.

Table 0.2: Trend in Bridge Response with Increase in Superstructure Stiffness

	Mid-Span Positive Superstructure Moment	**End-Span Negative Superstructure Moment**	**Absolute Substructure Displacement**	**Absolute Maximum Pile Moment**
L	Increase	Decrease	Decrease (Away)	Decrease
T(+)	Decrease (Negative)	Increase	Increase (Away)	Increase
T(-)	Increase	Decrease (Positive)	Increase (Towards)	Increase

Note: Positive = Positive value of moment. Negative = Negative value of moment.
Away = Substructure moves away from the center of bridge. Towards = Substructure moves towards to center of bridge.

Based on the findings from this research, some design recommendations for IABs are made below:

- Superstructure of IABs results in a large negative moment at end-span. The amount of negative moment increases significantly with stiffer foundation soil, especially for longer span IABs. In design of concrete girder IABs, it is important to account for the negative moment and reinforce the top of girders or in the slab for composite at end-span appropriately. It is also important to account for in the design of steel girder IABs to size the bottom flange of steel girders at end-span accordingly.
- AASHTO LLDFs may be conservative to use in IABs. If 2-D simply supported beam analysis is performed for IABs, AASHTO LLDFs may be used for IABs with an assumption of up to 50% reduction. However, the possible reduction highly depends on superstructure and substructure stiffnesses.
- The proposed LLDF equations for IABs by Dicleli and Erhan (2009) may be used to estimate the LLDFs of IABs. The proposed equation for interior girder moment estimates the LLDFs of IABs well, but the LLDFs for exterior girder moment estimated using the proposed equation need to be increased by about 10% to 20%.
- Yielding of piles is unavoidable for the bridges studied under the consideration of AASHTO Strength 1 load combinations for longer span IABs. If yielding of piles is concerned for IABs built in dense foundation soil (sand), boring out and replacing the soil 1.8m (6ft) from top of the piles with softer material is an effective way to reduce the maximum pile moment significantly.
- Effect of concrete cracking is especially important to consider for longer span concrete IABs and concrete IABs built on softer foundation soil, as it results in a larger pile moment.

Future study may include the following:

- For each individual load case, formulating the relationship between relative stiffness of superstructure to substructure and the response of IABs may be useful in design.
- The reasons for the pile moment being significantly lower than the superstructure end-span moments should be investigated further. The force couple between the axial load built up in superstructure and soil forces are a likely cause, but there was not a clear relationship due to nonlinearity of models and varying depth of significant soil spring forces.
- The methods for redistribution of negative moments used in multi-span or continuous beam bridges may be applicable in designing IABs to assume some reduction in the negative moment at end-span. However, further study is required to verify.
- The LLDF equation for exterior girder moment of IABs proposed by Dicleli and Erhan (2009) were unconservative by up to 20% for the bridges and parameters considered in this study. Improvements on this equation may be beneficial.
- The effects of curvature, skew, and multiple spans were not considered in this study, and they may affect the bridge behavior. Including these parameters in the future parametric analysis may be beneficial.

BIBLIOGRAPHY

American Association of State and Highway Transportation Officials (AASHTO). (2003). *Guide specifications for horizontally curved highway bridges*. AASHTO. Washington (DC).

American Association of State and Highway Transportation Officials (AASHTO). (2017). *AASHTO LRFD Bridge Design Specifications*. Washington (DC).

American Petroleum Institute. (2014). "Recommended practice for planning, designing and constructing fixed offshore platforms – working stress design, Washington (DC)."

Albhaisi, S. (2012). "Effect of substructure stiffness on the performance of integral abutment bridges under thermal loads." dissertation.

Breña, S., Civjan, S., Bonczar, C., DeJong, J., and Crovo, D. (2007). "Integral Abutment Bridge Behavior: Parametric Analysis of a Massachusetts Bridge." *Journal of Bridge Engineering*, 12(1), 64-71.

Bonczar, C. (2005). "Behavior of Integral Abutment Bridges: Finite Element Analysis and Field Performance of the Orange-Wendell Bridge." Unpublished thesis, University of Massachusetts Amherst.

Burke, M. P. (2009). Integral and semi-integral bridges. Wiley-Blackwell, Chichester, U.K.

Civjan, S. A., Kalayci, E., Quinn, B. H., Breña, S. F., and Allen, C. A. (2013). "Observed integral abutment bridge substructure response." Engineering Structures, 56, 1177–1191.

Civjan, S., Kalayci, E., Breña, S., Quinn, B., Allen, C. (2014a). "Performance Monitoring of Jointless Bridges- Phase III- Final Report Part I." Rep. no. 2014-07. Vermont Agency of Transportation and Federal Highway Administration.

Civjan, S., Quinn, B., Breña S., Kalayci, E., Allen, C. (2014b). "Performance Monitoring of Jointless Bridges- Phase III- Final Report Part II." Rep. no. 2014-07. Vermont Agency of Transportation and Federal Highway Administration.

Clough, G. M., and Duncan, J. M. (1991). Foundation engineering handbook, 2nd Ed., H. Y. Fang, ed., Van Nostrand Reinhold, New York.

Cooperative Highway Research Program. (2006). "Development of LRFD specifications for horizontally curved steel girder bridges." Report 563. Transportation Research Board, Washington (DC).

Deng, Y., Phares, B. M., Greimann, L., Shryack, G. L., and Hoffman, J. J. (2015). "Behavior of curved and skewed bridges with integral abutments." Journal of Constructional Steel Research, 109, 115–136.

Dicleli, M., and Albhaisi, S. M. (2004). "Effect of cyclic thermal loading on the performance of steel H-piles in integral bridges with stub-abutments." Journal of Constructional Steel Research, 60(2), 161–182.

Dicleli, M., and Erhan, S. (2008). "Effect of Soil and Substructure Properties on Live-Load Distribution in Integral Abutment Bridges." Journal of Bridge Engineering, 13(5), 527–539.

Dicleli, M., and Erhan, S. (2009). "Live Load Distribution Formulas for Single-Span Prestressed Concrete Integral Abutment Bridge Girders." Journal of Bridge Engineering, 14(6), 472–486.

Dicleli, M., and Erhan, S. (2010). "Effect of soil–bridge interaction on the magnitude of internal forces in integral abutment bridge components due to live load effects." Engineering Structures, 32(1), 129–145.

Dicleli, M., and Erhan, S. (2010). "Effect of superstructure-abutment continuity on live load distribution in integral abutment bridge girders." Structural Engineering and Mechanics, 34(5), 635–662.

Erhan, S., and Dicleli, M. (2009). "Live load distribution equations for integral bridge substructures." Engineering Structures, 31(5), 1250–1264.

Kalaycı, E., Civjan, S. A., Breña, S. F., and Allen, C. A. (2011). "Load Testing and Modeling of Two Integral Abutment Bridges in Vermont, US." Structural Engineering International, 21(2), 181–188.

Kalayci, E., Civjan, S., and Breña, S. (2012). "Parametric study on the thermal response of curved integral abutment bridges." *Engineering Structures*, 43, 129-138.

Kalayci, E. (2012). "Performance monitoring and analysis of integral abutment bridges." Doctoral Dissertations 1896 – February 2014. 387. University of Massachusetts Amherst.

Kozak, D., Lafave, J., and Fahnestock, L. (2018). "Seismic modeling of integral abutment bridges in Illinois." *Engineering Structures*, 165, 170–183.

Kunin, J., and Alampalli, S. (2000). "Integral Abutment Bridges: Current Practice in United States and Canada." *Journal of Performance of Constructed Facilities*, 14(3), 104-111.

Lybas, J. M. (1970) "Strength of wide-flange sections under combined axial force and weak-axis bending, October 1970." Fritz Laboratory Reports. 361.1.

Maruri, R., Petro, S. (2005). “Integral abutments and jointless bridges (IAJB) 2004 survey summary.” Proceedings of the 2005 FHWA conference: integral abutments and jointless bridges, Baltimore, MD.

Matlock, H. (1970). “Correlation for Design of Laterally Loaded Piles in Soft Clay.” *Proceeding Offshore Technology Conference*. Houston, TX.

National Steel Bridge Alliance (NSBA). (2013). “Short Span Steel Bridge Standard Designs” NSBA.

Peck, R. B., Hanson, W. E., & Thornburn, T. H. (1974). *Foundation engineering*. New York: Wiley.

Precast/Prestressed Concrete Institute (PCI) (2011). *Bridge Design Manual 3rd Edition*. Chicago, IL.

Quinn, B., and Civjan, S. (2017). "Parametric Study on Effects of Pile Orientation in Integral Abutment Bridges.” *Journal of Bridge Engineering*, 22(4), 04016132.

Salman, N. N., and Issa, M. A. (2021). “Calibration and parametric investigation of integral abutment bridges.” *Engineering Structures*, 227, 111381.

Wood, J. H. (2015). “Earthquake Design of Bridges With Integral Abutments.” *6th International Conference on Earthquake Geotechnical Engineering 1-4 November 2015 Christchurch, New Zealand*.

Vermont Agency of Transportation (VTran). (2008). *Integral abutment bridge design guidelines*. Montpelier (VT).